Transient Stability Improvement in a Transmission Line Using Neuro-Fuzzy Based Unified Power Flow Controller [Case Study of Adama II, Koka to Kality Substation]

Menberu Gebre Mengistu

A Thesis Submitted to the Department of Electrical Power and Control Engineering

College of Electrical Engineering and Computing

Presented in Partial Fulfilment of the Requirement for the Degree of Master's in Electrical Power and Control Engineering (Power System Engineering)

Office of Graduate Studies

Adama Science and Technology University

June, 2025

Adama, Ethiopia

Transient Stability Improvement in a Transmission Line Using Neuro-Fuzzy Based Unified Power Flow Controller [Case Study of Adama II, Koka to Kality Substation]

Menberu Gebre Mengistu

Advisor: Dr. Kena Likassa

A Thesis Submitted to the Department of Electrical Power and Control Engineering

College of Electrical Engineering and Computing

Presented in Partial Fulfilment of the Requirement for the Degree of Master’s in Electrical Power and Control Engineering (Power System Engineering)

Office of Graduate Studies

Adama Science and Technology University

June, 2025

Adama, Ethiopia

DECLARATION

I hereby declare that this Master's thesis, titled “Transient Stability Improvement in a Transmission Line Using Neuro-Fuzzy-Based Unified Power Flow Controller,” is my work. It has not been submitted for the award of any degree, diploma, or certificate at any other institution. All sources and references used in the preparation of this thesis have been properly cited and acknowledged.

Menberu Gebre	______________	________________
Name of the Student	Signature	Date

RECOMMENDATION

As the advisor of this thesis, I hereby confirm that I have reviewed the revised version of the thesis titled "Transient Stability Improvement in a Transmission Line Using Neuro-Fuzzy-Based Unified Power Flow Controller," prepared under my supervision by Menberu Gebre. This thesis has been submitted in partial fulfilment of the requirements for the degree of Master of Science in Electrical Power and Control Engineering (Power System Engineering).

Accordingly, I recommend that the revised version of the thesis be submitted to the department in accordance with the relevant procedures.

Dr. Kena Likassa	____________________	11/06/2025
Advisor	Signature	Date

APPROVAL PAGE

I, the advisor of the thesis titled "Transient Stability Improvement in a Transmission Line Using Neuro-Fuzzy-Based Unified Power Flow Controller," prepared by Menberu Gebre, hereby confirm that the recommendations and suggestions provided by the board of examiners have been properly addressed and incorporated into the final version of the thesis.

Dr.Kena Likassa		11/06/2025
Advisor	Signature	Date

We, the undersigned members of the Board of Examiners, have reviewed and evaluated the thesis submitted by Menberu Gebre, titled "Transient Stability Improvement in a Transmission Line Using Neuro-Fuzzy-Based Unified Power Flow Controller," and have assessed the candidate during the open defence. We hereby certify that the thesis is approved as part of the requirements for the degree of Master of Science in Electrical Power and Control Engineering (Power System Engineering).

Chairperson	Signature	Date
Dr.Negasa Muleta		11/06/2025
Internal Examiner	Signature	Date
Dr.Yeshitla Shiferaw		12/06/2025
External Examiner	Signature	Date

Final approval and acceptance of the thesis depend on submitting the final version to the Office of Postgraduate Studies (OPGS) via the Department Graduate Council (DGC) and the College Graduate Committee (CGC).

Department Head	Signature	Date
College Dean	Signature	Date
Office of Postgraduate Studies, Dean	Signature	Date

ACKNOWLEDGEMENT

First and foremost, I am profoundly thankful to the Almighty God for His constant blessings throughout my research journey. His strength and guidance have sustained me and enabled me to complete this thesis.

I sincerely thank my advisor, Dr. Kena Likassa, for allowing me to pursue this research and for his constant guidance throughout the journey. His vision, integrity, enthusiasm, and encouragement have been a great source of inspiration. Through his mentorship, I have gained valuable skills in conducting thorough research and communicating results clearly and effectively. It has been a true honour and privilege to learn and work under his supervision, and I am deeply grateful for the support and knowledge he has generously provided.

I am truly grateful to the staff of the Melka Wakena, Koka, Kality, and Adama Wind Farm substations and generation units at EEP for their generous support and cooperation. Their readiness to share important data and technical information was essential to the successful completion of this research. The results presented in this thesis would not have been achievable without their help.

Finally, I extend my gratitude to everyone who supported me in completing this thesis, whether directly or indirectly.

Menberu Gebre

TABLE OF CONTENTS

LIST OF FIGURES

LIST OF TABLES

LIST OF ABBREVIATIONS

ANFIS	Adaptive Neuro-Fuzzy Interferance System
EEP	Ethiopian Electric Power
FACTs	Flexible AC Transmission System
FIS	Fuzzy Inference System
FPSS	Fuzzy Power System Stabilizer
GD	Gradient Descent
GTO	Gate Turn-off Thyristor
GUI	Graphical User Interface
IEEE	Institute of Electrical and Electronics Engineers
IGBT	Insulated Gate Bipolar Transistor
IPFC	Interline Power Flow Controller
KCL	Kirchhoff's Current law
KVAR	kilovolt Amps Reactive
KVL	Kirchhoff's voltage law
LFO	Load Frequency Control
LSE	Least Square Estimation
MF	Membership Function
NR	Newton Raphson
PI	Proportional Integral

PID	Proportional Integral Derivative
PLL	Phase Lock Loop
PSO	Particle Swarm Optimization
PWM	Pulse Width Modulation
SMIB	Single machine infinite bus
SSSC	Static Synchronous Series Compensator
STATCOM	Static Synchronous Compensator
STATCON	Static Synchronous Condenser
SVC	Static Var Compensator
TCR	Thyristor Controlled Reactor
TCSC	Thyristor Controlled Series Capacitor
THD	Total harmonic distortion
UPFC	Unified Power Flow Controller
VSC	Voltage Source Converter

ABSTRACT

High-voltage transmission networks in Ethiopia are vulnerable to transient instability due to long lines and faults, causing power losses and voltage deviations. To meet increasing demand and ensure a secure power supply, the Ethiopian Electric Power office suggests enhancing transmission line capacity with the integration of Flexible AC Transmission System (FACTS) devices. This research proposes a Unified Power Flow Controller (UPFC) based on a Neuro-Fuzzy Inference System (NFIS) for high-voltage transmission networks. The UPFC will provide reactive power compensation quickly, and the optimal placement will be determined using Particle Swarm Optimization. The controller will be tested under fault scenarios and active power analysis across different transmission lines. When a three-phase ground fault occurs at the midpoint of the Koka to Kality East Industry transmission line, for example, the use of an ANFIS-based UPFC reduces the settling time of rotor angle deviation, rotor speed, rotor speed deviation, and output active power by 70.48%, 38%, 38%, and 44%, respectively, in comparison to a system without a UPFC. A PI-based UPFC reduces active power loss on the Koka to Kality East Industry transmission line by 54.54% at peak load, while an ANFIS-based UPFC reduces it by 72.72%. Similarly, at peak load, active power loss is decreased by 70% with an ANFIS-based UPFC and by 50% with a PI-based UPFC for the Adama II, Koka, and Melka Wakena to Kality transmission line. In general, the UPFC based on ANFIS.

Keywords: *Wind Power, Transmission line, ANFIS, UPF, transient stability, MATLAB/Simulink, PSO.*

CHAPTER ONE

INTRODUCTION

1.1 Background of The Study

A power system is a highly intricate, nonlinear, and dynamic network, where its operational parameters are constantly varying over time. This dynamic behaviour often leads to frequent disturbances that can push the system toward instability. Such ongoing disruptions negatively impact the reliability of the power system and degrade its overall power quality (Kundur et al., 2003). Various forms of power system instability have arisen due to the growing complexity of interconnections, the integration of advanced control technologies, and the pursuit of higher performance under extreme operating conditions. In today's interconnected and commercialized power environment, modern power systems face significant challenges (Wang et al., 2014).

Power system stability refers to the system's ability to return to a balanced operating state following a physical disturbance, assuming a given initial condition. This stability ensures that most system variables remain within acceptable limits, thereby maintaining overall system integrity. Generally, system integrity is preserved when the majority of the power network stays operational, with minimal disconnection of generators or loads, limited only to those isolated due to faults or deliberately shut down to ensure the continued functioning of the remaining system. Instability occurs when a disturbance leads to a sustained mismatch between power generation and consumption. In essence, stability represents a condition where supply and demand are in equilibrium (Eremia & Shahidehpour, 2013).

The ability of the power system to remain synchronised following an abrupt and substantial disruption is known as transient stability. A sudden change in load, a generation outage, a system failure or the loss of a large load can all cause these disruptions (Songhao et al., 2019). A common bus that runs at the same frequency and phase sequence as the generators connects several synchronous generators in power plants. Throughout the generation and transmission process, constant synchronisation between the bus and the generators is necessary to guarantee stable operation (Kumar & Rammohan, 2020).

High-voltage transmission lines connect generating units to load centres as part of the power system, which is frequently controlled by mechanical means. System stability must be continuously maintained in order to operate transmission lines close to their thermal limits and make the best use of the generating resources that are available. An efficient solution is to use quick, dependable power electronic devices in place of mechanical controllers. The strategic use of FACTS devices, which greatly increase transient stability margins, can help achieve this. As more affordable ways to increase transmission capacity, enhance oscillation damping, and fortify system stability, FACTS technologies are being embraced more and more. By using them, the current transmission network can be used more effectively close to its thermal capacity, which eliminates the need to build new transmission lines. (Azra Hasanovic, 2000).

The Unified Power Flow Controller (UPFC) is the most adaptable of the different FACTS devices and has a great deal of potential to increase system stability. Both real and reactive power can be injected and absorbed by the UPFC. It is made up of two AC-to-DC converters, one of which is connected to the transmission line in series with a series transformer and the other in parallel with the line via a shunt transformer. A shared capacitor connects the converters' DC sides and provides the DC voltage required for them to function (Mihalic, Zunko, & Povh, Jan 1996).

1.2 Classification of Power System Stability

Based on the physical mechanism responsible for the instability, power system stability is classified into three major groups as depicted in the figure below.

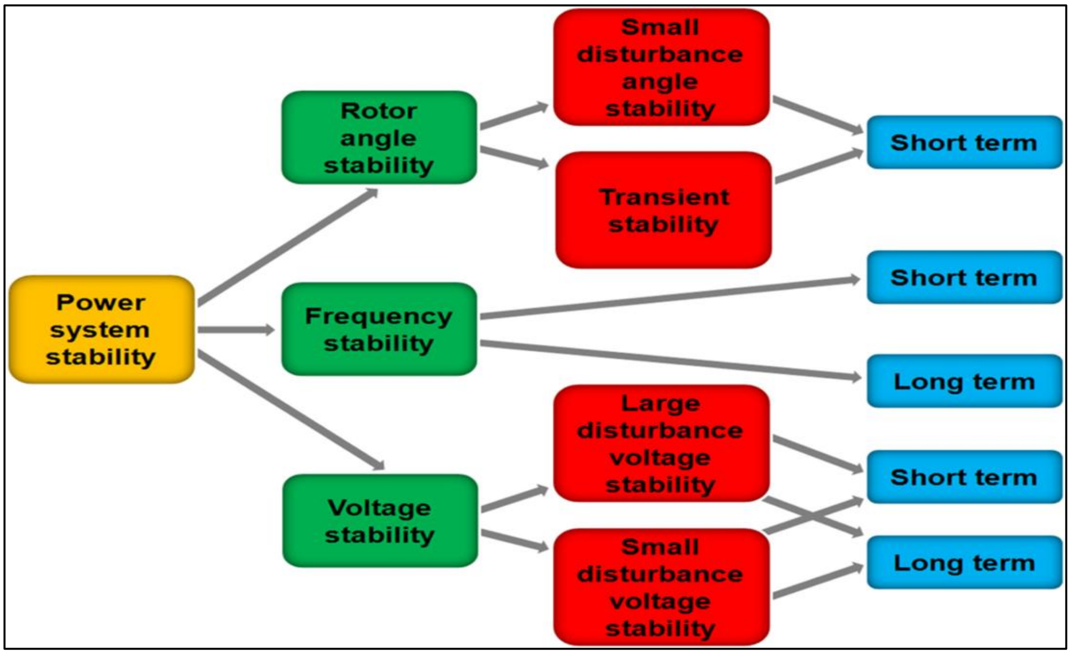

Figure1. 1: Classification of power system stability (Muttaqi, 2015)

1.2.1 Rotor Angle Stability

The ability of linked synchronous machines in a power system to maintain synchronisation through the balance of mechanical and electromagnetic torque is known as rotor angle stability. It focuses on how two synchronous generators operating in parallel to provide active power to the load are affected by the rotor angle of a generator (Wei et al., 2014).

Power system stability involves maintaining synchronism after disturbances. Small disturbances can be analyzed using linearized equations. Large disturbances require more complex methods, but the equal area criterion offers a graphical solution for a single machine connected to an infinite bus.

❖ 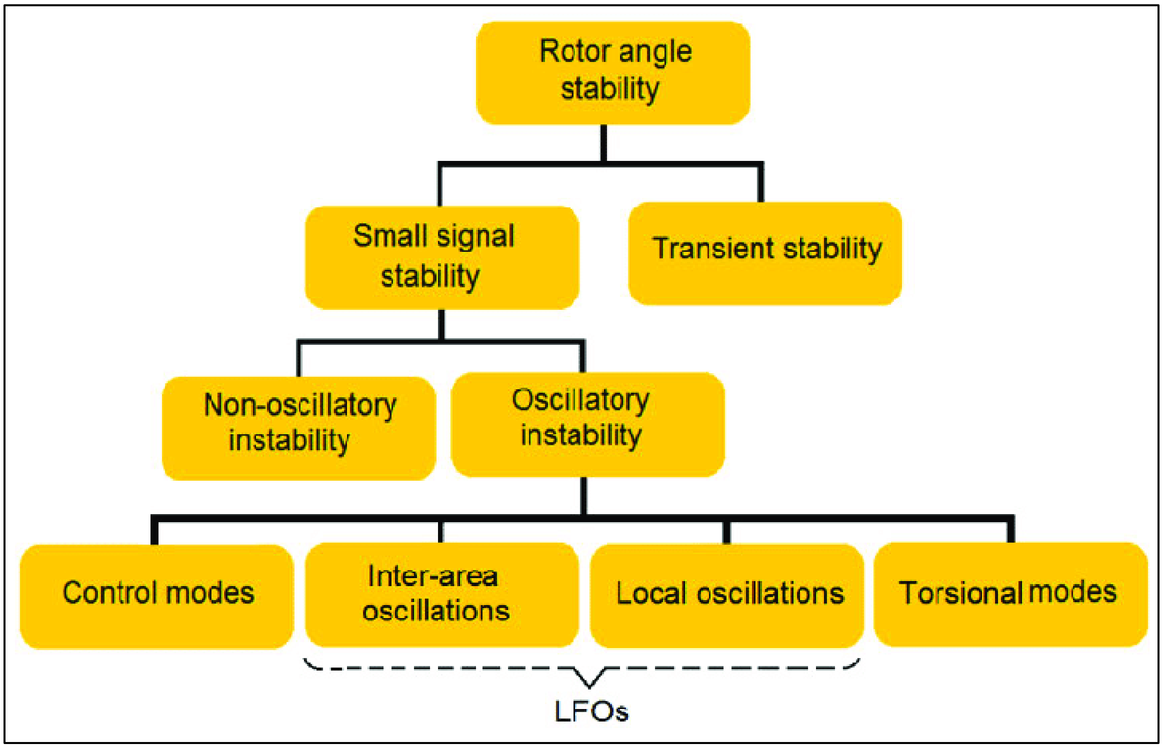

Figure1. 2: Classification of rotor angle stability (Saadatmand, 2020)

1.2.2 Voltage Stability

Voltage stability is a power system's ability to maintain acceptable voltage levels at all points, even after a disturbance. While typically stable, faults can cause voltage instability and a gradual, uncontrollable voltage drop (Shao & Tang, 2010).

Voltage instability can lead to voltage collapse, where critically low voltage levels cause blackouts. Voltage instability and voltage collapse are often used as synonyms. Voltage stability is generally classified into two types (Choudhary et al., 2020).

Voltage stability analysis comes in two main forms:

- ❖ Large Disturbance Voltage Stability: Focuses on maintaining voltage levels after major events (faults, outages) using simulations. This is a slower, long-term assessment.
- ❖ Small Disturbance Voltage Stability: Examines the system's reaction to minor disturbances. Stability is determined by positive V-Q sensitivity at buses. Negative sensitivity indicates instability and potential voltage collapse. This is analyzed using a small-signal approach.

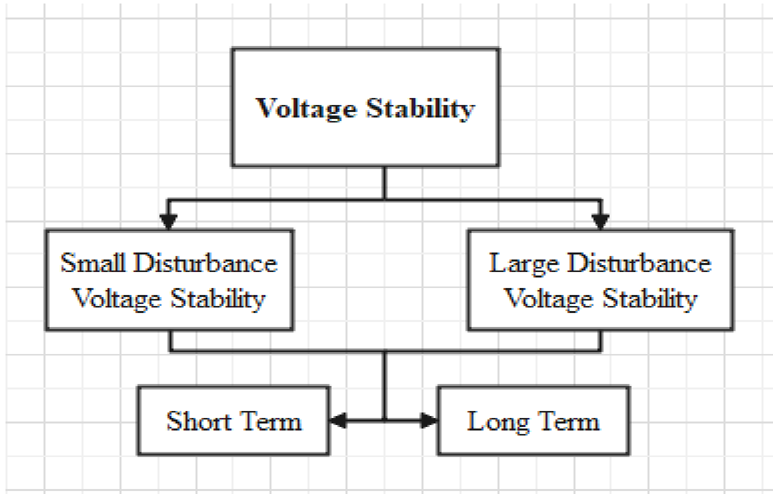

Figure1. 3: Classification of Voltage Stability (P. Kundur et al., 2004)

1.2.3 Frequency Stability

Frequency stability is the power system's ability to maintain a stable frequency after a major disturbance disrupts the balance between power generation and consumption. This imbalance causes system-wide frequency deviations. It's divided into short-term stability (immediately maintaining frequency) and long-term stability (restoring balance over time through actions like generator adjustments or load shedding) (Al-Mashhadani et al., 2020).

1.3 Statement of the Problem

The current energy markets, combined with economic and population growth and increasing power demand, are causing power systems to become more complex as they approach their maximum capacity limits. This complexity results in higher operational costs and, in extreme cases, puts the system at risk of partial failure or complete blackout. From a cost-effectiveness perspective, promptly addressing disturbances within the existing network should be prioritized over building new power plants. Transient instability presents serious challenges to power systems, including equipment damage, increased maintenance expenses, and decreased industrial production time. A key cause of power system instability is faults occurring in transmission lines.

This study investigates enhancing transient stability on the transmission line connecting the Adama II Wind Turbine and the Kality substation by employing a Neuro-Fuzzy controlled Unified Power Flow Controller. Integrating Wind turbines into the power grid poses stability challenges, particularly during transient disturbances like faults or sudden load changes in transmission lines that affect the turbines. When a transient fault occurs on the transmission line from the Adama II Wind farm to the Kality substation, the turbines at the Adama Wind power plant shut down completely. Since last year, the Adama II Wind turbines have experienced six disconnections due to transient problems, with 50 out of 102 units suffering major damage to turbine components such as pitch drivers, back-to-back converters, and generator slip rings.

This thesis uses an adaptive neuro-fuzzy-based Unified Power Flow Controller (UPFC), a quick and adaptable FACTS device, to improve the transient stability of the power system between the Adama II Wind Turbine and the Kality substation. Accurately determining the UPFC's size and location is essential for the study area's transient stability performance.

1.4 Objectives

1.4.1 General Objective

The main objective of this thesis is to investigate ways to enhance transient stability and minimize losses in the transmission line connecting the Adama II Wind Turbine with the Koka to Kality substation by implementing a neuro-fuzzy-based Unified Power Flow Controller.

1.4.2 Specific Objectives

- Assess the current network configuration and operating conditions of the high-voltage transmission system from Adama II Wind Turbine and Koka to Kality substation.
- Develop a mathematical model for the shunt, series, and DC components of the Unified Power Flow Controller (UPFC).
- Using Particle Swarm Optimisation (PSO) techniques, design and model the size of an ANFIS-based UPFC and ascertain its ideal location.
- Conduct a comparative analysis of the system's performance with and without the ANFIS-based UPFC, as well as with a conventional controller.
- Quantify the total loss reduction achieved by incorporating the ANFIS-based UPFC into the power system.

- Evaluate the cost implications of implementing the Unified Power Flow Controller before and after its integration into the system.

1.5 Significance of The Thesis

This research is highly significant for the sustainable growth and operational robustness of Ethiopia's electric power infrastructure, especially along the high-voltage transmission corridor from the Adama II Wind Farm to the Kality substation. By incorporating an intelligent Unified Power Flow Controller (UPFC) utilizing adaptive neuro-fuzzy inference systems, the study seeks to provide various technical and economic advantages.

These include:

- ✓ **Enhancing Grid Security and Stability:** By ensuring stable operation during severe transient disturbances, the study reduces the risk of system failure and improves the interconnected power system's security and dependability.
- ✓ **Mitigating Widespread Outages and Blackouts:** By enhancing transient response and managing power flow more effectively, the proposed solution decreases the chances of cascading failures that could result in widespread blackouts, thereby promoting greater system reliability.
- ✓ **Prolonging Equipment Lifespan:** By reducing intense electrical transients and mechanical strain on components, this approach prolongs the lifespan of both electrical and mechanical assets in the power system.
- ✓ **Minimizing Financial Losses in Industrial Sectors:** Regular power outages can cause significant economic damage, particularly in industries reliant on energy. This study seeks to minimize these losses by enhancing supply reliability and decreasing the necessity for costly equipment repairs or replacements.
- ✓ **Maximizing Transmission Line Efficiency:** The control strategy under consideration seeks to improve the power flow through the existing lines, making efficient use of the available resources while delaying the costs associated with building new transmission facilities.

1.6 Scope of The Study

The main objective of this dissertation is to design and implement a Unified Power Flow Controller (UPFC) utilizing an Adaptive Neuro-Fuzzy Inference System (ANFIS) to improve the transient stability of the interconnected tied transmission system Adama II Wind Farm and Koka to Kality substation. This paper involves (i) First, the design, optimal sizing, and dynamic modelling of the UPFC; (ii) the best location of the UPFC in the grid by means of PSO to provide the highest efficiency.

To evaluate the effectiveness of the suggested ANFIS-based UPFC, a comparative study is carried out against the conventional Proportional-Integral (PI)-based UPFC under different disturbance conditions. Important transient stability metrics, including percentage overshoot, settling time, and damping behaviour, are evaluated. Additionally, the effect of the UPFC on active power transfer throughout the high-voltage network is examined both prior to and following its implementation.

The complete system is modeled and validated using the MATLAB/SIMULINK platform, allowing for an in-depth evaluation of the UPFC's effectiveness in mitigating disturbances, stabilizing voltage, and enhancing overall power transfer efficiency. Through the application of advanced control strategies and optimization methods, this research presents a progressive solution to ongoing stability and reliability issues in Ethiopia's renewable energy-integrated power systems.

CHAPTER TWO

A REVIEW OF THE LITERATURE AND THEORY

2.1 Theory of The Case Study Area

The Ethiopian Electric Power (EEP) is a state-owned monopoly responsible for generating, transmitting, distributing, and selling electricity across Ethiopia. Established in 1956 E.C. as the Ethiopian Electric Power (EEP), it consolidated all electricity-related activities in the country under one organization. With over 50 years of service, the corporation now serves more than 2 million customers. Recently, EEP has begun exporting electricity to neighbouring countries like Djibouti and Kenya, earning a monthly revenue of 1.5 million dollars for supplying 35 megawatts. The corporation has plans to expand its export markets to other countries such as Sudan and Eritrea in the near future (Akele, Spring Semester2012)

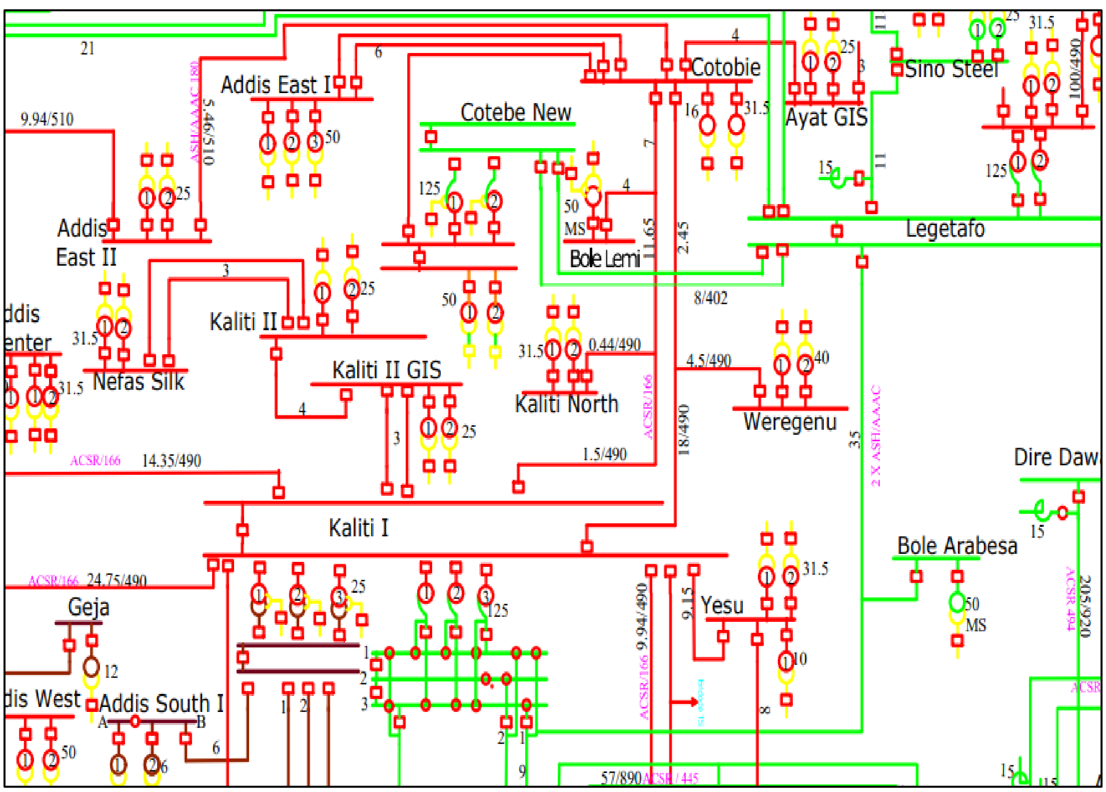

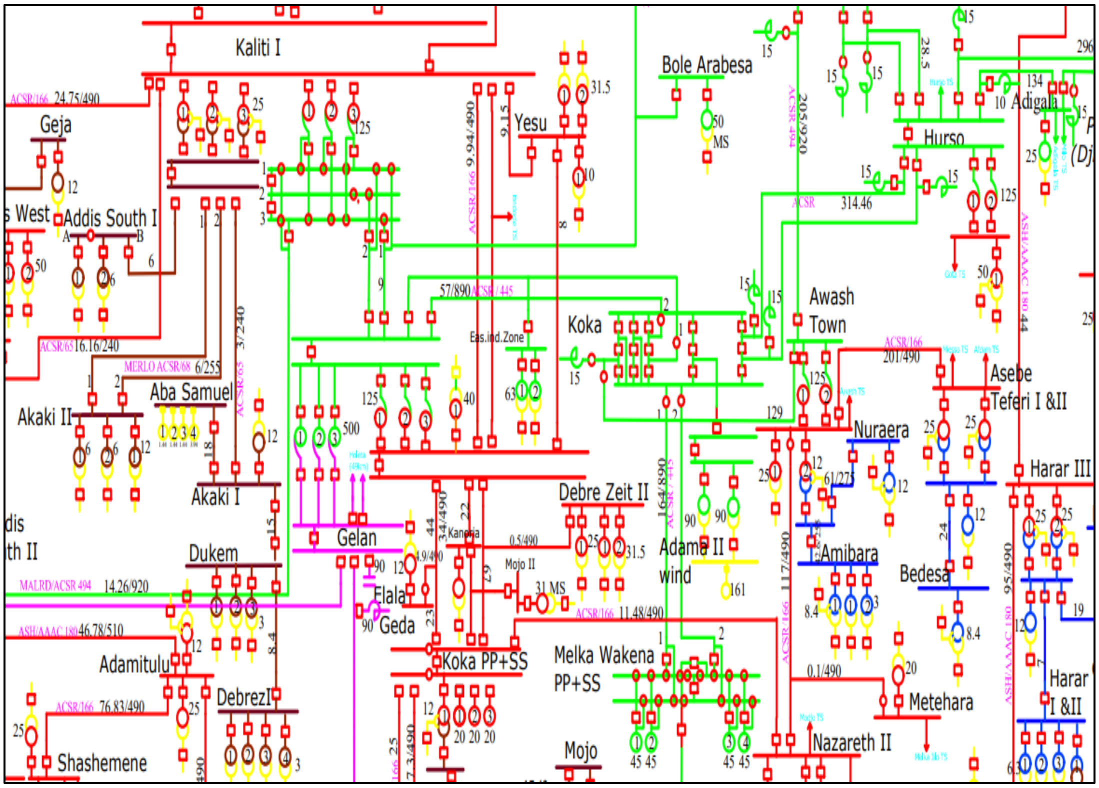

Figure2. 1: Adama II, Koka to Kality single line diagram from LDC Operational Planning and System study Department

Above is the single-line diagram of the Adama II, Koka to Kality power system, illustrating the principal connections of the components above 66 kV. In the diagram, pink represents 400 kV, red denotes 132 kV, blue signifies 66 kV, and green indicates 230 kV.

2.2 Literature Review

This section offers a summary of prior research efforts focused on improving transient stability. The knowledge gained from examining numerous research papers has proven to be extremely beneficial in the early design and simulation stages of this thesis, especially in the creation of a neuro-fuzzy-based unified power flow controller aimed at improving the transient stability of high-voltage transmission power systems.

((Li, 2024)in 2024 developed a nonlinear control approach for UPFCs using a A Transient Energy Function (TEF) and a Sliding Mode Observer (SMO) developed using local parameters.The method enabled accurate estimation of unobservable states and robust dynamic control during transient events. Simulation results showed improved damping performance and quicker system stabilization under various fault conditions, highlighting the method's potential for practical application in complex power systems.

(Muzaffer et al., 2017) Proposed Multi-machine system modelling, with shunt compensator and power system stabiliser support for improved transient stability. This paper's goal is to examine how two distinct mechanisms—power system stabilisers (PSS) and shunt compensation—can work in concert to increase both the voltage stability and the rotor angle stability. The patented design is slim and simple enough for real-world use. A power system stabilizer is connected to each generator for damping out rotor angle oscillations, and a shunt compensator is provided to maintain bus voltage. The power system is also known to provide for rapid and unpredictable load changes without impacting stability in a negative manner. But this paper only addresses an enhancement of transient stability at generation side. It could be possible to further study how generators react to disturbances on the transmission line.

(Kumar et al., 2015) discussion on the Enhancement of power system stability through the use of a unified power flow controller with hybrid fuzzy logic-pid tuning in an SMIB system. For stabilizer signal the output of identified model refernce of power system is compared with output of real power system and the error signal is input to one the input of a fuzzy based controller. The proposed controller offers a better damping property of the low-frequency oscillations. However, to analyze power system stability over a broad spectrum of the system, this paper concentrates.

(Benaissa et al., 2016) investigated the PSS and SVC's effects on the transient stability of the power system. The results demonstrate the successful development of a system for transient stability in a two-machine gearbox system with PSS and SVC. While the basic structure of a static var compensator operates under typical bus voltage control, the basic structure of a power system stabiliser operates under typical generator control.The findings of these studies show that the SVC has a great ability to dampen power system oscillations and improve the dynamic stability of the power system, while the selective of (PSS) can demonstrate adequate damping to the steady state oscillation and transient stability voltage performance across a broad range of operating conditions. SVC reacts more slowly than other voltages, though.

(Khurana & Titare, 2020) examined improvement of power flow and voltage stability using UPFC with artificial neural network in Matlab. The basic UPFC system utilises two separate system model architectures, STATCOM and SSSC, to compensate for high-voltage power transmission line voltage and current. Both are reusing higher voltage power transmission and consume more time period for power stablization. Hence, generating transmission impedance mismatching. This problem is solved by designing a UPFC using ANN algorithm simulation model. Artificial neural network gives a better result and, compared to previous UPFC controllers like PID and fuzzy logic, in terms of reducing settling time. ANN learning duration is higher in the case of huge training data or complicated systems.

(Mohanty & Pati, 2016) suggested STATCOM based on fuzzy logic controller for microgrid voltage profile enhancement. A STATCOM is used to enhance the voltage profile of the radial microgrid system that is based on a single alternator. PI and fuzzy logic controllers are the controllers used to control STATCOM. It is discovered that the fuzzy logic controller produces better results with a small steady state error, whereas the PI controller has a larger steady state error. Fuzzy logic controllers also reduce overshoots and settling time. Compared to traditional PI controllers, fuzzy logic controllers have a substantially lower voltage deviation caused by load changes. All of these results demonstrate that fuzzy logic controllers outperform traditional PI controllers in a wide range of load scenarios. However, fuzzy logic controller performance depends on the expert. If the expert assigns the wrong rules, then the fuzzy logic controller may provide poor performance even worse than PID controller.

(Das, Desmukh, & Sahu, 2016) examined the voltage stability improvement by using fuzzy logic controller in multimachine power system. The SVC with fuzzy logic controller has been tested in a 2-machine 3-bus power system where several parameters, including the difference of rotor angle between the machines, speed of the machines, terminal voltage and the transmission line active power, have been observed. The performance of the system implemented with the fuzzy based SVC controller. The system implemented with the fuzzy-SVC controller show better performance in damping oscillations, maintain terminal voltage, and controlling the power after the system is subjected to disturbance. However, in this work, the fuzzy based SVC controller has a deliberate dynamic response since its highly nonlinearity property causes the system to be uncertain to improve transient stability.

(Rahman et al., July 2012) examined the Stability Improvement of Power System by Using SVC With PID Controller. They present the stability improvement of voltage level, machine oscillation damping, real and reactive power in a power system model of SVC with and without properly tuned PID controller for different types of faulted conditions. The result shows PID is a very efficient controller for SVC to enhance the power system stability. However, in this work PID controller has an inadequacy in providing robust control over a wide range of power system operating conditions.

(M Nagahimaja et al., 2015) have studied the enhancement of transient stability in a multimachine power system using adaptive neuro-fuzzy controller for FACTs devices. In this paper, the Transient Stability improvement and Power Oscillation damping of a three-machine power system by various FACTS devices such as SSSC and UPFC, is analyzed. It is clear from the simulation results that there is a considerable improvement in the system performance with the presence of UPFC for which the settling time and amplitude of LFO is reduced when compared to SSSC and lead-lag, which shows that the proposed UPFC-based neuro-fuzzy controller provides efficient damping to power system oscillations and greatly improves the system voltage profile. But the system have large overshoot to damp the oscillation compared to ANFIS based UPFC.

(Khan & Bhowmick, 2015) examined a fuzzy TCSC controller to enhance transient stability. This study examines how well an FLC-based TCSC damping controller can increase a SMIB system's transient stability. The SMIB system is first examined without the TCSC. It was found that the system's clearing time was 0.086 seconds. A FLC-based TCSC damping controller was then used. The two inputs to the FLC were the rotor angle deviation and the rotor speed deviation. The output signal is the TCSC's firing angle deviation. It is found that the system's clearing time rises to 0.18 seconds when using the FLC-based TCSC damping controller. It has been noted that the system's transient stability has significantly improved. However, TCSC is a series compensator only, and it is investigated in SMIB only.

The researchers mentioned above have made significant contributions to improving transient stability using various FACTS devices, which naturally serve as the foundation for this thesis.

(Bose et al. , 2019) Conducted simulations using MATLAB/Simulink and reported that ANFIS-based UPFC outperforms conventional PI controllers in reducing the settling time and overshoot during transient events.

(Ali et al. , 2020) Compared ANFIS, fuzzy, and neural network controllers for UPFC and found ANFIS to be superior in terms of robustness and response time across various fault scenarios. This study aims to enhance the transient stability of the Adama II, Koka to Kality system by implementing an NFIS-based UPFC. Both shunt and series converters have been designed, and the optimal placement of the UPFC has been determined using particle swarm optimization. The performance of this controller is then compared to that of a conventional PI-based UPFC controller. Additionally, the power transfer capability of the UPFC and the total reduction in losses have been analyzed.

CHAPTER THREE

UNIFIED POWER FLOW CONTROLLER MODELLING AND DESIGN

3.1 Overview of FACTs Device

A system made up of stationary equipment intended for the alternating current (AC) transmission of electrical energy is known as a Flexible Alternating Current Transmission System (FACTS). Among various methods for enhancing transient stability, FACTS devices are crucial due to their fast response and soft switching capabilities, as they are based on power electronics. These devices improve the controllability and power transmission capacity of the network. Typically, power electronics form the core of the system. FACTS devices increase power transfer capacity, stability, and controllability when installed in AC transmission networks by providing series or shunt compensation (Imdadullah et al., 2020).

Before the development of power electronic switches, mechanical switches were used to connect capacitors, reactors, or synchronous generators to resolve these issues. However, mechanical switches have several drawbacks, including slow response times and susceptibility to wear and tear. These limitations made them unreliable for ensuring the stability and controllability of transmission lines. With the invention of power electronic switches, such as thyristors, which are capable of handling high-voltage applications, power electronics-based FACTS controllers were introduced to address these challenges more effectively (Peng, Nov. 2017). FACTS devices can be categorized into three types, depending on their arrangement in the transmission line and the kind of converter utilized.

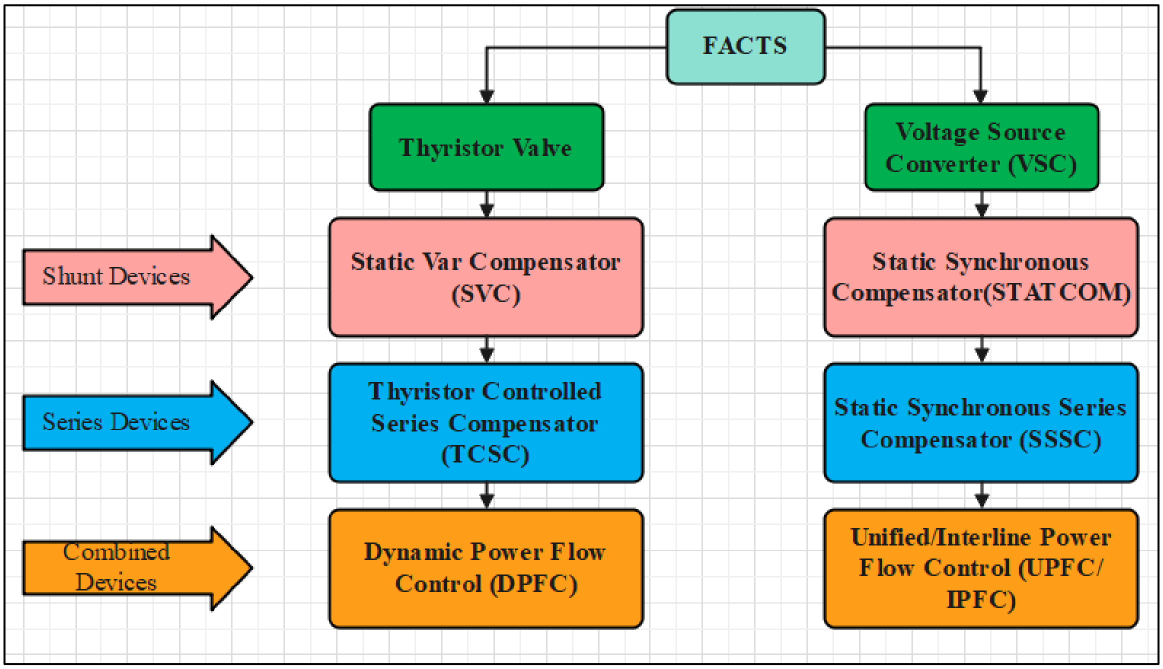

Figure3. 1: Classification of FACTs device (Dr. Abhishek Jain, 2018)

3.2 Overview of the UPFC and its Operation Principle

3.2.1 Introduction

Gyugyi first proposed the idea of the Unified Power Flow Controller (UPFC) in 1991. It can control all of the factors that affect power flow in a transmission line, such as voltage, impedance, and phase angle, either simultaneously or selectively. Two switching converters that are controlled by a common DC link make up the UPFC, a combined series-shunt controller (Baichao et al., 2018).

The UPFC consists of two converters arranged back-to-back, known as VSC1 and VSC2, which are energised by a DC link with a DC storage capacitor. These converters operate as an optimal AC-to-DC converter, enabling real power to move freely in both directions between the AC terminals of the converters. Each converter has the capability to independently produce or consume reactive power at its corresponding AC output terminal. (Yuan, et al., 2020).

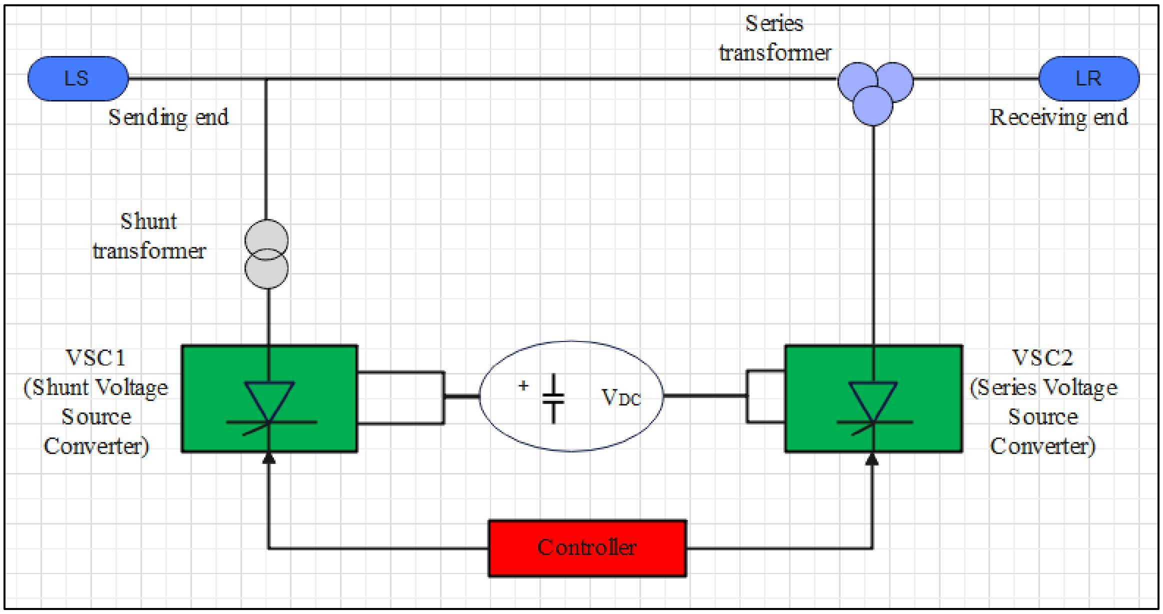

Figure3. 2: Basic UPFC schematic diagram (Vikas Gupta, 2011)

While VSC2 is connected in series with the transmission line via a series transformer, VSC1 is connected in parallel via a shunt transformer. Active power exchange is made possible between the two VSCs by their connection via DC terminals. VSC performs the main duty of the UPFC by injecting a voltage into the transmission line via an injection transformer with a controlled magnitude and phase angle. This injected voltage serves as a source of synchronous AC voltage (Wang, et al., 2020).

3.2.2 The Unified Power Flow Controller's Working Principle

As mentioned in Section 3.2.1, the voltage sources Vsh and Vse are produced by transforming DC voltage into AC voltage. Standard bridge circuits, which use GTOs as their basic building blocks, are used to accomplish this conversion process. These circuits are known as "voltage source converters (VSC)" because they change DC voltage into AC voltage. The VSC can control the phase angle and magnitude thanks to the control system that is attached to it. The VSC is also frequently referred to as an "inverter."Inverter 1 (VSC1) has the capability to charge the DC link capacitor (Balakrishnan et al., 2013). To understand the idea of unified power flow, picture a power system consisting of two machines connected by a transmission line that has a reactance of X_t (which is purely inductive). Furthermore, there are two voltage sources, Vsh and Vse, representing the

UPFC, as shown in Figure 3.3. The voltage sources Vsh and Vse are connected in shunt and series at the midpoint of the transmission line, respectively.

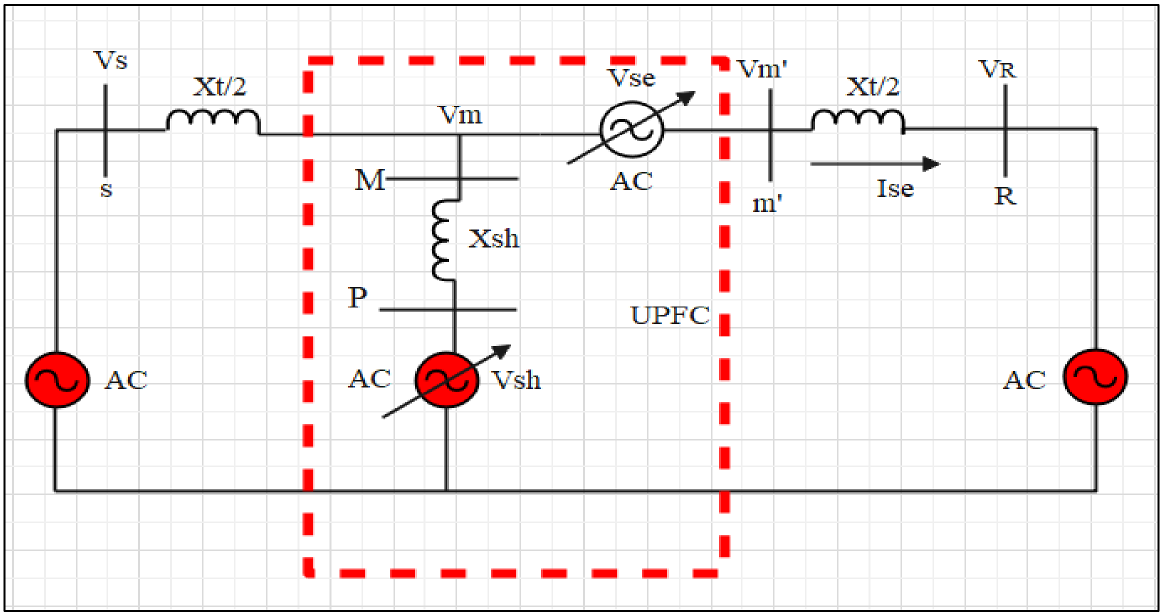

Figure3. 3: A transmission line connecting two machines in a power system with voltage sources vsh and vse that stand in for the UPFC

A transformer, represented by a reactance (Xsh), connects a voltage source (Vsh) to the transmission line. The voltage sources Vsh and Vse are presumed to be able to modify their phase angle and magnitude. The voltage source Vse is disconnected in order to comprehend how the voltage source Vsh operates. If the magnitude of Vsh is greater than the mid-point voltage Vm and their phases line up, reactive power will move from Vsh to bus M. Real and reactive power will move from Vsh to bus M if its phase angle is greater than Vm's and its magnitude is greater than Vm's (Sreenivasachar, 2001).

To summarize, by modifying the magnitude and phase angle of the shunt voltage source Vsh, it is possible to control the flow of both real and reactive power to bus M. The voltage source Vsh can function as either a load or a generator within the power system. When maintaining a zero phase angle difference between the voltage at bus M and that of Vsh, adjusting the magnitude of Vsh enables the system to either consume or generate reactive power. This operation resembles that of a thyristor-controlled reactor in combination with a fixed capacitor (shunt compensator), which alters its shunt reactive impedance to either absorb or produce reactive power.

Next, examining the operation of a series voltage source (Vse) with the shunt voltage source (Vsh) disconnected, we assume that both the magnitude and phase angle of the series voltage source (Vse) are adjustable. The current in the transmission line, denoted as Ise, interacts with Vse, resulting in the exchange of real and reactive power between the series voltage source and the transmission line. When the phase angle difference between the voltage source Vse and the transmission line current Ise is 90°, and if the voltage phasor of Vse leads the line current, then Vse will solely produce reactive power. The relevant phasor diagram is illustrated in Figure 3.4 below.

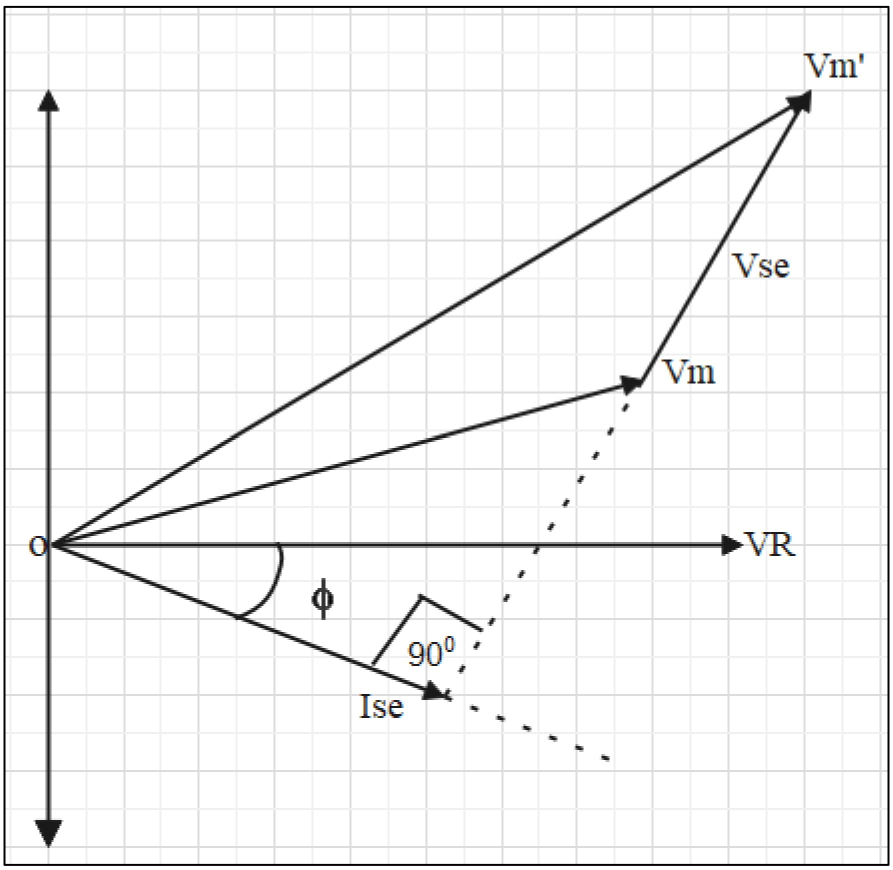

Figure3. 4: Phasor relationship for series compensation between the line current Ise and the voltage source Vse

On the other hand, if the phasor of the voltage source Vse lags behind the phasor of the transmission line current Ise by 90°, it indicates that the voltage source Vse is absorbing reactive power. This behavior is akin to that of a series capacitor or series inductor within the transmission line. When capacitors are introduced in series with the transmission line, they produce reactive power, and the quantity of reactive power generated is influenced by the degree of series compensation and the line current. Conversely, when inductors are added in series with the transmission line, they draw reactive power. In this scenario, the series voltage source Vse can act as a series capacitor by being ahead of the transmission line current Ise phasor by 90°. Alternatively, it can function as a series inductor by adjusting its phase angle to lag the line current Ise phasor by 90°. (Sreenivasachar, 2001).

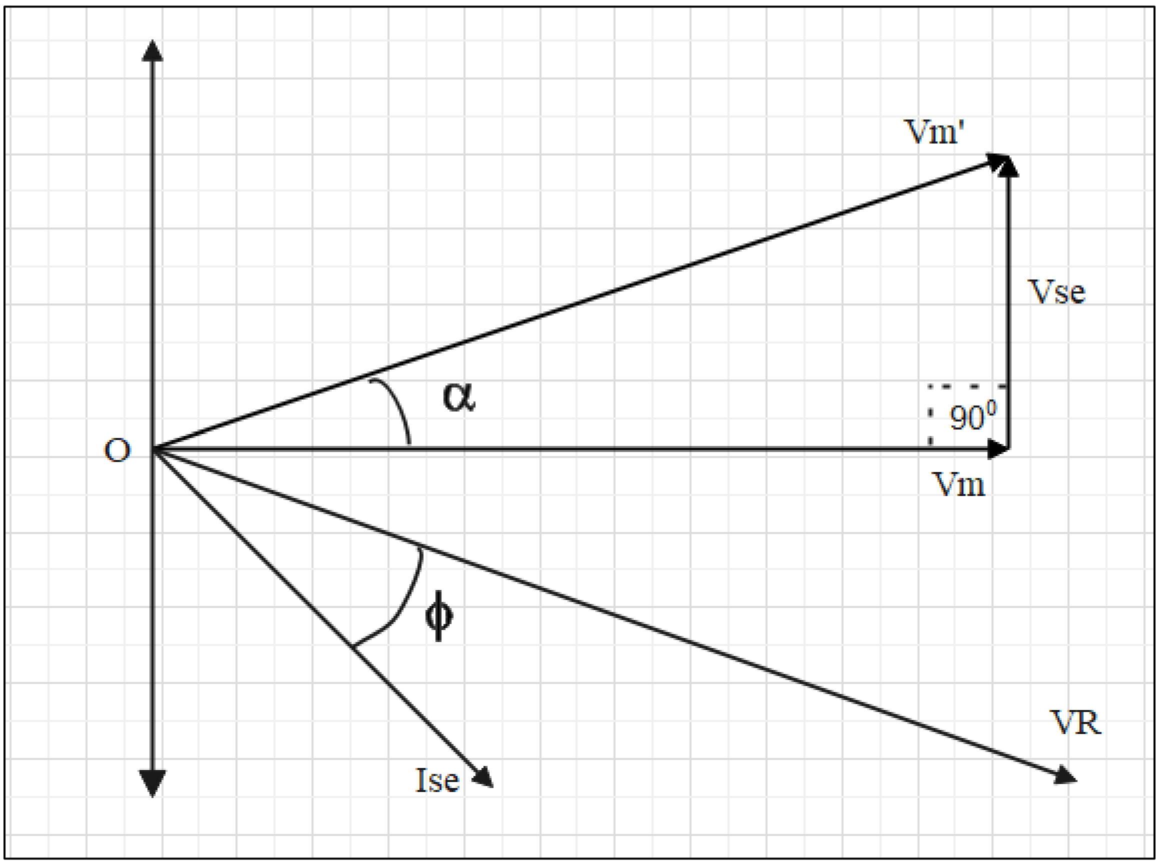

Figure3. 5: Phasor relationship between the series voltage source and the midpoint voltage, Vm, Vse, for the operation of a phase shifter

3.3 Mathematical Modelling of Unified Power Flow Controller

Figure 3.6 illustrates a standard circuit for a unified power flow controller. In order to improve transient stability, the control objectives in this system include controlling the real (P) and reactive (Q) power flows within the transmission line, as well as the voltage magnitude $|v_1|$. By injecting a leading or lagging current at the connection point, the shunt device controls $|v_1|$. In the meantime, by adding the proper voltage to the gearbox line, the series device controls the power flow (P and Q) in the system. This device makes it easier to exchange reactive power locally with the DC capacitor bank and real power with the system. Additionally, the shunt device provides the active power that the series device injects into the line through the DC capacitor bank.

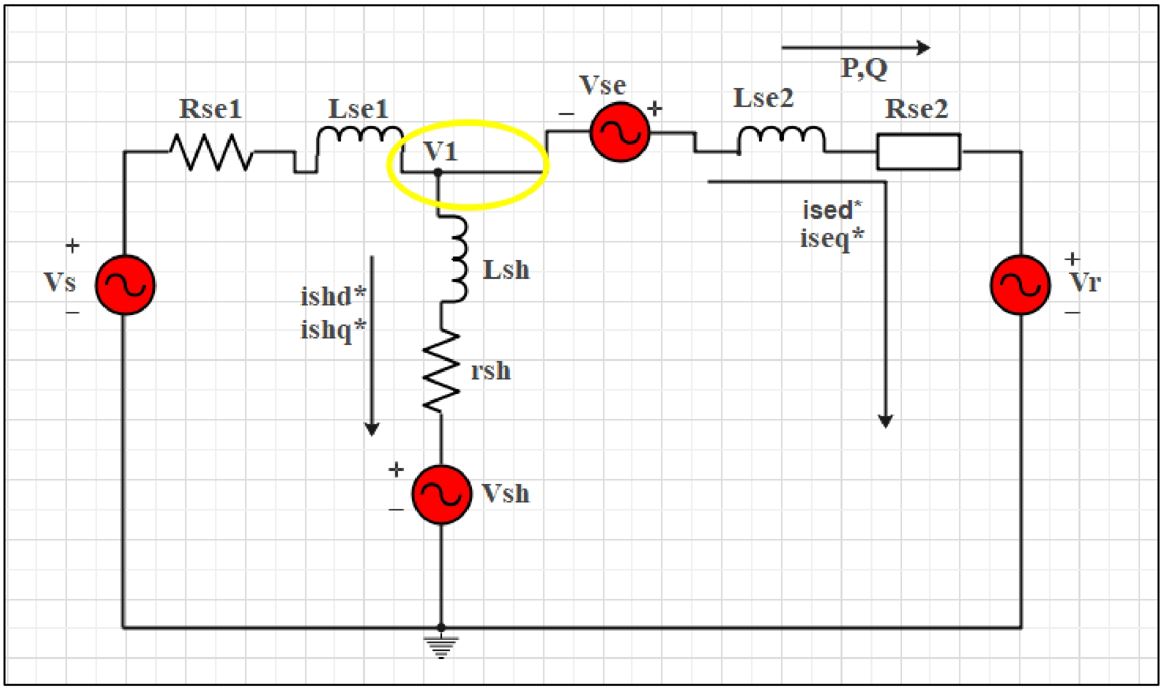

Figure3. 6: Representation of power flow in a UPFC using a single-phase circuit (Samal & Panda, 2014)

3.3.1 Mathematical Modelling of Shunt Converter

A shunt device model is depicted in Figure 3.7 below, with a voltage source V_1, shunt resistor r_sh and shunt inductor L_sh.

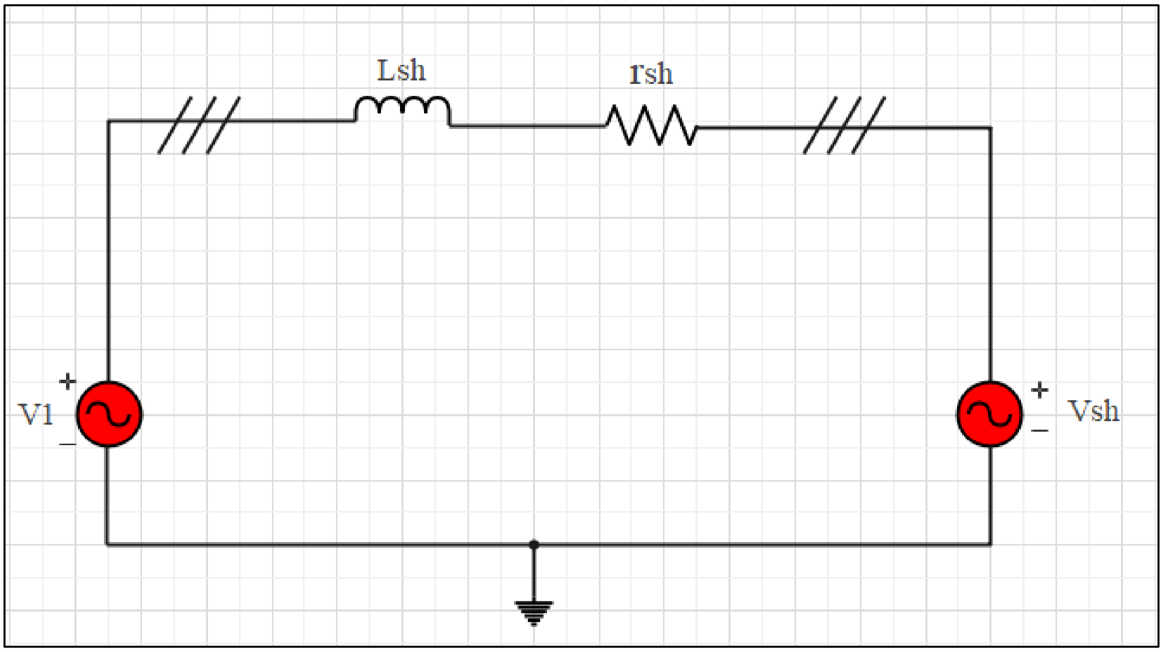

Figure3. 7: UPFC shunt device model

As shown in Figure 3.7, the differential equation for the shunt converter in the a-b-c reference axis system is derived. The equation from the circuit is expressed as follows:

$$\begin{cases} V_{1a} - V_{sha} = r_{sh} i_{sha} + L_{sh} \frac{d}{dt} i_{sha} \\ V_{1b} - V_{shb} = r_{sh} i_{shb} + L_{sh} \frac{d}{dt} i_{shb} \\ V_{1c} - V_{shc} = r_{sh} i_{shc} + L_{sh} \frac{d}{dt} i_{shc} \end{cases} \tag{3.1}$$

The equation (3.1) can be expressed in a different form by rearranging it:

$$\begin{cases} \frac{d}{dt} i_{sha} = \frac{V_{1a} - r_{sh} i_{sha} - V_{sha}}{Lsh} \\ \frac{d}{dt} i_{shb} = \frac{V_{1b} - r_{sh} i_{shb} - V_{shb}}{Lsh} \\ \frac{d}{dt} i_{shc} = \frac{V_{1c} - r_{sh} i_{shc} - V_{shc}}{Lsh} \end{cases} \tag{3.2}$$

In matrix format, the equation (3.2) can be organized as:

$$\frac{d}{dt}\begin{bmatrix} i_{sha} \\ i_{shb} \\ i_{shc} \end{bmatrix} = \begin{bmatrix} -\frac{r_{sh}}{L_{sh}} & 0 & 0 \\ 0 & -\frac{r_{sh}}{L_{sh}} & 0 \\ 0 & 0 & -\frac{r_{sh}}{L_{sh}} \end{bmatrix}\begin{bmatrix} i_{sha} \\ i_{shb} \\ i_{shb} \end{bmatrix} + \frac{1}{L_{sh}}\begin{bmatrix} V_{1a} - V_{sha} \\ V_{1b} - V_{shb} \\ V_{1c} - V_{shc} \end{bmatrix} \quad (3.3)$$

Here, the shunt voltages for phases a, b, and c are indicated by the symbols V_(sha), V_shb, and V_shc, respectively. Likewise, the node voltages for phases a, b, and c are denoted by V_(1a), V_1b, and V_1c. In the meantime, the shunt currents for phases a, b, and c are denoted by i_(sha), i_shb, and i_shc. R_sh and L_sh, respectively, represent the shunt resistance and inductance.

It is possible to convert a three-phase system into the d-q axis representation by applying Park's transformation rule. To make calculations easier, this transformation converts the three-phase system's time-domain components from the a-b-c reference frame to direct, quadrature, and zero components within a rotating reference frame. Let T(ωt) be the transformation ratio of Park's method.) (Abdelkrim et al., 2012).

$$T\,(\omega t) = \frac{2}{3}\begin{bmatrix} \cos(\omega t) & \cos(\omega t - 120°) & \cos(\omega t + 120°) \\ -\sin(\omega t) & -\sin(\omega t - 120°) & -\sin(\omega t + 120°) \\ \frac{1}{2} & \frac{1}{2} & \frac{1}{2} \end{bmatrix} \quad (3.4)$$

Three phase voltage parks transformation from three phase *abc* to *dq0* using Park's transformation ratio be T (ωt) can be written as V_{dq0}= T (ωt)* V_{abc}.

$$\begin{bmatrix} Vd \\ Vq \\ V0 \end{bmatrix} = \frac{2}{3}\begin{bmatrix} \cos(\omega t) & \cos(\omega t - 120°) & \cos(\omega t + 120°) \\ -\sin(\omega t) & -sin(\omega t - 120°) & -sin(\omega t + 120°) \\ \frac{1}{2} & \frac{1}{2} & \frac{1}{2} \end{bmatrix}\begin{bmatrix} Va \\ Vb \\ Vc \end{bmatrix} \quad (3.5)$$

Likewise, for three phase current parks transformation from three phase a-b-c to d-q-0 using Park's transformation ratio be T (ωt) can be written as i_{dq0}= T (ωt)*i_{abc}.

$$\begin{bmatrix} id \\ iq \\ i0 \end{bmatrix} = \frac{2}{3}\begin{bmatrix} \cos(\omega t) & \cos(\omega t - 120°) & \cos(\omega t + 120°) \\ -\sin(\omega t) & -\sin(\omega t - 120°) & -\sin(\omega t + 120°) \\ \frac{1}{2} & \frac{1}{2} & \frac{1}{2} \end{bmatrix}\begin{bmatrix} ia \\ ib \\ ic \end{bmatrix} \quad (3.6)$$

Using calculus derivative product rule:

$$\frac{d}{dt}\begin{bmatrix} i_d \\ i_q \\ i_0 \end{bmatrix} = \frac{d}{dt}\left(T(\omega t)\begin{bmatrix} i_a \\ i_b \\ i_c \end{bmatrix}\right) = \frac{d}{dt}T(\omega t) * \begin{bmatrix} i_a \\ i_b \\ i_c \end{bmatrix} + T(\omega t) * \frac{d}{dt}\begin{bmatrix} i_a \\ i_b \\ i_c \end{bmatrix} \quad (3.7)$$

Substituting equation (3.3) into equation (3.7) for shunt converter will be:

$$\frac{d}{dt}\begin{bmatrix} i_{shd} \\ i_{shq} \\ i_{sh0} \end{bmatrix} = T'(\omega t) * \begin{bmatrix} i_{sha} \\ i_{shb} \\ i_{shc} \end{bmatrix} + T(\omega t) * \frac{d}{dt}\begin{bmatrix} i_{sha} \\ i_{shb} \\ i_{shc} \end{bmatrix} \quad (3.8)$$

Next, convert equation (3.3) into the d-q-0 system. It is assumed that the zero axis is symmetric in this instance. Therefore, only the d-q reference can be expressed as follows when the zero axis component is ignored:

$$\frac{d}{dt}\begin{bmatrix} i_{shd} \\ i_{shq} \end{bmatrix} = \begin{bmatrix} -\frac{r_{sh}}{L_{sh}} & \omega \\ -\omega & -\frac{r_{sh}}{L_{sh}} \end{bmatrix} * \begin{bmatrix} i_{shd} \\ i_{shq} \end{bmatrix} + \frac{1}{L_{sh}}\begin{bmatrix} V_{1d} - V_{shd} \\ V_{1q} - V_{shq} \end{bmatrix} \quad (3.9)$$

- In this context, V_{shd}, V_{shq}, and V_{sh0} represent the shunt voltage on the direct axis, quadrature axis, and zero axis, respectively. Similarly, V_{1d}, V_{1q}, and V_{10} denote the node voltage components for the direct axis, quadrature axis, and zero axis. The direct axis, quadrature axis, and zero axis shunt current are represented by i_(shd), i_shq, and i_sh0, respectively. Additionally, r_sh and L_sh refer to the shunt resistance and inductance.
- The d and q components of first-order time-varying currents can be expressed as follows using equation (3.9).
- The d-component of shunt current is:

$$\frac{d}{dt}[i_{shd}] = -\frac{r_{sh}}{L_{sh}} * i_{shd} + \omega i_{shq} + \frac{1}{L_{sh}}(V_{1d} - V_{shd}) \quad (3.10)$$

- The q-component of shunt current is:

$$\frac{d}{dt}[i_{shq}] = -\omega i_{shd} - \frac{r_{sh}}{L_{sh}} * i_{shq} + \frac{1}{L_{sh}}(V_{1q} - V_{shq}) \quad (3.12)$$

Where, $\omega=2\pi f$, f the fundamental frequency of the supply voltage.

3.3.2 Reference to the Shunt Converter Control Variable

This section explains how operator inputs and power system data are used by the system control block to determine the reference signals for the functional control block. The sending end bus voltage $|v_1|$ is controlled by reactive power injection from a shunt device. As a result, a PI controller that sets the reference value can control the reactive power injection $Q_{sh.}$ represented by the star symbol (*) as superscript (Li, Qiang, 2006).

$$Q_{sh}{}^{*} = (\frac{k_{iv}}{s} + k_{pv})(|v_1|^{*} - |v_1|) \tag{3.13}$$

The d-axis voltage component matches the instantaneous voltage magnitude when the rotating axis aligns with the sending end voltage. As a result, we have (|v_1| = v_{1d}). As a result, the shunt branch's reference current on the q-axis can be written as follows:

$$i_{shq}{}^{*} = \frac{Q_{sh}{}^{*}}{v_{1d}} \tag{3.14}$$

Substituting equation (3.13) into equation (3.14) will give:

$$i_{shq}{}^{*} = \frac{(\frac{k_{iv}}{s} + k_{pv})(|v_1|^{*} - |v_1|)}{v_{1d}} \tag{3.15}$$

The series converter's active power has been depleted by the d-axis reference current for the shunt branch. The actual shunt converter current component is also in charge of causing power losses in the DC capacitor and switching devices. Maintaining a steady DC capacitor voltage reflects this.

$$i_{shd}{}^{*} = \frac{P_{se}{}^{*}}{v_{1d}} + (k_{pDC} + \frac{k_{iDC}}{s})(v_{DC}{}^{*} - v_{DC}) \tag{3.16}$$

Where V_{1d} is the voltage at the connection point's d-axis component. $P_{se}{}^{*} = v_{sed}i_{sed} + v_{seq}i_{seq}$ is the instantaneous actual power that the series converter injects into the transmission line. v_sed and v_seq represent the injected voltage's actual and reactive components, respectively. i_sed and i_seq represent the line current's actual and reactive components, respectively. For the PI controller, k_pDC and k_iDC stand for integral and proportional gain, respectively. Through the DC capacitor, the shunt converter provides the actual power required by the series converter.

Through the DC capacitor, the shunt converter provides the actual power required by the series converter. Figure 3.8 below provides an illustration of the shunt current reference calculating procedure:

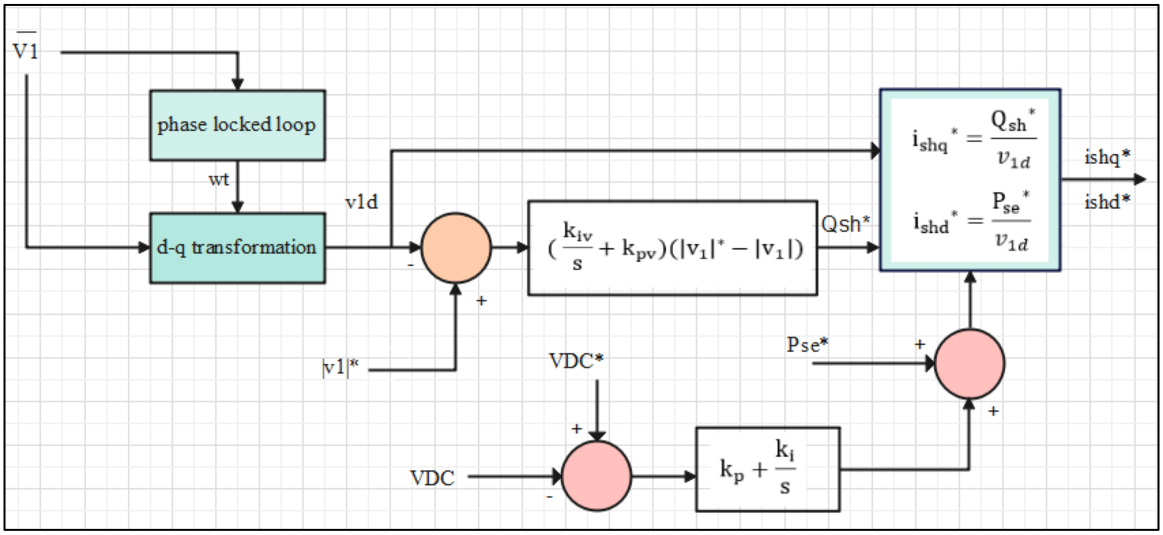

Figure3. 8: For the computation of the shunt current reference

3.3.3 Series Converter Mathematical Modelling

The series converter's mathematical modelling process is identical to that of the shunt converter. Figure 3.9 below shows how Kirchhoff's Voltage Law (KVL) is used to dynamically model a series converter for a three-phase system that is balanced. A voltage source with series resistance (Rse) and inductance (Lse) is used to represent this dynamic modelling on a per-phase basis.

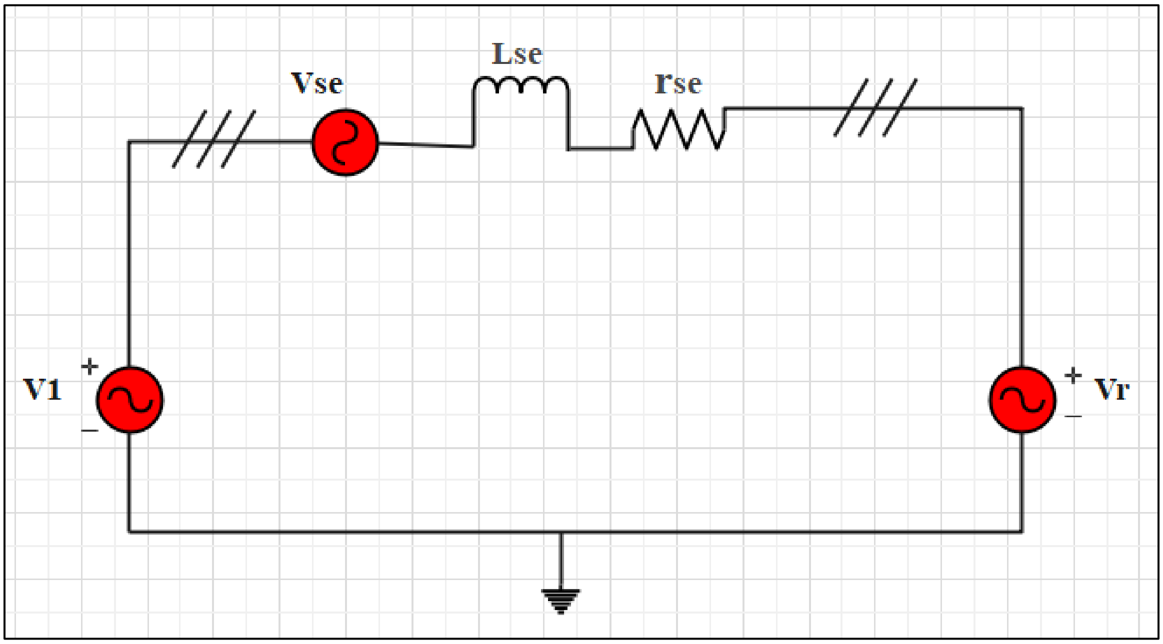

Figure3. 9: The UPFC series device model

The differential equation for the series converter in the system with the a-b-c axes, as shown in Figure 3.9, yields the following set of equations for three-phase circuits:

$$\begin{cases} V_{1a} + V_{sea} - V_{ra} = R_{se} i_{sea} + L_{se} \frac{d}{dt} i_{sea} \\ V_{1b} + V_{seb} - V_{rb} = R_{se} i_{seb} + L_{se} \frac{d}{dt} i_{seb} \\ V_{1c} + V_{sec} - V_{rc} = R_{se} i_{sec} + L_{se} \frac{d}{dt} i_{sec} \end{cases} \quad (3.17)$$

Rearranging equation (3.17), It can be expressed as:

$$\begin{cases} \frac{d}{dt} i_{sea} = \frac{V_{1a} + V_{sea} - V_{ra} - R_{se} i_{sea}}{Lsh} \\ \frac{d}{dt} i_{seb} = \frac{V_{1b} + V_{seb} - V_{rb} - R_{se} i_{seb}}{Lsh} \\ \frac{d}{dt} i_{sec} = \frac{V_{1c} + V_{sec} - V_{rc} - R_{se} i_{sec}}{Lsh} \end{cases} \quad (3.18)$$

It is possible to arrange equation (3.18) in matrix form as:

$$\frac{d}{dt} \begin{bmatrix} i_{sea} \\ i_{seb} \\ i_{sec} \end{bmatrix} = \begin{bmatrix} -\frac{R_{se}}{L_{se}} & 0 & 0 \\ 0 & -\frac{R_{se}}{L_{se}} & 0 \\ 0 & 0 & -\frac{R_{se}}{L_{se}} \end{bmatrix} \begin{bmatrix} i_{sea} \\ i_{seb} \\ i_{seb} \end{bmatrix} + \frac{1}{L_{se}} \begin{bmatrix} V_{1a} + V_{sea} - V_{ra} \\ V_{1b} + V_{seb} - V_{rb} \\ V_{1c} + V_{sec} - V_{rc} \end{bmatrix} \quad (3.19)$$

Where, $V_{sea,}$ V_{seb} and V_{sec} are the series voltages for phases A, B, and C, respectively. $V_{1a,}$ V_{1b} and V_{1c}. The node voltages are phases a, b, and c, respectively. $V_{ra,}$ V_{rb} and V_{rc} are, respectively, the receiving end voltages for phases a, b, and c. $i_{sha,}$ i_{shb} and i_{shc} are the phases a, b and c current respectively. R_{sh} and L_{sh} are the shunt resistance and inductance, respectively.

Following the same procedure of shunt converter,transform equation (3.19) into d-q-0 system. In this case,the zero axis is assumed to be symmetric.Therfore, neglecting zero axis component only d-q reference can be written as follows :

$$\frac{d}{dt}\begin{bmatrix} i_{sed} \\ i_{seq} \end{bmatrix} = \begin{bmatrix} -\frac{R_{se}}{L_{se}} & \omega \\ -\omega & -\frac{R_{se}}{L_{se}} \end{bmatrix} * \begin{bmatrix} i_{sed} \\ i_{seq} \end{bmatrix} + \frac{1}{L_{se}} \begin{bmatrix} V_{1d} + V_{sed} - V_{rd} \\ V_{1q} + V_{seq} - V_{rq} \end{bmatrix} \tag{3.20}$$

Where, $V_{sed,}$ V_{seq} and V_{se0} are series voltages on the direct, quadrature, and zero axes, respectively. $V_{1d,}$ V_{1q} and V_{10} are the node voltages' direct, quadrature, and zero axes, in that order. $V_{rd,}$ V_{rq} and V_{r0} are the receiving end voltages zero, quadrature, and direct axes, accordingly. $i_{sed,}$ i_{seq} and i_{se0} are zero axis current, quadrature axis current, and direct axis current, in that order. R_{se} and L_{se} are the series resistance and inductance respectively. From equation (3.20), the d and q elements of first-order time-varying currents can be written as follows.

- The series converter current's d-component is:

$$\frac{d}{dt}[i_{sed}] = -\frac{R_{se}}{L_{se}} * i_{sed} - \omega i_{seq} + \frac{1}{L_{se}}(V_{1d} - V_{sed} - V_{rd}) \tag{3.21}$$

- The series converter current's q-component is:

$$\frac{d}{dt}[i_{seq}] = \omega i_{seq} - \frac{R_{se}}{L_{se}} * i_{seq} + \frac{1}{L_{se}}(V_{1d} - V_{seq} - V_{rd}) \tag{3.22}$$

3.3.4 Series Converter Control Variable Reference

The d-q transformation allows for independent regulation of the real and reactive power transmitted to the receiving end bus. At the receiving end, the voltage Vrd is synchronized with the rotating axis. Therefore, $P_{se}{}^{*} = V_{rd} i_{sed}{}^{*}$, $Q_{se}{}^{*} = V_{rd} i_{seq}{}^{*}$. where, V_{rd} is the receiving end voltage's d-axis component. $i_{sed}{}^{*}$ and $i_{seq}{}^{*}$ are the line current's reference real and reactive components, correspondingly. The transmission line's d-axis and q-axis reference currents are thus determined using equation (3.23). Figure 3.10 shows the computing procedure.

$$\begin{cases} i_{sed}{}^{*} = \dfrac{P_{se}{}^{*}}{V_{rd}} \\ i_{seq}{}^{*} = \dfrac{Q_{se}{}^{*}}{V_{rd}} \end{cases} \tag{3.23}$$

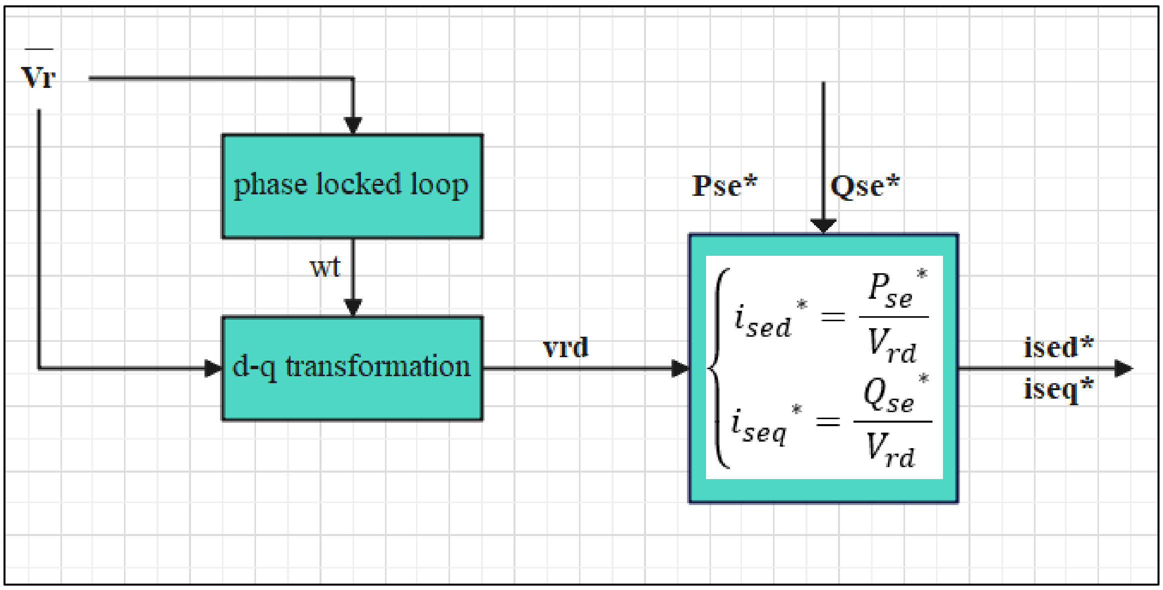

Figure3. 10: Series current reference computation

3.3.5 Mathematical Modelling of DC Link Capacitor

The model in Figure 3.11 illustrates how the voltage of the DC capacitor bank is determined by the actual power supplied and absorbed by the shunt and series devices.

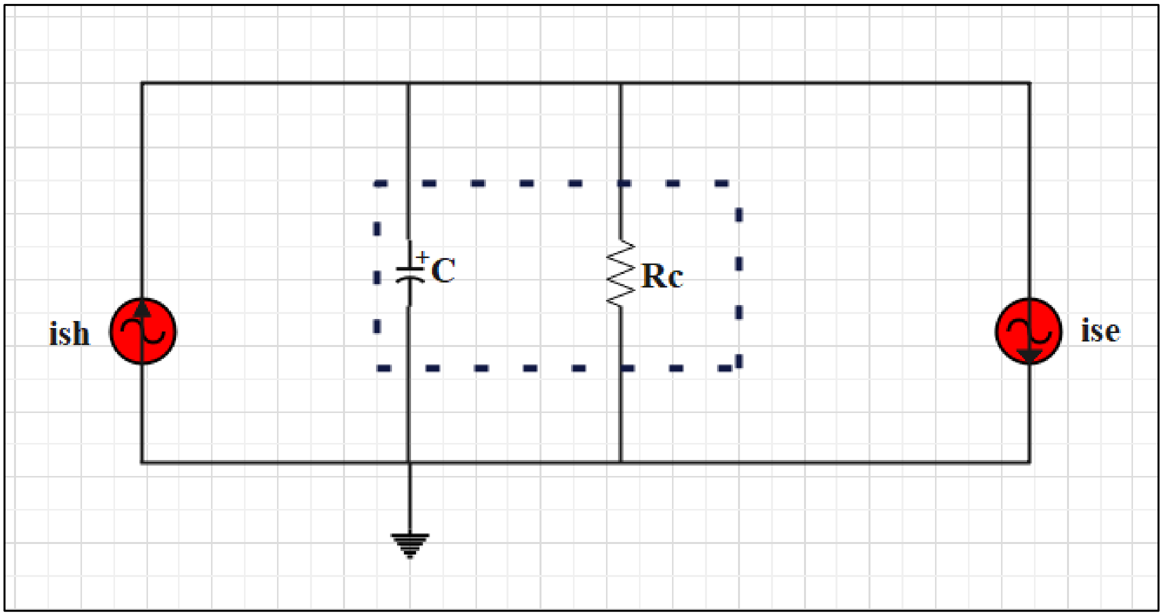

Figure3. 11: Model for controlling the voltage of DC link capacitors

$R_c$losses of the DC capacitor, series device, and shunt device, which are represented as a shunt connected resistance with the DC capacitor. The capacitor's positive side node current can be expressed as:

$$i_{sh} - i_{se} = \mathrm{C}\frac{d}{dt}V_{dc} + \frac{V_{dc}}{R_c} \tag{3.24}$$

where the currents drawn by the shunt and series converters are denoted by i_{sh} and i_{se}, respectively. The currents are determined by the actual power that is supplied or drawn by the shunt and series devices. Equation (3.24), therefore, can be updated as follows:

$$\frac{P_{sh} - P_{se}}{V_{dc}} = \mathrm{C}\frac{d}{dt}V_{dc} + \frac{V_{dc}}{R_c} \tag{3.25}$$

The actual power delivered by the shunt converter is represented by equation (3.26):

$$P_{sh} = V_{shd}i_{shd} + V_{shq}i_{shq} \tag{3.26}$$

Equation (3.27) represents the actual power that the series converter draws:

$$P_{se} = V_{sed} i_{sed} + V_{seq} i_{seq} \tag{3.27}$$

In equation (3.25), substitute equations (3.26) and (3.27):

$$\frac{V_{shd} i_{shd} + V_{shq} i_{shq} - V_{sed} i_{sed} - V_{seq} i_{seq}}{V_{dc}} = C \frac{d}{dt} V_{dc} + \frac{V_{dc}}{R_c} \tag{3.28}$$

Reorganize the equation (3.28), it can be written as:

$$\frac{d}{dt} V_{dc} = \frac{V_{shd} i_{shd} + V_{shq} i_{shq} - V_{sed} i_{sed} - V_{seq} i_{seq}}{C V_{dc}} - \frac{V_{dc}}{C R_c} \tag{3.29}$$

It is possible to express the shunt and series converter output voltage d-q components without accounting for the voltage harmonics brought on by the inverter switching:

$$\begin{bmatrix} V_{shd} \\ V_{shq} \\ V_{sed} \\ V_{seq} \end{bmatrix} = V_{dc} \begin{bmatrix} k_{sh} cos\delta_{sh} \\ k_{sh} sin\delta_{sh} \\ k_{se} cos\delta_{se} \\ k_{se} sin\delta_{se} \end{bmatrix} \tag{3.30}$$

Where k_{sh} and k_{se} are the constants that govern how the shunt and series converters relate to the DC voltage. It combines the modulation index of the shunt and series converter with the transformer turns ratio. The phase angle between the fundamental voltage of the shunt and series converter output and the reference voltage, usually the bus voltage at the sending or receiving end, is denoted by δ_{sh} and δ_{se}. (Li, Qiang, 2006).

Substituting equation (3.30) into (3.29), will give (3.31):

$$\frac{dV_{dc}}{dt} = \frac{k_{sh} cos\delta_{sh} i_{shd} + k_{sh} sin\delta_{sh} i_{shq} - k_{se} cos\delta_{se} i_{sed} - k_{se} sin\delta_{se} i_{seq}}{C} - \frac{V_{dc}}{C R_c} \tag{3.31}$$

3.4 Controller Design of Unified Power Flow Controller

The UPFC uses shunt and series converters controlled to manage real and reactive power and improve transient stability. The controllers rely on both reference values based on steady-state system characteristics and real-time measurements. The synchronous D-Q frame is used for control design and modelling, with converter output voltages driving a pulse width modulator to generate firing pulses. The DC link capacitor, series converter, and shunt converter models can be combined into a state-space representation.:

$$\begin{cases} \dot{x} = Ax + Bu \leftarrow \text{state equation} \\ y = Cx + Du \leftarrow \text{output equation} \end{cases} \tag{3.32}$$

A dynamic system's behavior can be described using state variables (x), input variables (u), and matrices (A, B, C, D). These matrices define how the system's dynamics depend on state variables (A), input variables (B), output variables (C), and direct input transitions (D). Applying this to a UPFC, a complex, nonlinear system, simplification is achieved by assuming a constant DC capacitor voltage, reducing the system to a fourth-order model. Further, transient stability can be improved by independently managing the shunt and series converter controls based on the state-space equation. (Li, Qiang, 2006).

3.4.1 Controller Design of Shunt Converter

In the transformation of the shunt controller to state space representation, the connection point voltage V_1 is synchronised with the rotating d-q axis. Thus, $V_{1d} = |V_1|$, and $V_{1q} = 0$. Equation (3.9) should be rearranged as follows (Li, Qiang, 2006):

$$\frac{d}{dt}\begin{bmatrix} i_{shd} \\ i_{shq} \end{bmatrix} = \begin{bmatrix} -\frac{r_{sh}}{L_{sh}} & 0 \\ 0 & -\frac{r_{sh}}{L_{sh}} \end{bmatrix} * \begin{bmatrix} i_{shd} \\ i_{shq} \end{bmatrix} + \frac{1}{L_{sh}}\begin{bmatrix} V_{1d} - V_{shd} + \omega L_{sh} i_{shq} \\ -V_{shq} - \omega L_{sh} i_{shd} \end{bmatrix} \tag{3.33}$$

Where, $\dot{x} = \frac{d}{dt}\begin{bmatrix} i_{shd} \\ i_{shq} \end{bmatrix}$, $x = \begin{bmatrix} i_{shd} \\ i_{shq} \end{bmatrix}$, $A = \begin{bmatrix} -\frac{r_{sh}}{L_{sh}} & 0 \\ 0 & -\frac{r_{sh}}{L_{sh}} \end{bmatrix}$, $B = \begin{bmatrix} 1 & 0 \\ 0 & 1 \end{bmatrix}$, $Y = \begin{bmatrix} Y1 \\ Y2 \end{bmatrix}$

$C = \begin{bmatrix} 1 & 0 \\ 0 & 1 \end{bmatrix}$ and $u = \begin{bmatrix} u1 \\ u2 \end{bmatrix} = \frac{1}{L_{sh}}\begin{bmatrix} V_{1d} - V_{shd} + \omega L_{sh} i_{shq} \\ -V_{shq} - \omega L_{sh} i_{shd} \end{bmatrix}$

Equation (3.33) can be written as:

$$\frac{d}{dt}\begin{bmatrix} i_{shd} \\ i_{shq} \end{bmatrix} = \begin{bmatrix} -\frac{r_{sh}}{L_{sh}} & 0 \\ 0 & -\frac{r_{sh}}{L_{sh}} \end{bmatrix} * \begin{bmatrix} i_{shd} \\ i_{shq} \end{bmatrix} + \begin{bmatrix} u1 \\ u2 \end{bmatrix} \tag{3.34}$$

Lets assume the following equation to integrate control variables u with PI (Li, Qiang, 2006):

$$\begin{cases} u1 = \frac{1}{L_{sh}}(k_{psh} + \frac{k_{ish}}{s})(i_{shd}{}^{*} - i_{shd}) \\ u2 = \frac{1}{L_{sh}}(k_{psh} + \frac{k_{ish}}{s})(i_{shq}{}^{*} - i_{shq}) \end{cases} \tag{3.35}$$

Now substitute equation (3.35) into (3.32) and equate it with (3.33), and solve for reference to the shunt converter's output $V_{shd}{}^{*}$ and $V_{shq}{}^{*}$ will give:

$$\begin{bmatrix} V_{shd}{}^{*} \\ V_{shq}{}^{*} \end{bmatrix} = \begin{bmatrix} k_{psh} + \frac{k_{ish}}{s} & 0 \\ 0 & k_{psh} + \frac{k_{ish}}{s} \end{bmatrix} * \begin{bmatrix} i_{shd}{}^{*} - i_{shd} \\ i_{shq}{}^{*} - i_{shq} \end{bmatrix} + \begin{bmatrix} V_{1d} + \omega i_{shq} \\ -\omega i_{shd} \end{bmatrix} \tag{3.36}$$

The shunt converter control diagram is then displayed in the figure below by combining equations (3.15), (3.16) from the shunt current reference computation, and (3.36) above:

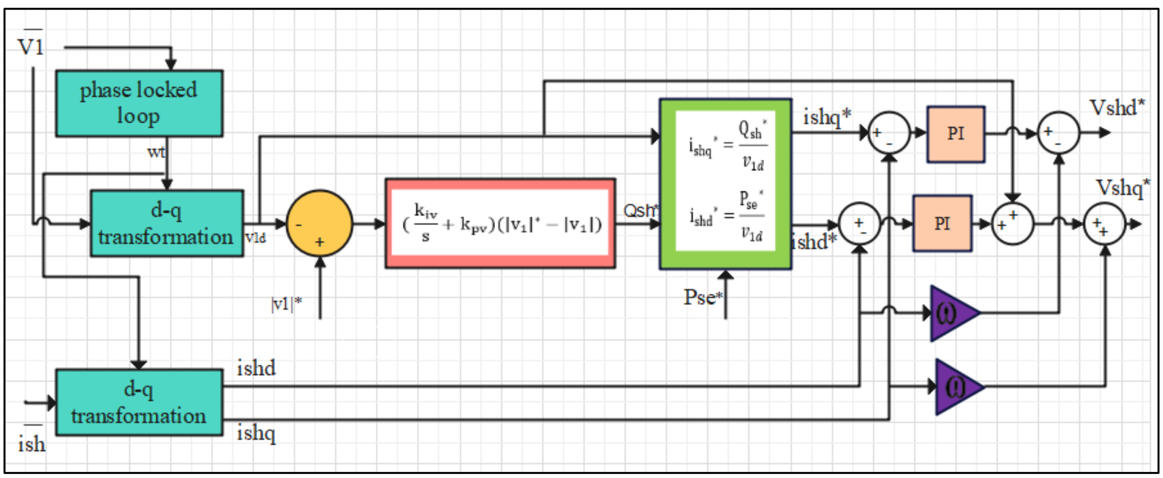

Figure3. 12: D-Q frame shunt converter control by UPFC

3.4.2 Shunt Converter Simulink Model Controller

A MATLAB/SIMULINK model has been created based on the shunt converter controller's mathematical modelling. Below is the shunt controller's full Simulink representation:

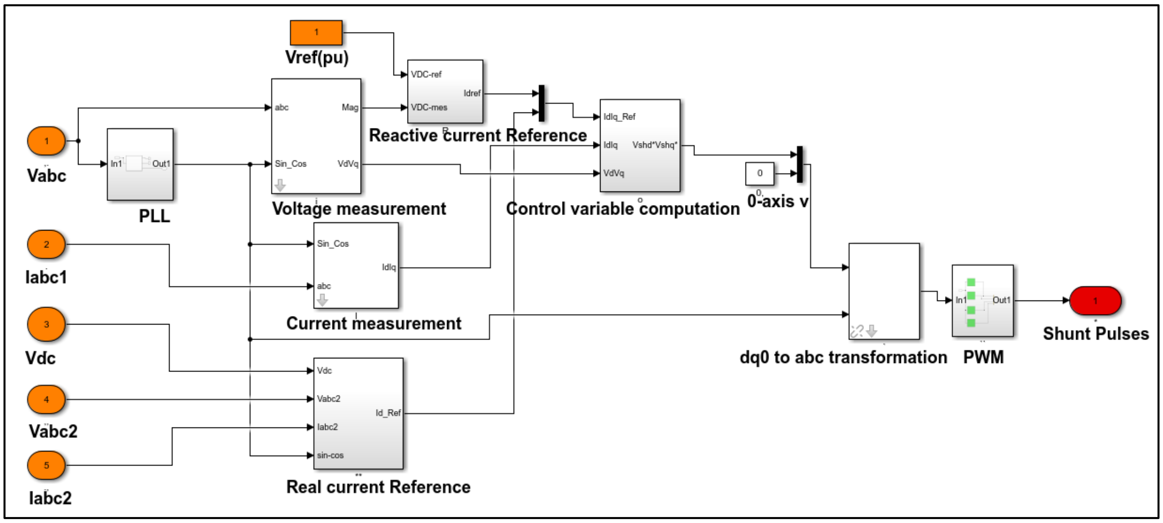

Figure3. 13: SIMULINK representation of the shunt converter controller.

Below is a description of each block in the Simulink model:

- The PLL block model is an example of a Phase-Locked Loop (PLL), a closed-loop control system that uses an internal oscillator to synchronise with the frequency and phase of a sinusoidal input signal. To keep the phase difference between the voltage and current at zero, the system continuously modifies the oscillator's frequency.
- The voltage and current measurement block uses Park's transformation to transform the line voltages and currents into the dq0 reference frame. This transformation's main goal is to make the system's calculations simpler. It also allows the operator to control the current's active (d-axis) and reactive (q-axis) components separately.
- The reactive reference current includes a voltage regulator within the i-qref block, guaranteeing that the voltage level stays stable and uniform under all operating conditions. This system efficiently manages the AC voltage during fluctuations in power and various disturbances. Below is the corresponding Simulink model:

❖ 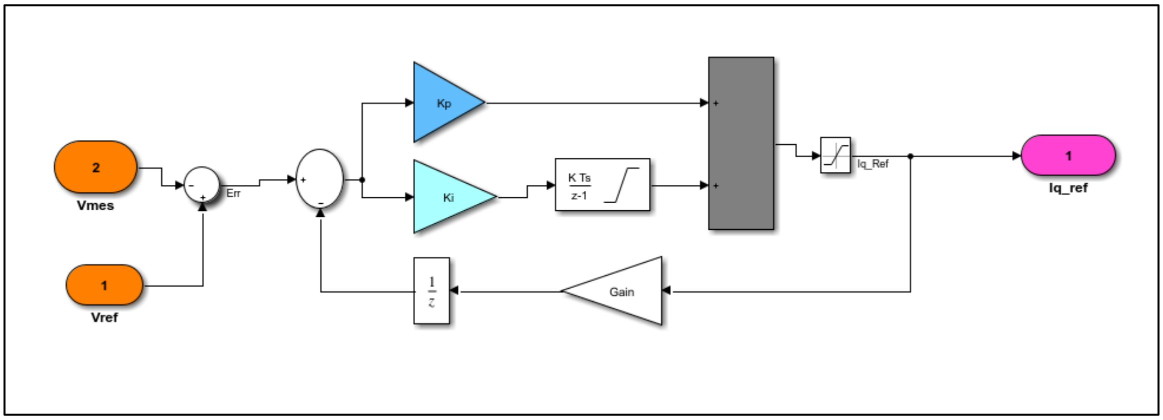

Figure3. 14: AC voltage regulator for iq-ref based on PI

❖ The required d-axis and q-axis reference voltages are calculated by the control variable computation block.

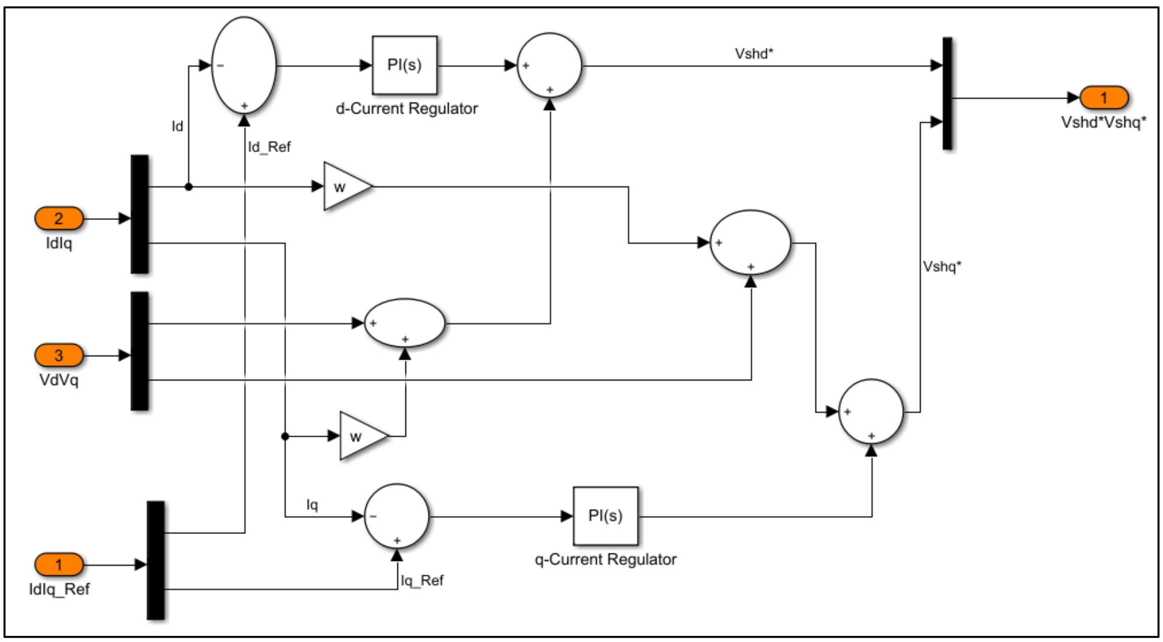

Figure3. 15: Calculation of control variables for vshd* and vshq*

❖ For the id-ref component, the real reference current block has a voltage regulator that helps keep the voltage level steady and constant throughout operation. During power outages and other disruptions, it precisely controls the DC link voltage. The following is the corresponding Simulink model:

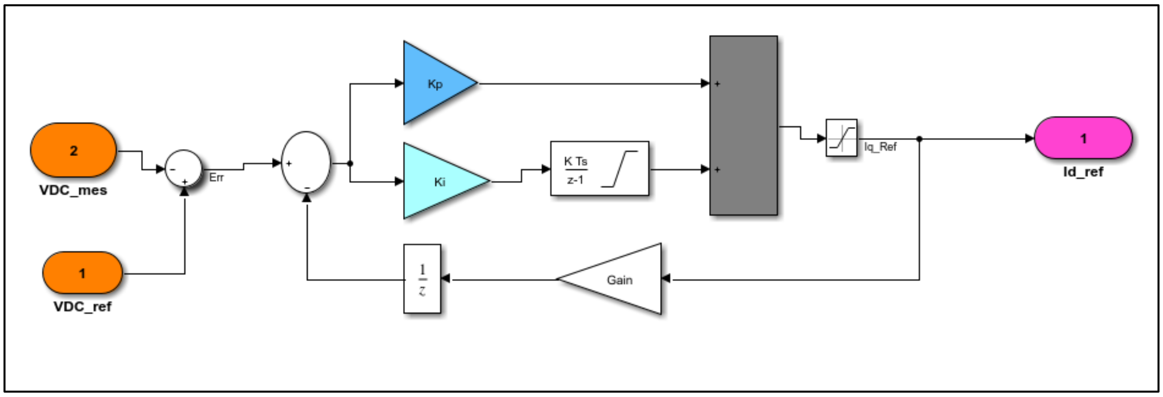

Figure3. 16: DC voltage regulator for id-ref based on PI

❖ The following equations are used by the dq0 to abc transformation block to convert the dq0 to abc:

$$V_a = V_d * \sin wt + V_q * \cos wt + V_0 \tag{3.37}$$

$$V_b = V_d * \sin\left(wt - \frac{2\pi}{3}\right) + V_q * \cos\left(wt - \frac{2\pi}{3}\right) + V_0 \tag{3.38}$$

$$V_c = V_d * \sin\left(wt + \frac{2\pi}{3}\right) + V_q * \cos(wt + \frac{2\pi}{3}) + V_0 \tag{3.39}$$

❖ The discrete PWM generator block produces the PWM signal that regulates the output voltage by controlling the power converter's switching condition.

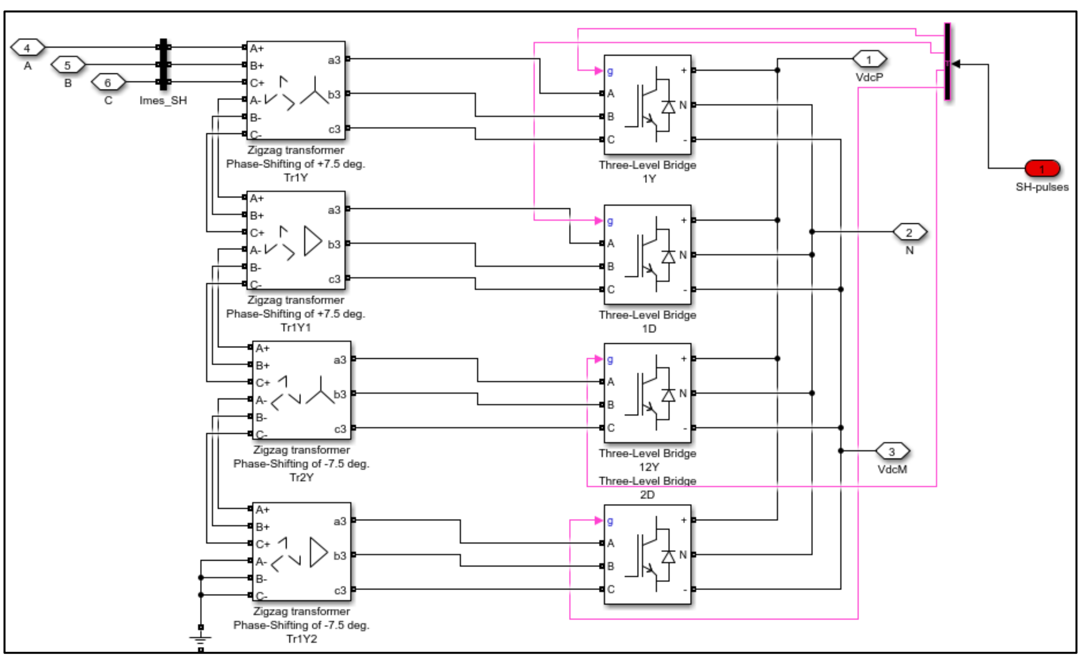

Figure3. 17: Shunt converter for voltage sources (switches)

- The shunt voltage source converter block is the primary component that uses a shared DC link capacitor to convert voltage between AC and DC. It includes four identical zigzag transformers and four identical three-level bridge GTOs that switch system parameters on or off based on predefined input signals. Zigzag transformers are chosen for their iron core design, which effectively reduces harmonic fluxes. Additionally, they are more compact and cost-effective than Transformers with Wye-delta for the same zero-sequence impedance. The operation of the three-level bridge GTOs is governed by control pulses generated by the shunt controller.

3.4.3 Controller Design of Series Converter

In the process of converting the series controller to a state space equation, the rotating axis is synchronized with the receiving end voltage (Vr). Thus, we have (V_{rd} = |V_r|) and (V_{rq} = 0). Equation (3.20) can be rearranged into the following format:

$$\frac{d}{dt}\begin{bmatrix} i_{sed} \\ i_{seq} \end{bmatrix} = \begin{bmatrix} -\frac{R_{se}}{L_{se}} & 0 \\ 0 & -\frac{R_{se}}{L_{se}} \end{bmatrix} * \begin{bmatrix} i_{sed} \\ i_{seq} \end{bmatrix} + \frac{1}{L_{se}} \begin{bmatrix} V_{1d} + V_{sed} - V_{rd} + \omega \mathrm{L_{se}} \mathrm{i_{seq}} \\ V_{1q} + V_{seq} - \omega \mathrm{L_{se}} \mathrm{i_{sed}} \end{bmatrix} \tag{3.40}$$

Where, $\dot{x} = \frac{\mathrm{d}}{\mathrm{dt}}\begin{bmatrix} \mathrm{i_{sed}} \\ \mathrm{i_{seq}} \end{bmatrix}$, $x = \begin{bmatrix} i_{sed} \\ i_{seq} \end{bmatrix}$, $\mathrm{A} = \begin{bmatrix} -\frac{\mathrm{R_{se}}}{\mathrm{L_{se}}} & 0 \\ 0 & -\frac{\mathrm{R_{se}}}{\mathrm{L_{se}}} \end{bmatrix}$, $\mathrm{B} = \begin{bmatrix} 1 & 0 \\ 0 & 1 \end{bmatrix}$,$\mathrm{Y} = \begin{bmatrix} \mathrm{Y1} \\ \mathrm{Y2} \end{bmatrix}$

$\mathrm{C} = \begin{bmatrix} 1 & 0 \\ 0 & 1 \end{bmatrix}$, and $\mathrm{u} = \begin{bmatrix} u1 \\ u2 \end{bmatrix} = \frac{1}{\mathrm{L_{se}}} \begin{bmatrix} V_{1d} + V_{sed} - V_{rd} + \omega \mathrm{L_{se}} \mathrm{i_{seq}} \\ V_{1q} + V_{seq} - \omega \mathrm{L_{se}} \mathrm{i_{sed}} \end{bmatrix}$

Equation (3.40) can be written as:

$$\frac{\mathrm{d}}{\mathrm{dt}}\begin{bmatrix} \mathrm{i_{sed}} \\ \mathrm{i_{seq}} \end{bmatrix} = \begin{bmatrix} -\frac{\mathrm{R_{se}}}{\mathrm{L_{se}}} & 0 \\ 0 & -\frac{\mathrm{R_{se}}}{\mathrm{L_{se}}} \end{bmatrix} * \begin{bmatrix} \mathrm{i_{sed}} \\ \mathrm{i_{seq}} \end{bmatrix} + \begin{bmatrix} \mathrm{u_1} \\ \mathrm{u_2} \end{bmatrix} \tag{3.41}$$

Let us assume the following equation to integrate control variables u with PI:

$$\begin{cases} u1 = \frac{1}{L_{sh}}(k_{psh} + \frac{k_{ish}}{s})(i_{shd}{}^{*} - i_{shd}) \\ u2 = \frac{1}{L_{sh}}(k_{psh} + \frac{k_{ish}}{s})(i_{shq}{}^{*} - i_{shq}) \end{cases} \tag{3.42}$$

Where, $i_{sed}{}^{*}$ is the series converter's reference current for the d-component and $i_{seq}{}^{*}$ is the series converter's reference current for the q-component. Then, substitute (3.42) into (3.41) and equate it with (3.40) and solve for the reference to the series converter's output $V_{sed}{}^{*}$ and $V_{seq}{}^{*}$ will give:

$$\begin{bmatrix} V_{sed}{}^{*} \\ V_{seq}{}^{*} \end{bmatrix} = \begin{bmatrix} k_{pse} + \frac{k_{ise}}{s} & 0 \\ 0 & k_{pse} + \frac{k_{ise}}{s} \end{bmatrix} * \begin{bmatrix} i_{sed}{}^{*} - i_{sed} \\ i_{seq}{}^{*} - i_{seq} \end{bmatrix} + \begin{bmatrix} V_{rd} - V_{1d} - \omega i_{seq} \\ -V_{1q} + \omega i_{sed} \end{bmatrix} \tag{3.43}$$

The figure below displays the control diagram for the series converter:

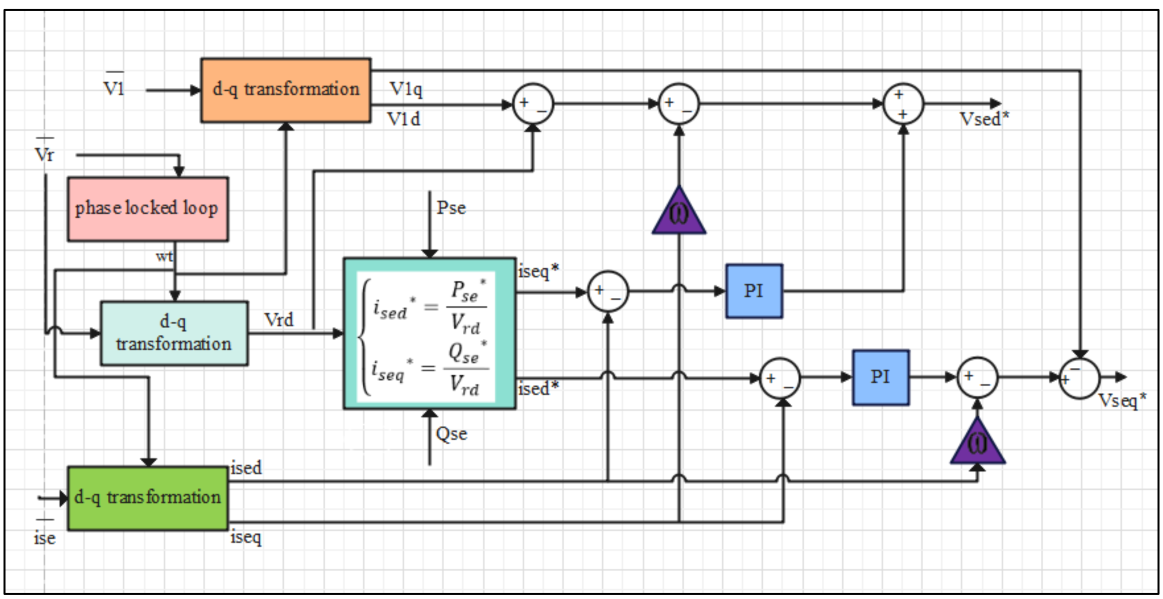

Figure3. 18; D-Q frame control for series converters in UPFC systems.

3.4.4 Simulink Model of Series Converter Controller

A MATLAB/SIMULINK model has been developed as a result of the series converter controller's mathematical modelling. The full Simulink model for the series controller is shown below:

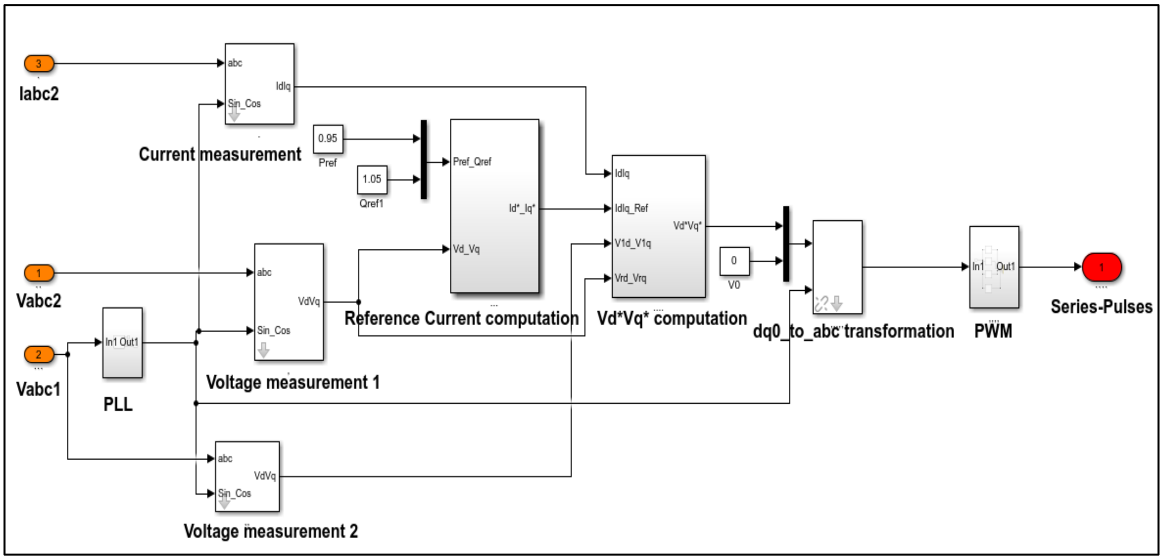

Figure3. 19: Series converter controller models in SIMULINK

Each block in the Simulink model is described below:

- ❖ The PLL block model is a closed-loop control system that uses an internal frequency oscillator to track the frequency and phase of a sinusoidal signal. To maintain a zero phase difference, the control system modifies the internal oscillator frequency.
- ❖ The voltage and current measurement block assesses the line voltage and current, converting them into the d-q-0 frame through Park's transformation. The primary purpose of transforming the three-phase instantaneous voltages and currents into a synchronously rotating reference d-q-o frame is to simplify calculations. Additionally, this transformation enables the system operator to control the active (d-axis) and reactive (q-axis) components of the currents independently.
- ❖ Reference computation block computes the instantaneous reactive and active reference current as follows:

$$i_d^* = \frac{P * V_d + Q * V_q}{V_d^2 + V_q^2} \qquad (3.44)$$

$$i_q^* = \frac{P * V_q - Q * V_d}{V_d^2 + V_q^2} \quad (3.45)$$

The Figure below displays the Simulink model of the reference computation block derived from equations (3.44) and (3.45)..

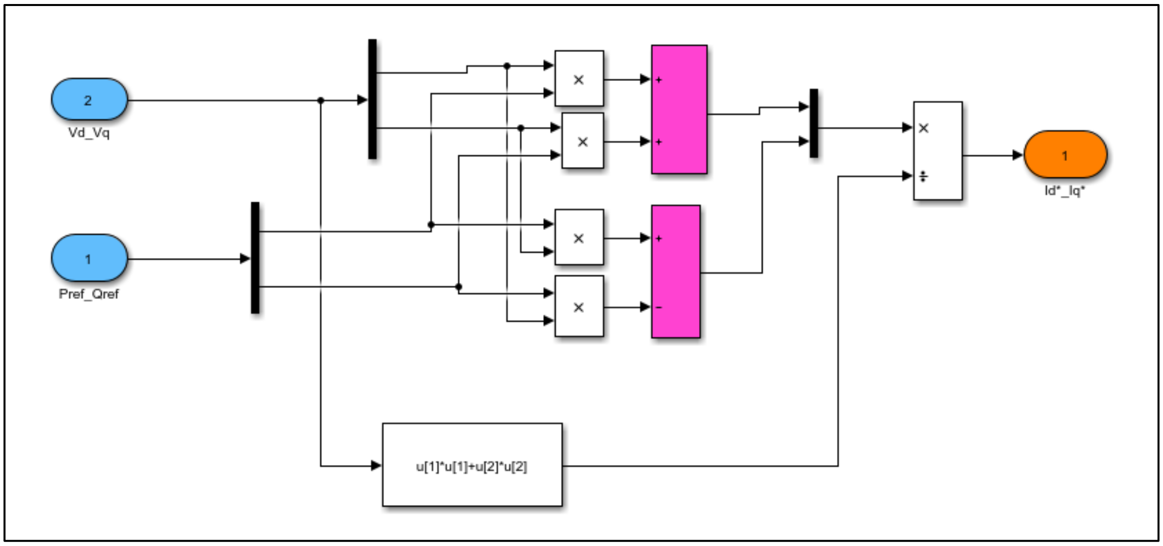

Figure3. 20: d-axis and q-axis reference current calculation of the UPFC series controller in a Simulink model

❖ The control variable computation block calculates reference d-axis and q-axis voltages within a Simulink model, using reference currents, measured currents, and the source voltage as inputs.

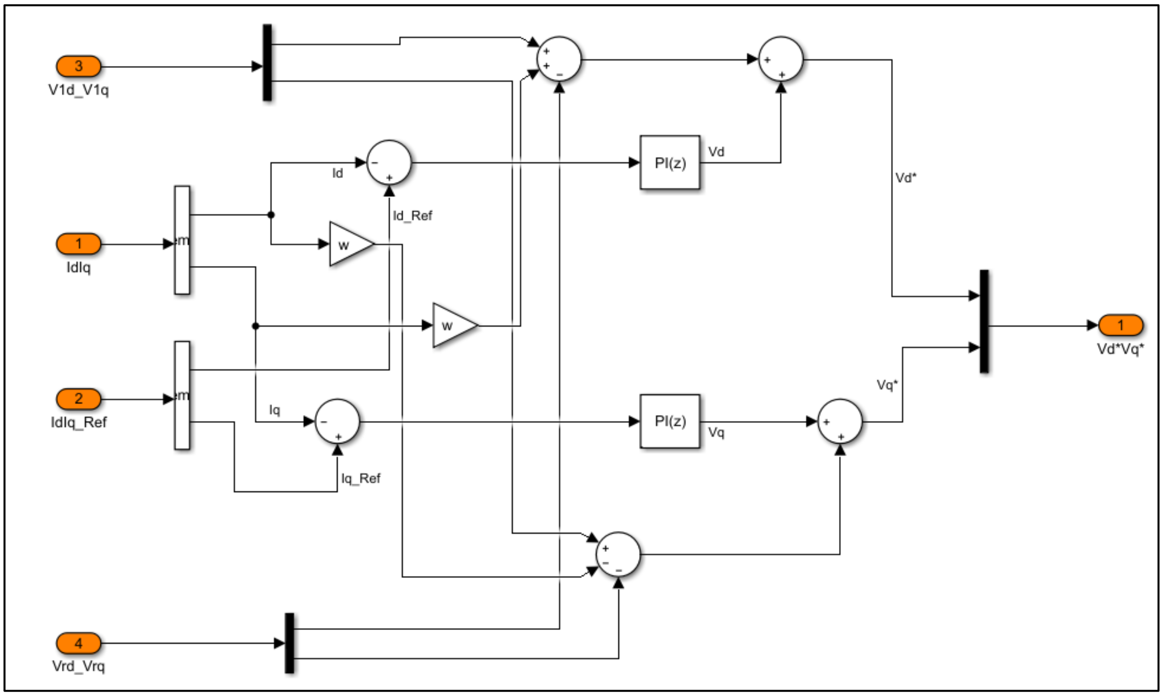

Figure3. 21: Reference voltages for the D-axis and Q-axis of a series converter.

❖ From dq0 to abc, the following is how the transformation block changes the dq0 to abc:

$$V_a = V_d * \sin wt + V_q * \cos wt + V_0 \tag{3.46}$$

$$V_b = V_d * \sin\left(wt - \frac{2\pi}{3}\right) + V_q * \cos\left(wt - \frac{2\pi}{3}\right) + V_0 \tag{3.47}$$

$$V_c = V_d * \sin\left(wt + \frac{2\pi}{3}\right) + V_q * \cos(wt + \frac{2\pi}{3}) + V_0 \tag{3.48}$$

❖ The Discrete PWM generator block produces the PWM signal that manages the switching state of the power converter, allowing for regulation of the output voltage.

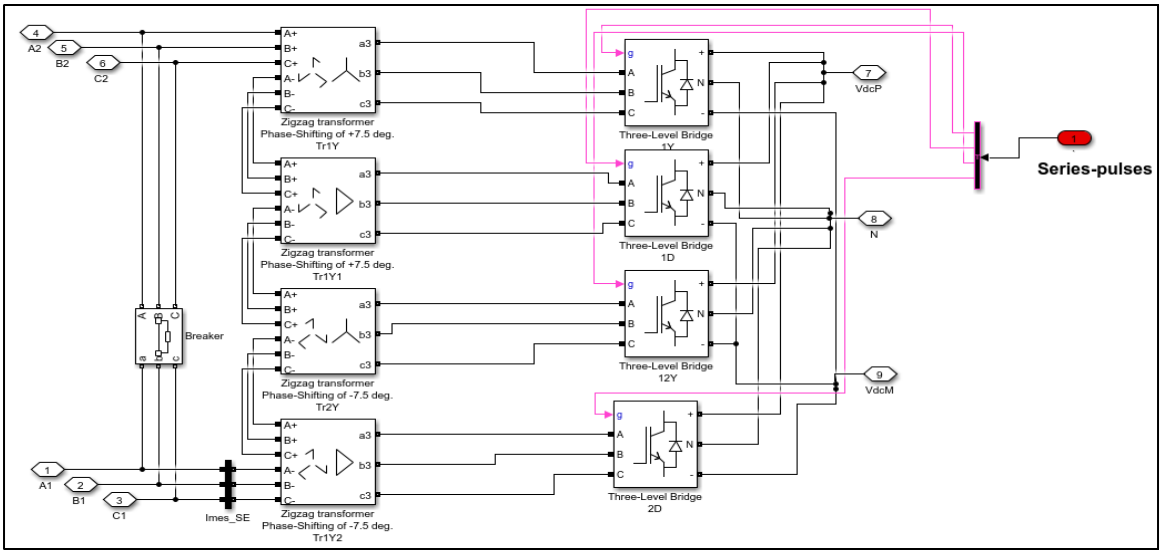

Figure3. 22: Series voltage source converter (switches)

❖ The The series voltage source converter uses zigzag transformers and three-level bridge GTOs to convert AC and DC voltage. Zigzag transformers are preferred for their harmonic flux limitation, smaller size, and cost-effectiveness. The GTOs act as switches controlled by pulse signals to regulate the system.

CHAPTER FOUR

The Optimal Location and Design of an Adaptive Neuro-Fuzzy-Based Unified Power Flow Controller

4.1 Optimal Location of Unified Power Flow Controller Using Modified PSO Integrated With Newton-Raphson Algorithm

4.1.1 Power Flow Study using Newton-Raphson Algorithm

Power systems planning and operation heavily rely on power flow analysis. It gives the voltage level and angle at every network bus. Real and reactive power flows through each transmission line can be computed once these bus voltages are established, enabling the evaluation of system losses. This kind of study, also known as a load flow study, is an example of a steady-state analysis. Because system loads are defined in terms of power, the resulting mathematical equations are non-linear and must be solved using iterative techniques (Kothari, 2011). The Newton-Raphson technique is an iterative method employed to find solutions for systems of nonlinear equations, provided the quantity of equations corresponds to the number of unknown variables. In power system analysis, it offers a more robust and mathematically advanced alternative to the Gauss-Seidel method. It converges faster and is generally more reliable, especially when dealing with ill-conditioned or complex power system networks, making it a preferred choice for load flow studies (Das & Debapriya, 2006).

4.1.2 Power Flow Problem

A typical i[th] bus of a power system is depicted in the figure below. By applying KCL to this bus, the relationship between voltage and current is determined.

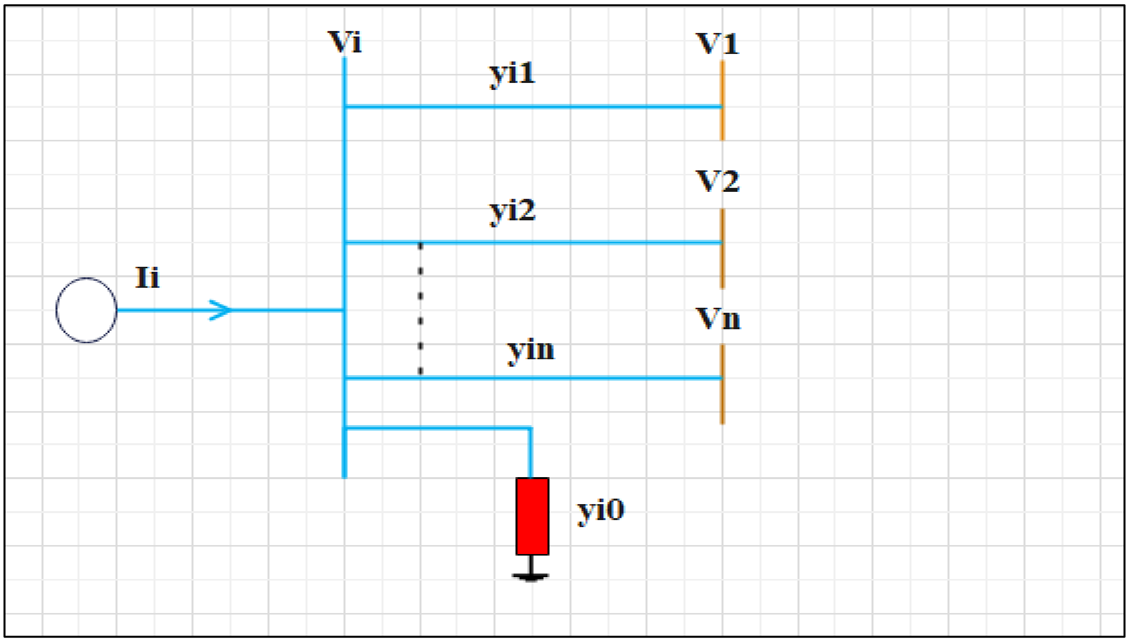

Figure4. 1:An example of a standard power system bus

The net current that flows into the network at the i[th] bus is:

$$I_i = Y_{i1}V_1 + Y_{i2}V_2 + \cdots + Y_{iN}V_N = \sum_{n=1}^{N} Y_{in}V_n \quad (4.1)$$

Where N is the network's total bus count. Let P_i and Q_i represent the net real and reactive power that enter the network at the i[th] bus, respectively..

$$P_i + jQ_i = V_i I_i^{*} \quad (4.2)$$

Equation (4.1) can be substituted into equation (4.2) to yield (4.3):

$$P_i - jQ_i = V_i^{*} \sum_{n=1}^{N} Y_{in}V_n \quad (4.3)$$

Comparing the real and imaginary components:

$$P_i = \sum_{n=1}^{N} |Y_{in}||V_i||V_n| \cos{(\theta_{in} + \delta_n - \delta_i)} \tag{4.4}$$

$$Q_i = -\sum_{n=1}^{N} |Y_{in}||V_i||V_n| \sin{(\theta_{in} + \delta_n - \delta_i)} \tag{4.5}$$

Equations (4.4) and (4.5) form a set of nonlinear algebraic equations in terms of independent variables. Expanding equations (4.4) and (4.5) in Taylor's series, results in set of linear equations as given below.

$$\begin{bmatrix} \Delta P_2{}^{(k)} \\ \vdots \\ \Delta P_n{}^{(k)} \\ \Delta Q_2{}^{(k)} \\ \vdots \\ \Delta Q_n{}^{(k)} \end{bmatrix} = \begin{bmatrix} \frac{\partial P_2{}^{(k)}}{\partial \delta_2{}^{(k)}} & \cdots & \frac{\partial P_2{}^{(k)}}{\partial \delta_n{}^{(k)}} & \frac{\partial P_2{}^{(k)}}{\partial |V_2|^{(k)}} & \cdots & \frac{\partial P_2{}^{(k)}}{\partial |V_n|^{(k)}} \\ \vdots & \ddots & \vdots & \vdots & \ddots & \vdots \\ \frac{\partial P_n{}^{(k)}}{\partial \delta_2{}^{(k)}} & \cdots & \frac{\partial P_n{}^{(k)}}{\partial \delta_n{}^{(k)}} & \frac{\partial P_2{}^{(k)}}{\partial |V_2|^{(k)}} & \cdots & \frac{\partial P_n{}^{(k)}}{\partial |V_n|^{(k)}} \\ \frac{\partial Q_2{}^{(k)}}{\partial \delta_2{}^{(k)}} & \cdots & \frac{\partial Q_2{}^{(k)}}{\partial \delta_n{}^{(k)}} & \frac{\partial Q_2{}^{(k)}}{\partial |V_2|^{(k)}} & \cdots & \frac{\partial Q_2{}^{(k)}}{\partial |V_n|^{(k)}} \\ \vdots & \ddots & \vdots & \vdots & \ddots & \vdots \\ \frac{\partial Q_n{}^{(k)}}{\partial \delta_2{}^{(k)}} & \cdots & \frac{\partial Q_n{}^{(k)}}{\partial \delta_n{}^{(k)}} & \frac{\partial Q_n{}^{(k)}}{\partial |V_2|^{(k)}} & \cdots & \frac{\partial Q_n{}^{(k)}}{\partial |V_n|^{(k)}} \end{bmatrix} \begin{bmatrix} \Delta \delta_2 \\ \vdots \\ \Delta \delta_n \\ \Delta |V_2|^k \\ \vdots \\ \Delta |V_n|^k \end{bmatrix} \tag{4.6}$$

The linearised relationship between minor variations in the voltage angle $\Delta \delta_i{}^{(k)}$ and $\Delta |V_i{}^k|$ is provided by the Jacobian matrix, and voltage level with the slight variations in real $\Delta P_i{}^{(k)}$ and reactive power $\Delta Q_i{}^{(k)}$. Equation 4.6 can be written in short form as:

$$\begin{bmatrix} \Delta P \\ \Delta Q \end{bmatrix} = \begin{bmatrix} J1 & J2 \\ J3 & J4 \end{bmatrix} \begin{bmatrix} \Delta \delta \\ \Delta |V| \end{bmatrix} \tag{4.7}$$

The diagonal and the off diagonal elements of J_1 are:

$$\frac{\partial P_i}{\partial \delta_i} = \sum_{j \neq i}^{n} |Y_{ij}||V_i||V_j| \sin{(\theta_{ij} - \delta_i + \delta_j)} \tag{4.8}$$

$$\frac{\partial P_i}{\partial \delta_j} = -|Y_{ij}||V_i||V_j| \sin{(\theta_{ij} - \delta_i + \delta_j)} \quad j \neq i \tag{4.9}$$

The diagonal and the off-diagonal elements of J_2 are:

$$\frac{\partial P_i}{\partial |V_i|} = 2|Y_{ii}|\,|V_i| cos(\theta_{ii}) + \sum_{j \neq i}^{n} |Y_{ij}||V_j| \cos\,(\theta_{ij} - \delta_i + \delta_j) \tag{4.10}$$

$$\frac{\partial P_i}{\partial |V_j|} = |Y_{ii}|\,|V_i| cos(\theta_{ij} - \delta_i + \delta_j) \quad j \neq i \tag{4.11}$$

The diagonal and the off-diagonal elements of J_3 are:

$$\frac{\partial Q_i}{\partial \delta_i} = \sum_{j \neq i}^{n} |Y_{ij}||V_i||V_j| \cos(\theta_{ij} - \delta_i + \delta_j) \tag{4.12}$$

$$\frac{\partial Q_i}{\partial \delta_j} = -|Y_{ij}||V_i||V_j| \cos\,(\theta_{ij} - \delta_i + \delta_j) \quad j \neq i \tag{4.13}$$

The diagonal and off-diagonal elements of J_4 are:

$$\frac{\partial Q_i}{\partial |V_i|} = -2|Y_{ii}|\,|V_i| \sin\,(\theta_{ii}) - \sum_{j \neq i}^{n} |Y_{ij}||V_j| \cos\,(\theta_{ij} - \delta_i + \delta_j) \tag{4.14}$$

$$\frac{\partial Q_i}{\partial |V_j|} = -|Y_{ij}|\,|V_i| sin(\theta_{ij} - \delta_i + \delta_j) \quad j \neq i \tag{4.15}$$

$\Delta P_i^{(k)}$and $\Delta Q_i^{(k)}$ the disparity between the planned and computed values is referred to as power residuals, defined as follows:

$$\Delta P_i^{(k)} = P_i^{(sch)} - P_i^{(k)} \tag{4.16}$$

$$\Delta Q_i^{(k)} = Q_i^{(sch)} - Q_i^{(k)} \tag{4.17}$$

The new updated bus voltages and angles are:

$$|V_i^{(k+1)}| = |V_i^{(k)}| + \Delta |V_i^{(k)}| \tag{4.18}$$

$$\delta_i^{(k+1)} = \delta_i^{(k)} + \Delta \delta_i^{(k)} \tag{4.19}$$

The iteration will continue until the magnitude of power residuals $\Delta P_i^{(k)}$ and $\Delta Q_i^{(k)}$are below the required level of precision. Rather than using the Newton-Raphson alone, integrating PSO algorithm with Newton-Raphson provides accurate convergence and reduced computational time. This algorithm is applied to the computational achievement of the load flow solution, based on the power system's power mismatches being minimised. The minimum voltage magnitude observed among the given bus voltage magnitudes is considered the worst case at which a FACTS compensator needs to be placed (Abugri et al., 2015).

4.1.3 Particle Swarm Optimization Modified

Particle Swarm Optimization (PSO), introduced in 1995, is an AI technique inspired by flocking behavior used to find near-optimal solutions for complex numerical problems. It uses a swarm of particles representing potential solutions, with each particle adjusting its position based on its own experience and the experiences of its neighbors, effectively balancing global and local search. PSO is known for its robustness and efficiency in optimization tasks (Abugri et al., 2015).

In PSO, each single solution is viewed as a particle. The position of each particle can be expressed as $X_i = (X_{i1}, X_{i2}, X_{i3,}\ldots\ldots\ldots, X_{im})$. The initial solutions in PSO are randomly selected, and then PSO will continually search for the optimal value by updating the solutions in each iteration. The fitness value of the particle is related to the objective function and the velocity of the particle $V_i = (V_{i1}, V_{i2}, V_{i3,}\ldots\ldots\ldots, V_{im})$ is related to its previous velocity, global best-known position, and local best-known position. The velocity indicates the directions of all the particles in the next iteration (Shen, et al., 2018).

Particle Swarm Optimization (PSO) uses a swarm of particles to find optimal solutions. Each particle remembers its personal best position and the swarm tracks the global best position. A particle's velocity is influenced by its inertia, its personal best, and the global best, balancing individual exploration with swarm collaboration. The algorithm iteratively updates particle positions and velocities, guided by these influences.(Cabezas Soldevilla et al., 2019) .

In PSO search scheme, there are two best positions.

1. Personal best (P^{best}) : The best particle achieved so far by that particle.

2. Global best (G^{best}) : The best value obtained so far by any particle in the neighbourhood of that particle.

$$V^{t+1} = w * V^{t} + c1r1\left(P^{best} - X^{t}\right) + c2r2\left(G^{best} - X^{t}\right) \quad (4.20)$$

$$X^{t+1} = X^{t} + V^{t+1} \quad (4.21)$$

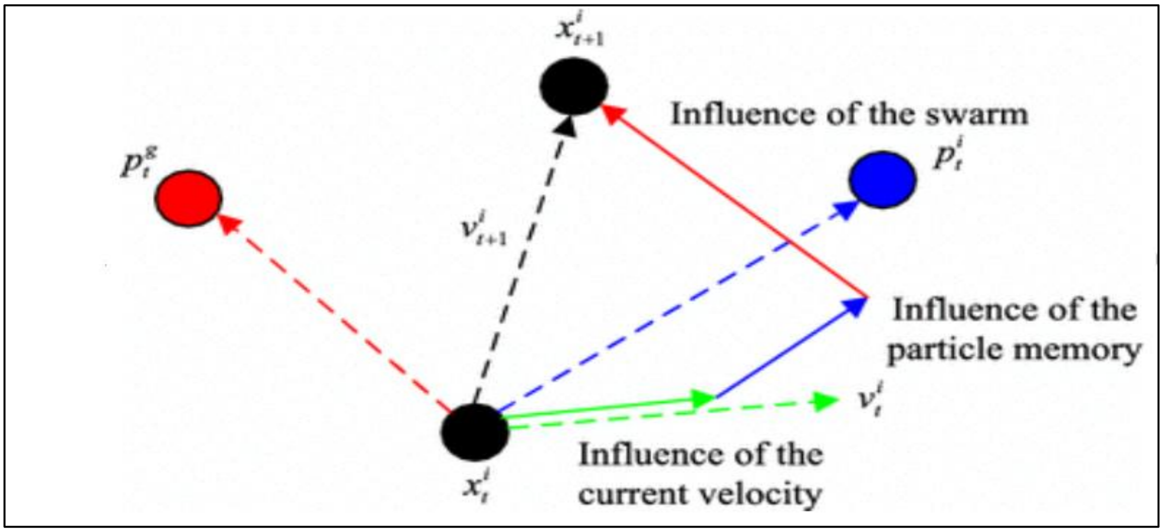

Figure4. 2: PSO iteration scheme of the Particle

Acceleration coefficients in Particle Swarm Optimization (PSO) control how much a particle adjusts its movement based on its own experience and the swarm's best position. Choosing appropriate values is crucial; too small and particles move too slowly, too large and they overshoot, both hindering convergence and potentially trapping the swarm in local minima.

4.1.4 Formulating the Particle Swarm Optimisation Problem

I. Objective Function

The goal is to minimize power transmission losses by adjusting control variables within set limits. This is achieved using Particle Swarm Optimization (PSO) integrated with the Newton-Raphson method to find the optimal placement of a Unified Power Flow Controller (UPFC). PSO is used due to its effectiveness in solving complex, non-smooth optimization problems.

Objective function = Min F(P_{loss})

The sum of the real power losses on each branch determines the system's real power loss, which can be explained as (Abugri et al., 2015):

$$F: P_{loss} = \sum_{i\in j}^{N} Gij \left(V^2{}_i + V^2{}_j - 2V_iV_j cos\theta_{ij}\right) \tag{4.22}$$

Where: N-Number of branches in the network.

Gij-Conductance of the branch connecting bus i and bus j.

Vi & Vj-Voltage magnitudes at bus i and bus j, respectively.

Ɵij-Phase angle difference between bus i and bus j.

Equality Constraints

The equality constraints are the power balance equations, which can be described by the equations as follows.

$$P_{gi} - P_{di} - V_i \sum_{j=1}^{NP} V_j (Gij\, cos\theta_{ij} + Bijsin\theta_{ij}) = 0 \tag{4.23}$$

$$Q_{gi} - P_{di} - V_i \sum_{j=1}^{NQ} V_j (Gij\, sin\theta_{ij} - Bijcos\theta_{ij}) = 0 \tag{4.24}$$

Where: P_{gi} is where bus i generates the real power.

P_{di} is the actual power requirement at bus i.

Q_{gi} is the reactive power generation at bus i.

Q_{di} is the reactive power demand at bus i.

II. Inequality Constraints

The bus voltage magnitude is the inequality constraint used.

$$V_i^{min} < V_i < V_i^{max} \tag{4.25}$$

The bus voltage value per unit should be within the specified limit, which is ±5% of the range ($0.95 \leq vi \leq 1.05$).

III. The Penalty Functions

The application of quadratic penalty functions to optimal power flow problems is covered in this text. System security is the main objective, which is accomplished by reducing constraint violations, even if doing so slightly violates some voltage constraints. Because they enable control over the significance of constraints through adjustments to the penalty factor, quadratic penalty functions are favoured because they guarantee minor infractions and a swift increase in penalty as violations worsen (Baharozu et al., 2015). The equations are depicted as follows:

$$\Omega_v = \rho \sum_{i=1}^{N_B} \{\max(0, |V_i| - |V_i^{max}|)\}^2 + \rho \sum_{i=1}^{N_B} \{\max(0, |V_i^{min}| - |V_i|)\}^2 \qquad (4.26)$$

The results are shown in Table 4.1:

I. PSO at peak load
II. PSO at average load
III. PSO at light load

Table4. 1: PSO parameters used for UPFC placement

PSO parameter	Value
Cognitive factor min (C1)	1.5
Cognitive factor max (C1)	2.5
Social factor min (C2)	1.5
Social factor max (C2)	2.5
Inertia weight min (Wmin)	0.4
Inertia weight max (Wmax)	0.9
Maximum number of iterations	50
Population size	100

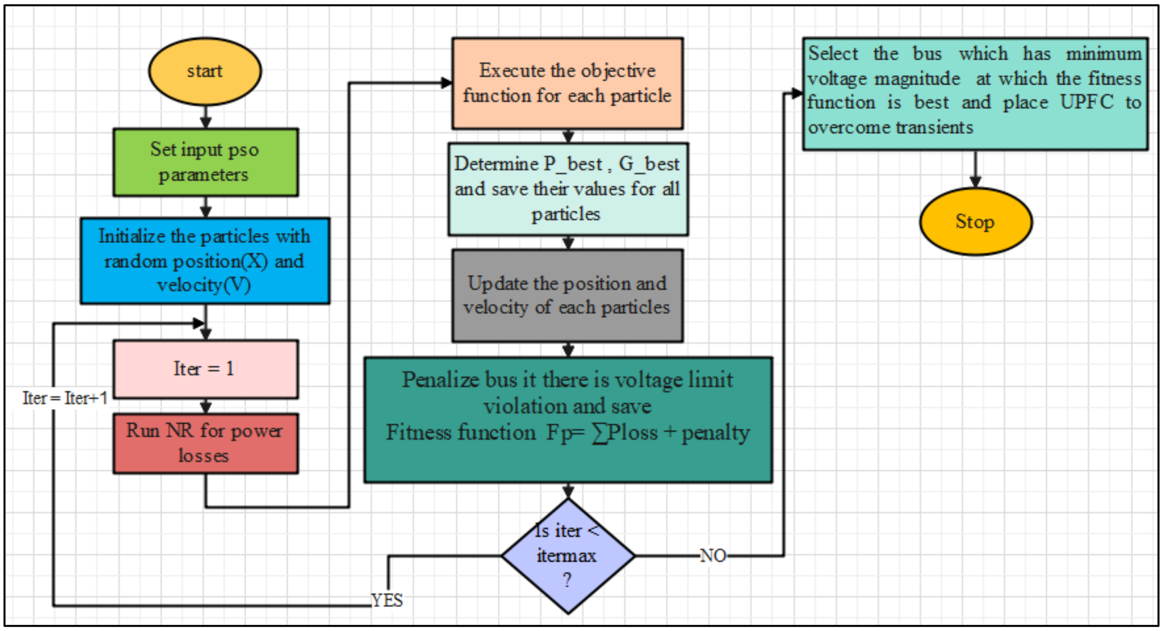

Figure4. 3: UPFC placement flow chart for the modified PSO

Table4. 2: Bus voltage magnitude using modified PSO at three different loading scenarios

Bus No	Bus location	Peak load voltage magnitude (p.u.)	Magnitude of voltage (p.u.) at average load	magnitude of voltage (p.u.) under light load
1	Koka	1.0200	1.0200	1.0200
2	Melka Wakena	1.010	1.010	1.010
3	Adama Wind Farm	1.020	1.020	1.020
3	Hurso	0.9432	0.9456	0.9514
4	Gelan	0.9465	0.9489	0.9549
5	Awash 7 kilo	0.9532	0.9549	0.9563
6	Adama Wind II	0.9532	0.9469	0.9683
7	Nazareth II	0.9432	0.9459	0.9682
8	Awash II	0.9532	0.9579	0.9683
9	Debrezeith II	0.9432	0.9529	0.9533
10	Mojo	0.9270	0.9108	0.9310
11	Kality East industry	0.9448	0.9412	0.9434

The bus with the lowest voltage magnitude at peak load, average load, and light load is determined to be the best place for UPFC placement based on the PSO result. Because the Mojo 132 kV bus bar has magnitudes of 0.9270, 0.9108, and 0.9310 (i.e., the weakest bus is the low voltage magnitude bus with the lowest value for peak load, average load, and light load, respectively. It is the bus that is chosen to place UPFC according to the suggested algorithm.. The convergence characteristics for 100 iterations are as follows:

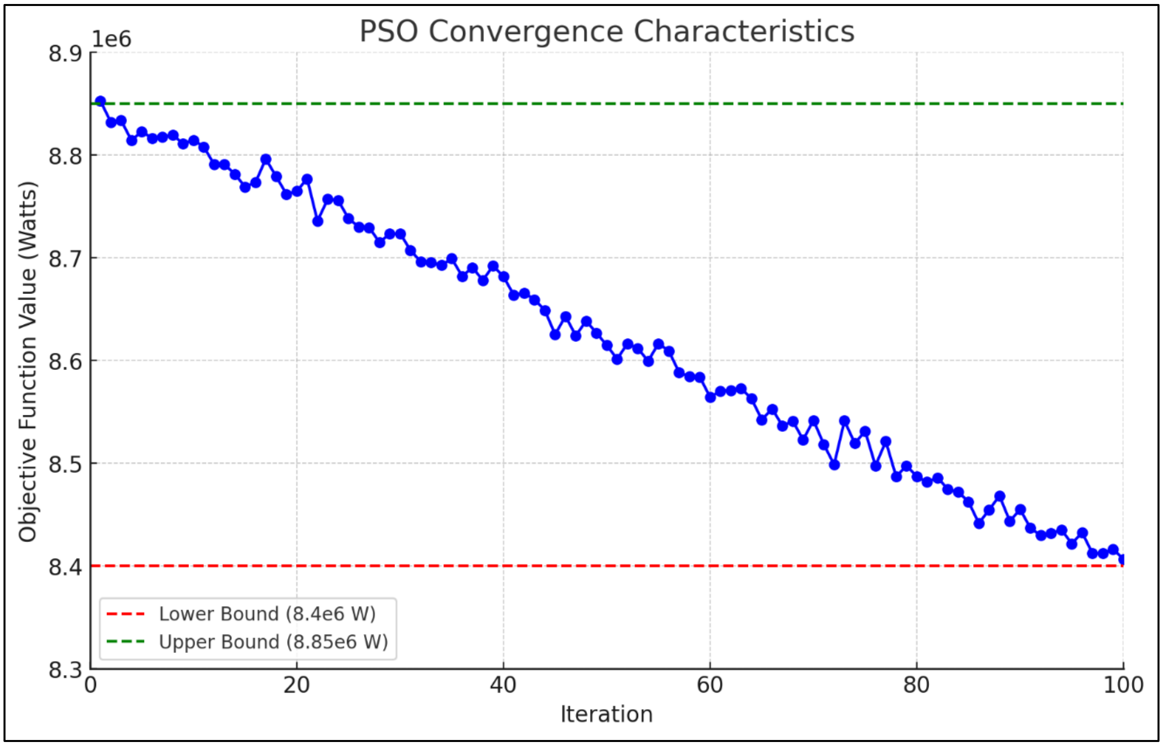

Figure4. 4: Convergence characteristics at peak load for 100 iterations

4.2 UPFC Converter Sizing

The Mojo 132kV substation bus bar is the weakest bus designated for UPFC placement based on the power flow analysis conducted using the Newton-Raphson method. The power network and the UPFC may suffer as a result of sizing mistakes. The ratings for the capacitor, series converter, and shunt converter are all part of the sizing process. The primary side transformers of both converters use the line voltage and power at the UPFC connection point as inputs. In both shunt and series converters, the bus bar voltage of 132 kV corresponds to the transformers' primary side voltage (i.e V_{Sh} primary =V_{SE} primary = 132 kV).

The design of a UPFC (Unified Power Flow Controller) that connects to a high-voltage transmission line via a zigzag transformer is described in the text. Zigzag transformers are favoured because of their affordability, capacity to control harmonic fluxes, and small size. The UPFC is positioned between two buses and is made up of two voltage-sourced converters (VSCs) connected by a common DC link. Both VSCs need step-down transformers to function with the high-voltage line; one is connected in shunt and the other in series. The voltage, power, and frequency ratings of the transmission line are used to choose the parts of the UPFC (Hasanovic, Azra, 2000).

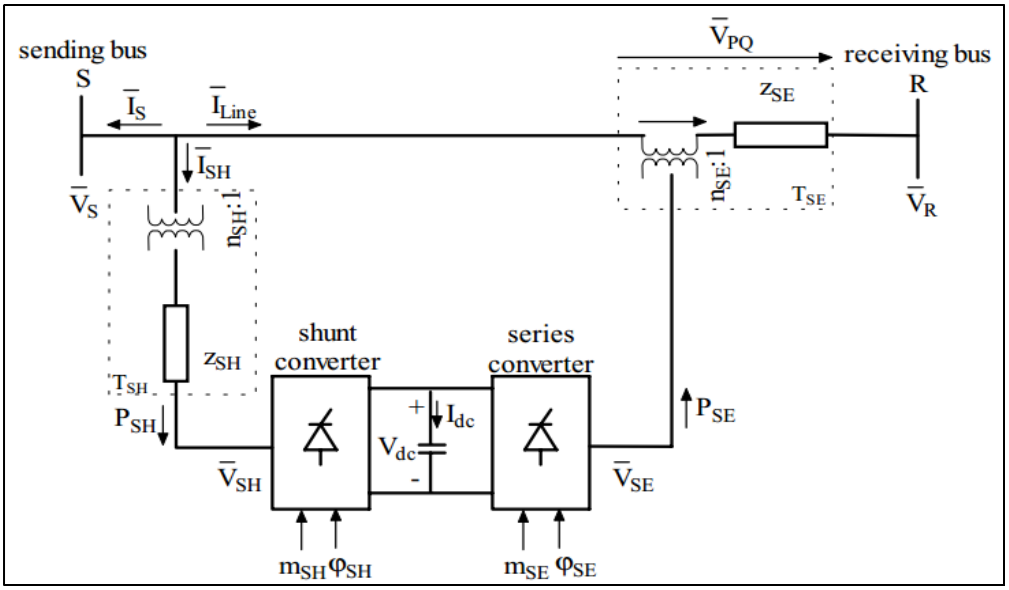

Figure4. 5: UPFC's fundamental frequency model

To calculate the capacitance of a capacitor, the rated KVAR (kilovolt-ampere reactive) of the line must first be determined. Once the rated KVAR is known, the actual KVAR of the capacitor can be computed using the formula below:

$$\text{Actual KVAR} = \text{Rated KVAR} * \frac{\text{Minimum operating frequency of the system}}{\text{Rated frequency of the system}} \qquad (4.27)$$

Rated KVAR of the line where UPFC is connected = 45.69 KVAR (i.e Mojo 132kV)

Rated frequency=50 Hz

Operating frequency recorded = minimum 49 Hz

$$\text{Actual KVAR} = 45.69 * \frac{49}{50} = 44.776\text{KVAR}$$

Then capacitance of the capacitor can be obtained from the actual KVAR using equation (4.28):

$$C = \frac{\text{Actual KVAR} * 10^3}{2\pi V^2} \quad (4.28)$$

$$C = \frac{44.77 * 10^3}{2 * \pi * 400\ \text{kV}^2} = 4.455mF$$

For a given surface areas of electrode (A) to design a capacitor , the corresponding distance between the electrodes (D) can be obtained using the equation (4.29).

$$C = \varepsilon_0 \varepsilon_r \frac{A}{D} \quad (4.29)$$

Where, ε_0: absolute permittivity (8.854 pF/m).

ε_r : relative permittivity of the material (1 for vacuum) .

D : distance of the space between the plates.

A: area of the plate.

The capacitance and supply voltage of a capacitor determine how much energy it can store. The most energy that a DC link can store capacitor is 475 joules with charge time range 1 to 10 seconds (Kandasamy & Rajapalan, 2015).

$$E = \frac{C{V_{DC}}^2}{2} \quad (4.30)$$

Now solving for DC link voltage:

$$V_{DC} = \frac{2E}{C} = \frac{2 * 475}{4.455} = 213.243V(\sim 230V\ \text{Standard})$$

The following formulas can be used to determine the magnitudes of shunt and series injected voltages at the transformer's secondary side when the Pulse Width Modulation (PWM) technique is applied to the two VSCs (Hasanovic& Azra, 2000).

$$V_{SH}\ \text{secondary} = m_{SH} \frac{V_{DC}}{2\sqrt{2}\, n_{SH} V_B} \quad (4.31)$$

$$V_{SE}\ \text{secondary} = m_{SE} \frac{V_{DC}}{2\sqrt{2}\, n_{SE} V_B} \quad (4.32)$$

where: m_{SH} – Amplitude modulation index of the shunt VSC control signal

m_{SE}– Amplitude modulation index of the series VSC control signal

n_{SH} – Shunt transformer turn ratio.

n_{SE} – Series transformer turn ratio

V_B– Base voltage in kV

V_{DC}– DC link voltage

According to IEEE specifications of UPFC details, the shunt VSC and series VSC control signals' amplitude modulation index is in the range of 0.01 to 0.1. Now solving for V_{SH} and V_{SE}:

$$\mathrm{V_{SH}\ secondary} = \mathrm{m_{SH}} \frac{\mathrm{V_{DC}}}{2\sqrt{2}\ \mathrm{n_{SH}V_B}} = 0.9 * \frac{230}{2\sqrt{2} * 0.0037 * 400}$$
$$= 50\ \mathrm{kV}$$

$$V_{SE}\ secondary = m_{SE} \frac{V_{DC}}{2\sqrt{2}\ n_{SE}V_B} = 0.9 * \frac{230}{2\sqrt{2} * 0.0045 * 400}$$
$$= 40\ \mathrm{kV}$$

The values for winding resistance, inductance, and the magnetizing branch resistance and inductance of the UPFC are determined using the corresponding data from the IEEE UPFC catalogue. Based on these selected values, the UPFC is configured with the required block parameters for both the series and shunt transformers, as well as a common DC link capacitor.

Table4. 3: Block parameters of shunt and series transformer

UPFC parameters	**Shunt values**	**Series values**
Nominal power (Sn)	133MVA	133MVA
Nominal frequency (fn)	50Hz	50Hz
Primary nominal voltage (Vp)	132kV	132kV
Secondary nominal voltage (Vs)	50kV	40kV

Primary Winding resistance (R1)	0.0016pu	0.0012pu
Primary Winding inductance (L1)	1pu	0.9pu
Secondary Winding resistance (R2)	0.0016pu	0.0012pu
Secondary Winding inductance (L2)	30pu	25pu
Magnetizing branch resistance (Rm)	1pu	1pu
Magnetizing branch inductance (Lm)	1pu	1pu

4.3 Adaptive Neuro-Fuzzy Inference System Design for Unified Power Flow Controller (ANFIS-based-UPFC)

4.3.1 Background of Neuro Fuzzy Inference System

A hybrid model called a neuro-fuzzy system blends fuzzy logic's ability to handle uncertainty with neural networks' learning capabilities. Proposed by Jang in 1993, it automatically learns fuzzy rules and membership functions from data using training algorithms inspired by neural networks. This adaptive nature allows the system to build an effective fuzzy rule base without manual intervention, making it especially useful for modelling complex, nonlinear systems. The most common implementation, ANFIS (Adaptive Neuro-Fuzzy Inference System), fine-tunes its parameters through learning techniques such as backpropagation or hybrid methods, offering high accuracy and flexibility in applications like control systems, prediction, and optimization (Latha & Rani, 2013). Combining neural networks and fuzzy logic creates powerful controllers, especially for complex systems. Fuzzy logic handles uncertainty well but struggles with rule creation, while neural networks learn and adapt but lack interpretability. Together, they overcome these limitations, creating adaptive systems that dynamically adjust and learn, resulting in more accurate, efficient, and robust control, particularly in real-time applications (Balakrishnan et al., 2013). The Adaptive Neuro-Fuzzy Inference System (ANFIS) successfully tackles the challenges posed by neural networks in terms of transparent decision-making and the insufficient learning capabilities of fuzzy logic controllers by integrating the advantages of both methods.

4.3.2 Significance of Adaptive Neuro-Fuzzy Inference System

The Fuzzy Inference Systems (FIS) use fuzzy logic to map inputs to outputs based on predefined rules, mimicking human decision-making in uncertain environments. They're used in control systems, pattern recognition, and decision-making. Common types include Mamdani (intuitive) and Sugeno (mathematically compact). They are the bases for hybrid models like ANFIS that incorporate learning.

I. Mamdani FIS and
II. Sugeno FIS.

The Mamdani fuzzy inference system, created by Ebrahim Mamdani, was initially designed to control a steam engine and boiler system using a collection of linguistic control rules based on the knowledge of human operators. In this framework, each rule produces an output represented as a fuzzy set, facilitating decision-making through approximate reasoning instead of strict mathematical models.

The second fuzzy inference system was introduced by Takagi, Sugeno, and Kang, aimed at establishing a methodical approach for creating fuzzy rules from a specified input-output dataset. One can express a rule (R_k) as follows:

$$R_k: \text{IF } \mu_{Ai}(x) \text{ AND } \mu_{Bi}(y) \text{ THEN } F = p_k x + q_k y + r_k \tag{4.33}$$

ANFIS (Adaptive Neuro-Fuzzy Inference System) uses fuzzy rules with adjustable membership functions (Ai, Bi) in the antecedent and linear equations (Rk, pk, qk, rk) in the consequent. During training, both the membership function parameters and the linear equation parameters are optimized. ANFIS utilizes the Sugeno Fuzzy Inference System because of its specific characteristics:

- ✓ Only a mathematical combination of the output and the strength of the rules, without any distribution of the output.
- ✓ The system design of Sugeno FIS is more adaptable.
- ✓ Instead of relying on human input, the Sugeno inference system is better suited for mathematical analysis.
- ✓ Work effectively with adaptive and optimisation techniques.
- ✓ Ensure the continuity of the output surface.

4.3.3 Types of Membership Function

Membership functions (MFs) are key to fuzzy logic systems, defining the degree to which an input belongs to a fuzzy set. They transform precise inputs into fuzzy terms and vice-versa, outputting values between 0 and 1 representing membership grade. Introduced by Lotfi Zadeh, MFs come in various shapes (triangular, Gaussian, etc.), and the choice of shape impacts the system's performance and interpretability (Chourasia et al., 2017).

- **Triangular membership function**: The triangular membership function is one of the most commonly used and widely accepted types in fuzzy logic controller design. The triangle that is used to fuzzify the input is shaped by the three parameters a, b, and c. In this arrangement, the triangle's base is determined by a and c, and its peak is represented by the point at which the membership value reaches its maximum (typically 1). This simple structure makes it computationally efficient and easy to implement, making it a popular choice for real-time control applications.

$$\mu_{triangle}(x; a, b, c) = \begin{cases} 0, & x \le a \\ \frac{x-a}{b-a}, & a \le x \le b \\ \frac{c-x}{c-b}, & b \le x \le c \\ 0, & x \le a \end{cases} \tag{4.34}$$

- **Trapezoidal membership function**: It is characterized by four parameters: a, b, c, and d. The interval between b and c represents the range where the membership value reaches its maximum (typically 1). When the input x falls within the ranges (a, b) or (c, d), it is assigned a partial membership value between 0 and 1, depending on its proximity to the peak range.

$$\mu_{trapezoidal}(x; a, b, c, d) = \begin{cases} 0, & x \le a \\ \frac{x-a}{b-a}, & a \le x \le b \\ 1, & b \le x \le c \\ \frac{d-x}{d-c}, & c \le x \le d \\ 0, & d \le x \end{cases} \tag{4.35}$$

- **Gaussian membership function**: It is characterized by two parameters, {m, σ}, and can be described as follows. In this function, m denotes the mean or center of the Gaussian curve, while σ indicates the spread of the curve. Although this approach provides a more natural representation of data distribution, it is rarely used for fuzzification due to its mathematical complexity.

$$\mu_{gaussian}(x; m, \sigma) = e^{-0.5(\frac{x-m}{\sigma})^2} \quad (4.36)$$

❖ **A membership function that is bell-shaped in general**: An alternative name for this is the Cauchy membership function. The three parameters {a, b, c} define a generalised bell membership function, which can be explained as follows. Because we can produce a variety of distinct membership functions by changing the values of a, b, and c, it is known as a generalised membership function.

$$\mu_{bell}(x; a, b, c) = \frac{1}{1 + |\frac{x-c}{a}|^{2b}} \quad (4.37)$$

4.3.4 Architecture of Adaptive Neuro-Fuzzy Inference System

The Adaptive Neuro-Fuzzy Inference System (ANFIS) uses a Sugeno fuzzy model with five layers to map inputs to a single output. It has fixed and adjustable nodes, with the latter found in most layers except the membership function layer.

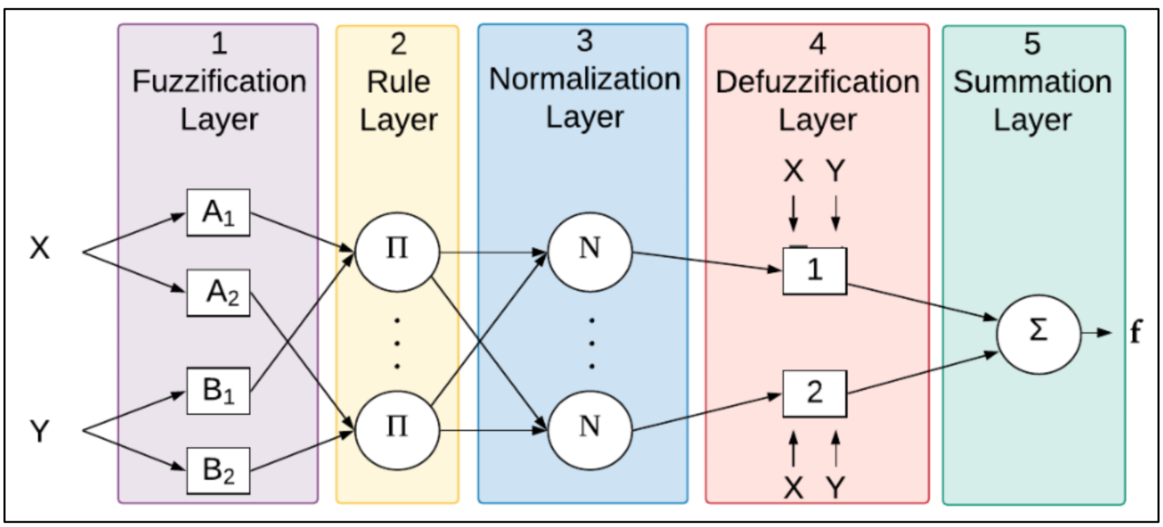

Figure4. 6: Adaptive neurofuzzy inference system architecture

❖ **Layer 1** is the fuzzification layer, in which every neuron functions as an adaptive node and stores the fuzzy value of the crisp inputs. This is how the node output is computed**.**:

$$O_i^{\,1} = \begin{cases} \mu_{Ai}(x) & \forall i = 1,2, \\ \mu_{Bi}(y) & \forall i = 2,3, \end{cases} \quad (4.38)$$

Where μ is a membership function for the fuzzy sets A_i, B_i.

- **Layer 2:** The weight of the premise parameters, or the product of inputs, is stored in the neurones of this implication layer. This is how the node output is computed:

$$O_i^{\,2} = w_i = \mu_{Ai}(x) * \mu_{Bi}(y)\,, \forall i = 1,2, \tag{4.39}$$

Where w_i It is the weight of the neuron.

- **Layer 3:** The neurones in this layer are fixed and normalised by the total weights of all the neurones in the normalising layer. This is how the node output is computed:

$$O_i^{\,3} = \overline{w} = \frac{w_i}{\sum w_i}, \forall i = 1,2 \tag{4.40}$$

Where $\overline{w}$ is the normalized weight of the neuron.

- **Layer 4:** Each neurone in this defuzzification layer serves as an adaptive node and stores the architecture's resulting parameters. The following formula is used to determine the node output: $O_i^{\,4} = \overline{w} f x + q_k y + r_k, \forall i = 1,2$ (4.41)
- **Layer 5:** It is an output layer with a single output neuron that calculates the total output by adding up all of the incoming signals. This is how the node output is computed.:

$$O_i^{\,5} = f(x, y) = \sum \overline{w} f = \frac{\sum w_i f_i}{\sum w_i} \quad \forall i = 1,2 \tag{4.42}$$

ANFIS uses tunable parameters (pk, qk, rk) to learn the mapping between inputs and outputs, minimizing error. It employs a two-pass learning algorithm: Least Squares Estimation (LSE) for parameter adjustment in the forward pass and Gradient Descent (GD) for refining membership functions in the backwards pass.

4.3.5 Design of Neuro-Fuzzy Based Unified Power Flow Controller

Takagi-Sugeno's Adaptive Neuro-Fuzzy Inference System (ANFIS) combines the advantages of fuzzy logic (FL) and artificial neural networks (ANNs) into a unified framework. This system's enhanced learning capacity and adaptable interpretative features allow it to efficiently model complex patterns and understand nonlinear relationships.

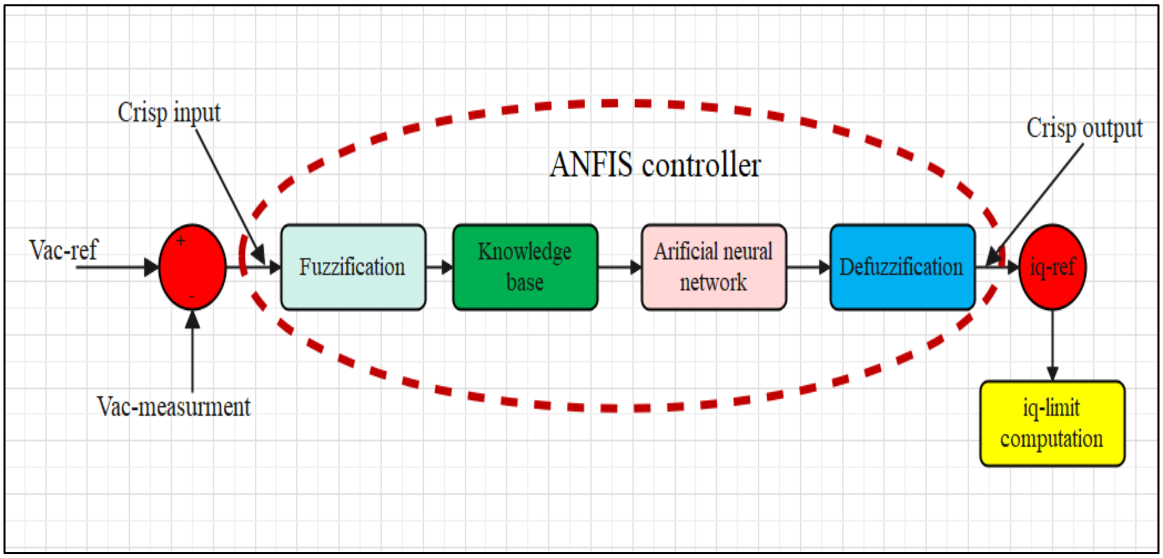

Figure4. 7: Block diagram of adaptive neuro-fuzzy inference system for iq-reference

The AC voltage regulator in a shunt controller uses measured voltage (Vac-mes) and a reference voltage (Vac-ref) to calculate the required q-axis current (Iq). This Iq value is then used by a current regulator to determine the voltage and phase angle needed on the transmission line. A PI controller adjusts the UPFC to inject or absorb current to maintain the voltage at 1 pu. If the measured voltage is below 1 pu, the UPFC injects current; if it's above 1 pu, the UPFC absorbs current; if it's equal to 1 pu, the UPFC does nothing.

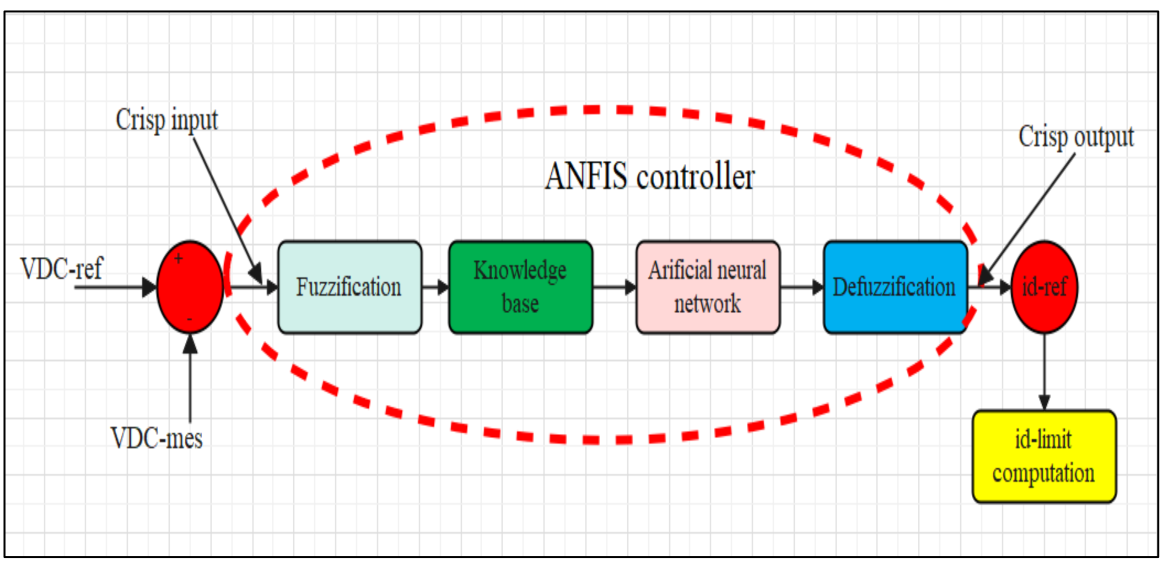

Figure4. 8: Block schematic of an id-reference adaptive neuro-fuzzy inference system

The DC voltage regulator of the shunt controller uses VDC_{mes} and VDC_{ref} as inputs to determine the value of the d-axis current (Id). The d-axis current regulator, which determines the voltage and phase angle needed for a series converter, will receive these d-axis current values as input.

Table4. 4: Characteristics of PID controller

Parameter	Rise time	Overshoot	Settling time	S-S error
Kp increase	Decrease	Increase	Small change	Decrease
Ki increase	Decrease	Increase	Increase	Eliminate
Kd increase	Small change	Decrease	Decrease	Small change

Since ANFIS-based UPFC provides a minimum overshoot and a low settling time when a disturbance is applied to a high-voltage transmission network, PI-based UPFC should be replaced by ANFIS-based UPFC (Liu, et al., 2017).

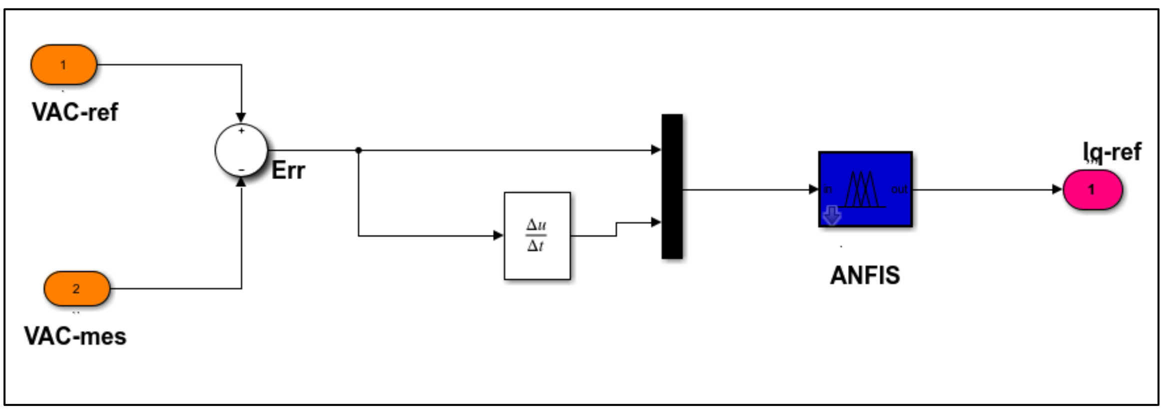

Figure4. 9: iq-reference calculation based on ANFIS

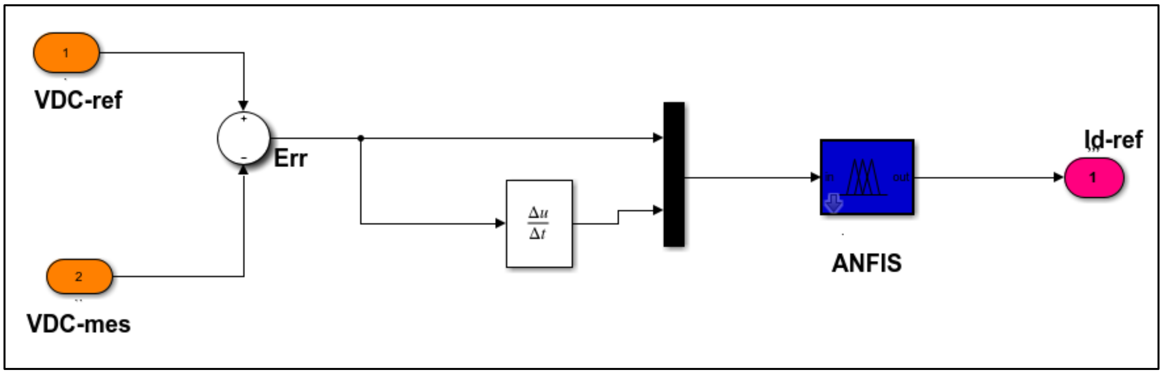

Figure4. 10: id-reference computation using ANFIS

The ANFIS controller uses error and error derivative to determine the quadrature reference current (Iqref) for UPFC. Iqref directly controls line reactance and real power flow. Including error and its derivative as inputs improves the controller's ability to respond to transient disruptions by capturing power system dynamics.

The ANFIS function in the MATLAB toolbox utilizes a specified set of input-output data to build a Takagi-Sugeno fuzzy inference system (FIS), subsequently adjusting the parameters of its membership functions (Sharma & Jagtap, 2010).

4.3.6 Accuracy of ANFIS Training Data

A statistical metric in a regression model called the coefficient of determination (R2) establishes the percentage of variance in the dependent variable that can be accounted for by the independent variable. It is a gauge of a model's goodness of fit and how closely training accuracy matches actual data points. The regression predictions are more than 95% best fit for the data when the R2 value is 0.95.

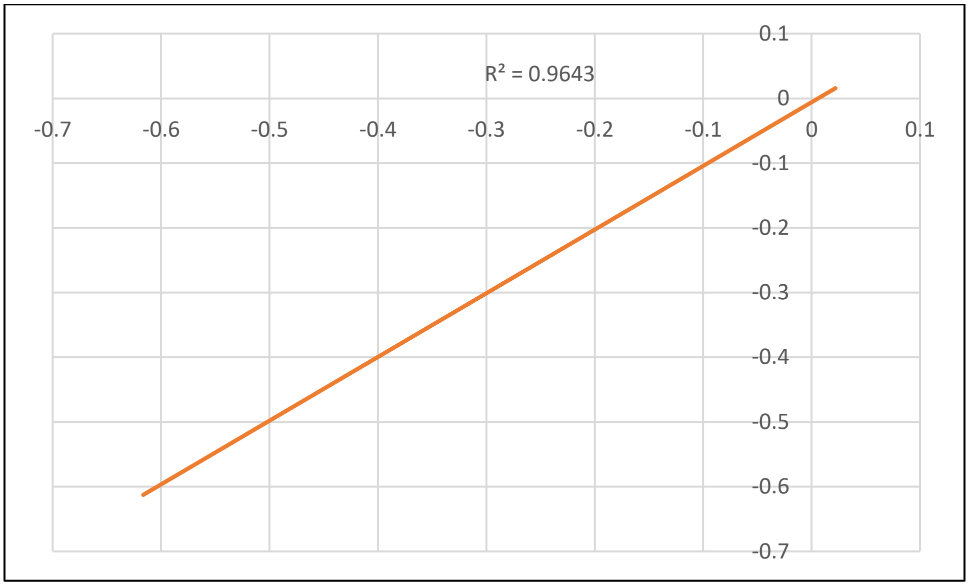

Figure4. 11: ANFIS training data accuracy for the UPFC model

4.3.7 ANFIS Rule Base

The IF-THEN statements that make up the ANFIS rule base represent the process's practical knowledge as understood by human operators. The knowledge that is currently available for designing the UPFC can be used to create a rule that specifies the relationship between the neuro-fuzzy system's input and output. The voltage error and its derivative are the neuro-fuzzy system's inputs. 49 rules are created to depict the input-output relationship, with seven membership functions selected for the voltage error and its derivative.

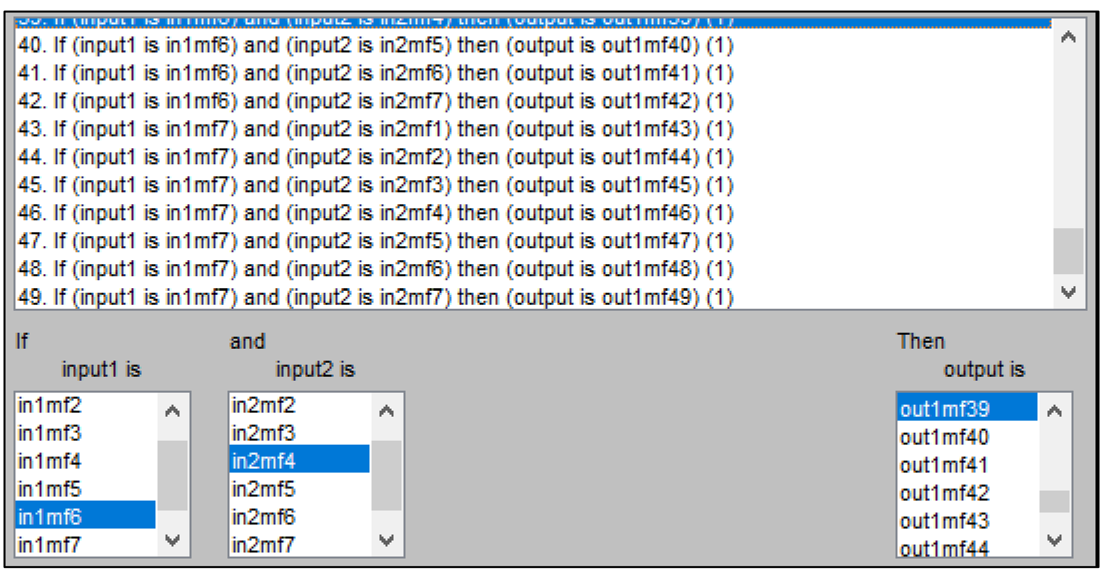

Figure4. 12: Fuzzy inference rules of ANFIS

4.3.8 ANFIS Inference System and its Architecture

ANFIS uses Sugeno fuzzy inference to link inputs to outputs for decision-making. Sugeno inference is computationally efficient because it uses weighted averages or sums instead of centroid calculations for defuzzification and employs singleton output membership functions (constants or linear functions):

- ✓ Computationally efficient;
- ✓ compatible with linear techniques, including PID control;
- ✓ compatible with optimisation and adaptive techniques;
- ✓ able to ensure output surface continuity;
- ✓ and well-suited for mathematical analysis.

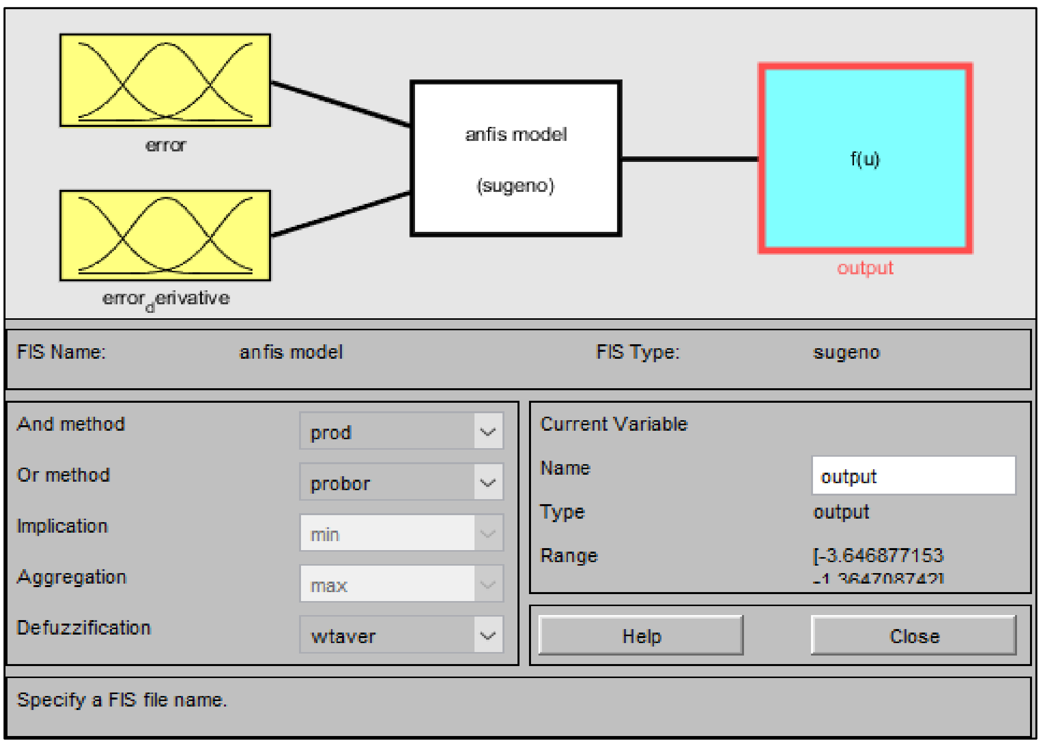

Figure4. 13: Sugeno inference system for ANFIS

The ANFIS structure is composed of five layers: the fuzzification layer, product layer, normalising layer, defuzzification layer, and total output layer. Its MATLAB structure is shown in the figure below. The voltage error and the rate of change of the voltage error are the two inputs to the ANFIS architecture.

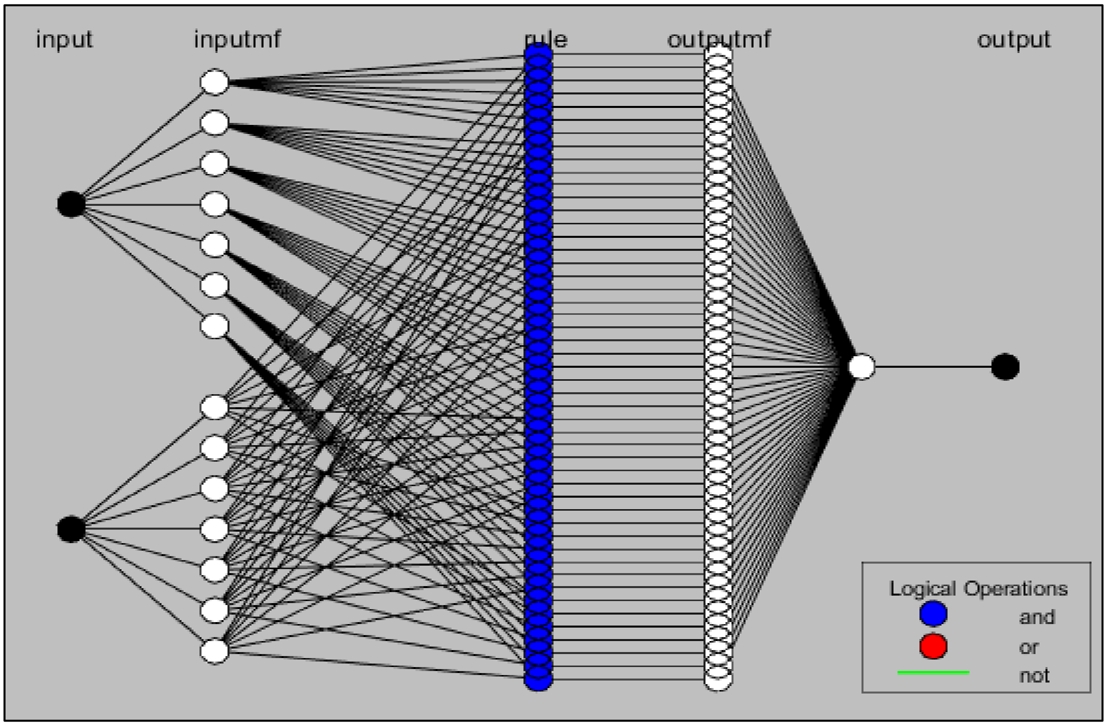

Figure4. 14: Anfis model structure

4.4 Cost Analysis of Unified Power Flow Controller

The UPFC is a highly versatile FACTS device used in high-voltage transmission networks for rapid reactive power compensation and superior power flow control compared to other methods. It combines STATCOM and SSSC functionalities to manage both active and reactive power, enhancing transmission capacity, voltage stability, and system damping.

In order to evaluate the effect of the UPFC on a synchronous generator in a particular power system, the text also discusses a cost comparison study and transient fault analysis.

Table4. 5: Power loss from Koka to Kality East line under various loads

Loading condition	Not using UPFC	Using PI-based UPFC	With ANFIS-based UPFC
At minimum load	9.0	4.5	4.0
At average load	11.0	5.0	3.0
At peak load	15.42	9.6	8.3

Table4. 6: Power loss from Melka wakena to Koka line under various loads

Loading condition	Not using UPFC	Using PI-based UPFC	With ANFIS-based UPFC
At minimum load	8.7	4.0	3.8
At average load	10.6	4.6	2.6
At peak load	14.98	9.4	8.2

Table4. 7: Power loss from Koka to Hurso line under various loads

Loading condition	Not using UPFC	Using PI-based UPFC	With ANFIS-based UPFC
At minimum load	8.5	3.8	3.6
At average load	10.4	4.4	2.5
At peak load	14.70	9.38	8.12

Table4. 8: Power loss from Gelan to Koka line under various loads

Loading condition	Not using UPFC	Using PI-based UPFC	With ANFIS-based UPFC
At minimum load	8.3	3.5	3.5
At average load	10.3	4.3	2.4
At peak load	14.60	9.28	8.98

Table4. 9: Power loss from Koka to Awash 7 kilo line under various loads

Loading condition	Not using UPFC	Using PI-based UPFC	With ANFIS-based UPFC
At minimum load	8.2	3.4	3.48
At average load	10.28	4.21	2.38
At peak load	14.58	9.18	8.96

Table4. 10: Power loss from Adama Wind II to Koka line under various loads

Loading condition	Not using UPFC	Using PI-based UPFC	With ANFIS-based UPFC
At minimum load	8.18	3.36	3.38
At average load	10.18	4.19	2.28
At peak load	13.59	8.68	7.76

Table4. 11: Power loss from Koka to Nazret line under various loads

Loading condition	Not using UPFC	Using PI-based UPFC	With ANFIS-based UPFC
At minimum load	7.20	3.67	3.43
At average load	9.56	4.29	2.11
At peak load	12.49	8.32	6.38

Table4. 12: Power loss from Koka to Awash II line under various loads

Loading condition	Not using UPFC	Using PI-based UPFC	With ANFIS-based UPFC
At minimum load	9.0	4.5	4.0
At average load	11.0	5.0	3.0
At peak load	15.42	9.6	8.3

Table4. 13: Power loss from Koka to Mojo line under various loads

Loading condition	Not using UPFC	Using PI-based UPFC	With ANFIS-based UPFC
At minimum load	8.3	5.66	5.23
At average load	10.46	5.03	4.99
At peak load	16.89	9.56	9.38

4.4.1 Annual Energy Loss (MWh) for Each Line in Three Different Scenarios

The Annual energy of the power loss for all loads in three different scenarios can be evaluated as follows:

I. The Annual energy loss from Koka to Kality East line for the three scenarios evaluated in this study can be estimated as follows:

Case 1: Energy losses of the system without UPFC

Scenario 1: Annual MWh loss at minimum load

Annual MWh loss = (Minimum loss in MW) * 8760 h =9MW*8760 h=78,840 MWh

Scenario 2: Annual MWh loss at an average load

Annual MWh loss = (Average loss in MW) * 8760 h =11 MW*8760 h=96,360MWh

Scenario 3: Annual MWh loss at peak load

Annual MWh loss = (Peak loss in MW) * 8760 h =15.42 MW*8760 h=135,079.20 MWh

Case 2: Energy losses of the system with ANFIS-based UPFC

Scenario 1: Annual MWh loss at minimum load

Annual MWh loss = (Minimum loss in MW) * 8760 h =4 MW*8760 h=35,040MWh

Scenario 2: Annual MWh loss at an average load

Annual MWh loss = (Average loss in MW) * 8760 h =3MW*8760 h= 26,280 MWh

Scenario 3: Annual MWh loss at peak load

Annual MWh loss = (Peak loss in MW) * 8760 h =8.3 MW*8760 h= 72,708 MWh

II. Following the same procedure as above, the annual energy loss from Melka wakena to Koka line for the three scenarios evaluated in this study can be estimated as follows:

Table4. 14: The Annual energy loss from Melka wakena to Koka line without UPFC

Annual energy loss at different loading conditions	Annual energy loss (MWh)
At minimum load	76,212
At an average load	92,856
At peak load	131,224.80

Table4. 15: The Annual energy loss from Melka wakena to Koka line with ANFIS-based-UPFC

Annual energy loss at different loading conditions	Annual energy loss (MWh)
At minimum load	33,288
At an average load	22,776
At peak load	71,832

III. The Annual energy loss from Koka to Hurso line for the three scenarios evaluated in this study can be estimated as follows:

Table4. 16: The Annual energy loss from Koka to Hurso line without UPFC

Annual energy loss at different loading conditions	Annual energy loss (MWh)
At minimum load	74,460
At an average load	91,104
At peak load	128,772

Table4. 17: The Annual energy loss from Koka to Hurso line with ANFIS-based-UPFC

Annual energy loss at different loading conditions	Annual energy loss (MWh)
At minimum load	31,536
At an average load	21,900
At peak load	71,131.20

IV. The annual energy loss from Gelan to Koka line for the three scenarios evaluated in this study can be estimated as follows:

Table4. 18: The Annual energy loss from Gelan to Koka line without UPFC

Annual energy loss at different loading conditions	Annual energy loss (MWh)
At minimum load	72,708
At an average load	90,228
At peak load	127,896

Table4. 19: The Annual energy loss from Gelan to Koka line with ANFIS-based-UPFC

Annual energy loss at different loading conditions	Annual energy loss (MWh)
At minimum load	30,660
At an average load	21,024
At peak load	78,664.80

V. The annual energy loss from Koka to Awash 7Kilo line for the three scenarios evaluated in this study can be estimated as follows:

Table4. 20: The Annual energy loss from Koka to Awash 7Kilo line without UPFC

Annual energy loss at different loading conditions	Annual energy loss (MWh)
At minimum load	71,832
At an average load	90,052.80
At peak load	127,720.80

Table4. 21: The Annual energy loss from Koka to Awash 7Kilo line with ANFIS-based-UPFC

Annual energy loss at different loading conditions	Annual energy loss (MWh)
At minimum load	30,484.80
At an average load	20,848.80
At peak load	78,489.60

VI. The annual energy loss from Adama Wind II to Koka line for the three scenarios evaluated in this study can be estimated as follows:

Table4. 22: The Annual energy loss from Adama Wind II to Koka line without UPFC

Annual energy loss at different loading conditions	Annual energy loss (MWh)
At minimum load	71,656.80
At an average load	89,176.80
At peak load	119,048.40

Table4. 23: The Annual energy loss from Adama Wind II to Koka line with ANFIS-based-UPFC

Annual energy loss at different loading conditions	Annual energy loss (MWh)
At minimum load	29,608.80
At an average load	19,972.80
At peak load	67,977.60

VII. The annual energy loss from Koka to Nazret line for the three scenarios evaluated in this study can be estimated as follows:

Table4. 24: The Annual energy loss from Koka to Nazret line without UPFC

Annual energy loss at different loading conditions	Annual energy loss (MWh)
At minimum load	63,072
At an average load	83,745.60
At peak load	109,412.40

Table4. 25: The Annual energy loss from Koka to Nazret line with ANFIS-based-UPFC

Annual energy loss at different loading conditions	Annual energy loss (MWh)
At minimum load	30,046.80
At an average load	18,483.60
At peak load	55,888.80

VIII. The annual energy loss from Koka to Awash II line for the three scenarios evaluated in this study can be estimated as follows:

Table4. 26: The Annual energy loss from Koka to Awash II line without UPFC

Annual energy loss at different loading conditions	Annual energy loss (MWh)
At minimum load	78,840
At an average load	96,360
At peak load	135,079.20

Table4. 27: The Annual energy loss from Koka to Awash II line ANFIS-based UPFC

Annual energy loss at different loading conditions	Annual energy loss (MWh)
At minimum load	35,040
At an average load	26,280
At peak load	72,708

IX. The annual energy loss from Koka to Mojo line for the three scenarios evaluated in this study can be estimated as follows:

Table4. 28: The Annual energy loss from Koka to Mojo line without UPFC

Annual energy loss at different loading conditions	Annual energy loss (MWh)
At minimum load	72,708
At an average load	91,629.60
At peak load	147,956.40

Table4. 29: The Annual energy loss from Koka to Mojo line with ANFIS-based-UPFC

Annual energy loss at different loading conditions	Annual energy loss (MWh)
At minimum load	45,814.80
At an average load	43,712.40
At peak load	82,168.80

While FACTS controllers offer quick control to enhance electric power systems, a significant disadvantage of power-electronic-based controllers is that they are more expensive per unit of capacity than conventional equipment.

Table4. 30: Typical investment cost for different FACTs controllers (Tsehay, 2019)

FACTs Controller	Cost (US$)
DSTATCOM	34 per KVAR
SVC	26 per KVAR
TCSC	47 per KVAR
UPFC	37 per KVAR

From chapter 3, the UPFC rating calculated is 133MVA. The power factor at peak load at Koka 132kV bus is 0.87. MVAr rating of UPFC at peak load is calculated as (MVAr=MVA*sinϴ=133*0.493046=65.57MVAr).

The total cost is 65.57*1000*37$=2,426,090$. Convert the dollar into Ethiopian birr: 1$=132.65ETB. The total investment cost for UPFC is 2,426,090*132.65ETB **321,820,838.5ETB**. Energy tariff implementation for all consumer class adjusted by Ethiopian Electric Power and Ethiopian Energy Authority is shown in Table 4.13.

Table4. 31: Ethiopia's energy tariff for all consumer levels

Consumer block	Consumption	Energy Tariff (Birr/kWh)
1st Block	Up to 50 KWh	0.2730
2nd Block	Up to 100 KWh	0.7670
3rd Block	Up to 200 KWh	1.6250
4th Block	Up to 300 KWh	2.0000
5th Block	Up to 400 KWh	2.2000
6th Block	Up to 500 KWh	2.4050
7th Block	kWh> 500 KWh	2.4810

Table4. 32: Total energy saved annually for all transmission lines

Loading condition	Total MWh loss annually Without UPFC	Total MWh loss annually With ANFIS-based-UPFC	Total Energy (MWh) saved annually	Total ETB saved annually
At minimum load	660,328.80	336,566.000	626,768.80	83,140,881.32
At average load	821,512.80	221,277.600	600,235.20	79,621,199.28
At peak load	1,271,237.60	651,568.80	619,668.80	82,199,066.32

4.4.2 Payback Period for UPFC Investment Cost

The payback period refers to how many years it will take to recover the original investment made in a UPFC. This approach identifies the time frame within which the original expenditure is recovered. A project proceeds only if the payback period is shorter than a specific threshold set by the company, which commonly ranges from 2 to 6 years.

$$\text{Payback period} = \frac{\text{Initial UPFC investment cost}}{\text{Total ETB saved annualy}} \qquad (4.43)$$

$$\text{Payback period at Peak load} = \frac{321{,}820{,}838.50\text{ETB}}{82{,}199{,}066.32\text{ETB}} = 3.915 \text{ years}$$

CHAPTER FIVE

SIMULATION RESULT AND DISCUSSION

5.1 Introduction

This chapter uses simulation to verify the developed models. Results show how well an ANFIS-based UPFC integrated into the system performs in terms of transient stability. high-voltage transmission network spanning from Adama II and Koka to Kality. The simulation considers various interconnected lines, including Melka Wakena–Koka, Koka–Hurso, Gelan–Koka, Koka–Awash 7 Kilo, Adama Wind II–Koka, Koka–Nazreth, Koka–Awash II, and Koka–Gelan Mojo, incorporating equivalent transmission line impedances, transformer characteristics, and load conditions. The findings confirm that the UPFC significantly enhances the transient stability of the Adama II–Koka–Kality interconnected system under different disturbance scenarios. Additionally, Particle Swarm Optimization (PSO) is employed to identify the system's weakest bus for optimal UPFC placement, revealing that the 132 kV bus bar at Mojo substation is the most effective location for its installation.

The simulation utilizes MATLAB/SIMULINK, capturing various performance metrics to evaluate the effectiveness of the proposed controller. The input and output of the PI-based voltage regulator are used to create ANFIS training and testing datasets in order to validate this controller. The inputs include the voltage error and its derivative, whereas the outputs consist of the direct and quadrature current components. In the ANFIS model, a triangular membership function is employed, which efficiently converts non-fuzzy input values into fuzzy linguistic terms, thereby improving transient stability. In total, 300,000 data samples are gathered from the PI-controlled UPFC system. 30% of the extracted data is set aside for testing, and the remaining 70% is used for training in order to validate the ANFIS model. Key metrics, such as power transfer capability, loss minimisation, and voltage profile enhancement, are then compared to assess the ANFIS-based UPFC's performance..

5.2 Fault types and their percentage of occurrence in the Adama II, Koka to Kality HV Transmission Line

Electrical power systems primarily experience two types of faults: symmetrical faults and unsymmetrical faults.

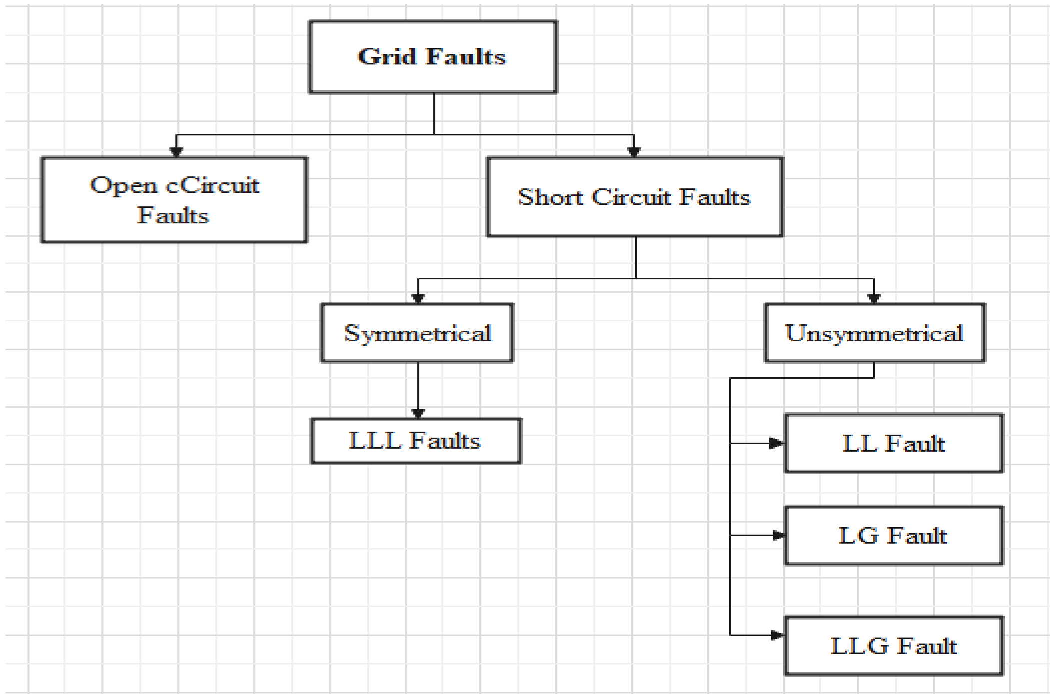

Figure5. 1: Types of power grid faults (Gaurav, 2023).

I. **Symmetrical faults**: These are uncommon but very serious power system faults, also known as balanced faults. Line-to-line-to-ground (L-L-G) and line-to-line-to-line (L-L-L) faults are among them. Such faults can seriously harm both electrical and mechanical components, even though the system maintains electrical balance throughout.

II. **Unsymmetrical faults**: Unsymmetrical faults (Line-to-Ground, Line-to-Line, and Double Line-to-Ground) are more common but less severe than symmetrical faults. They cause unbalanced current flow due to unequal phase impedances, disrupting system symmetry. Single-line ground faults are the most probable type of unsymmetrical fault. A pie chart showing the fault percentage of Adama II, Koka to Kality HV line that was responsible for each kind of fault in 2024 GC is displayed.

Table5. 1: Fault type occurring in Adama II, Koka to Kality transmission line and its duration of interruption in 2024 G.C

Fault Type	Duration of interruption (hrs.)
Single phase with ground (L-G)	120
Double line with ground (L-L-G)	59
Line to line (L-L)	35
Triple line (L-L-L)	12
Triple line with ground (L-L-L-G)	4
Total =230hrs.	

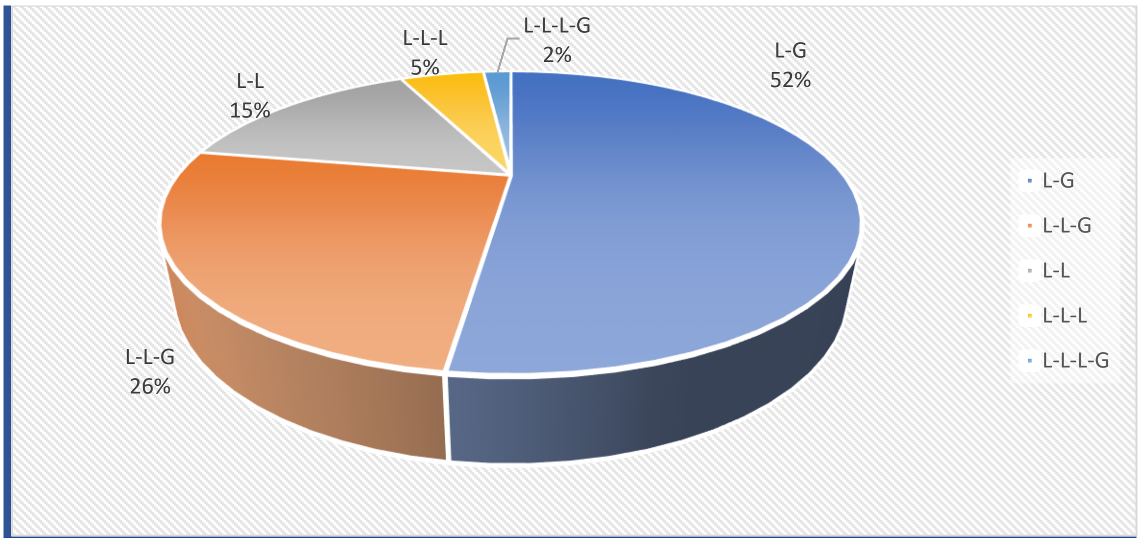

Figure5. 2: Percentage of faults occurring in Adama II, Koka to Kality line recorded in 2024 G.C.

5.3 System Performance at Base Case for an Average Load

In terms of rotor speed deviation, rotor speed, rotor angle deviation, output reactive power, excitation voltage, and output active power, this section illustrates how the Koka synchronous generators without compensators react to the average load on the transmission line at both the generation and transmission line levels. Analysis of the current behaviour of synchronous generators is aided by the simulation result, which displays the system's response without imposing a fault. As seen in the figure below, the system response initially oscillates as a result of switching surges. Over time, the oscillating amplitude diminishes and settles after a few seconds, and the arc is caused by switching off.

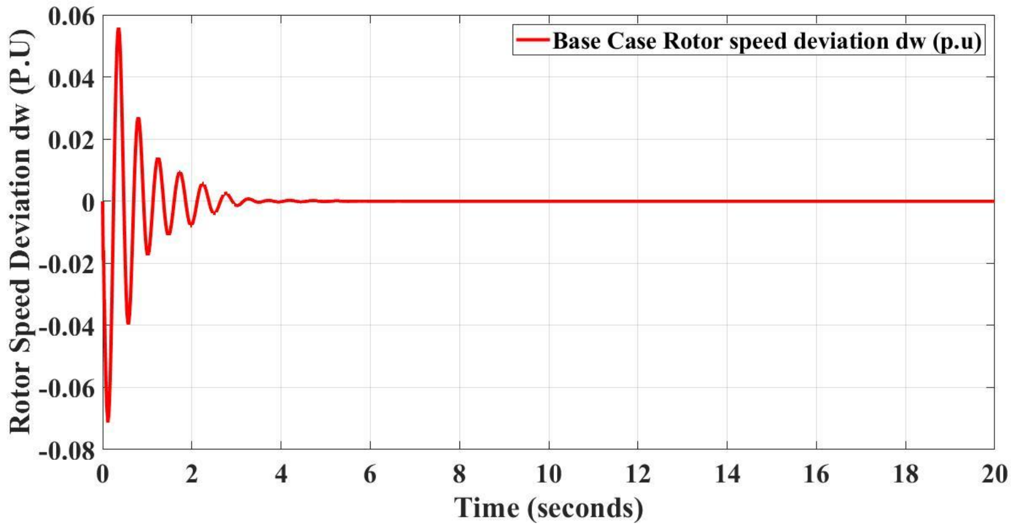

Figure5. 3: Base case rotor speed deviation response without disturbance dw(pu).

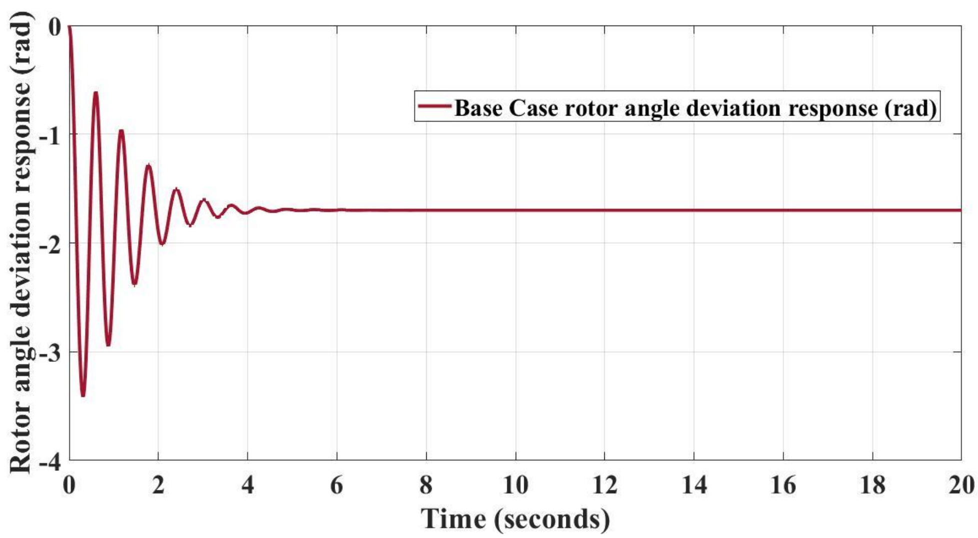

Figure5. 4: Base case rotor angle deviation response (rad) without disturbance

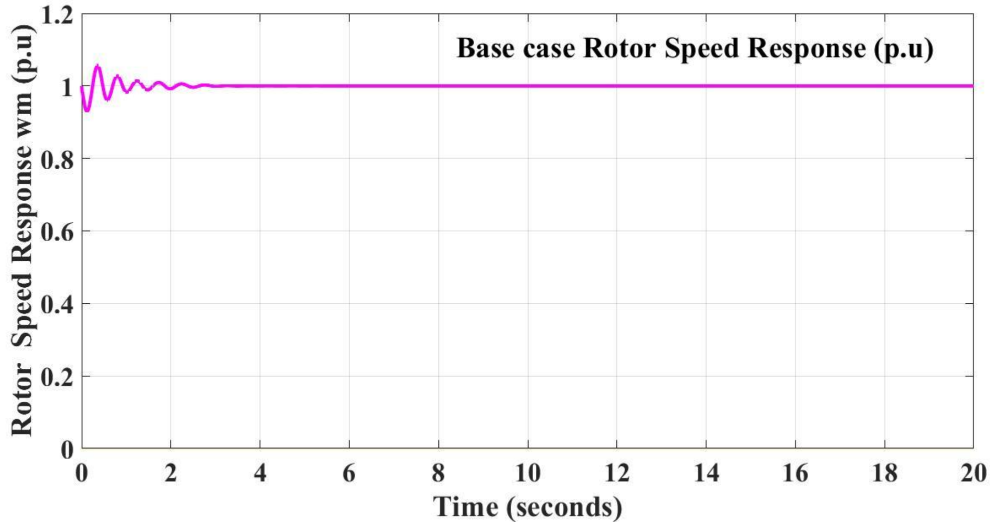

Figure5. 5: Base case rotor speed response(pu) without disturbance

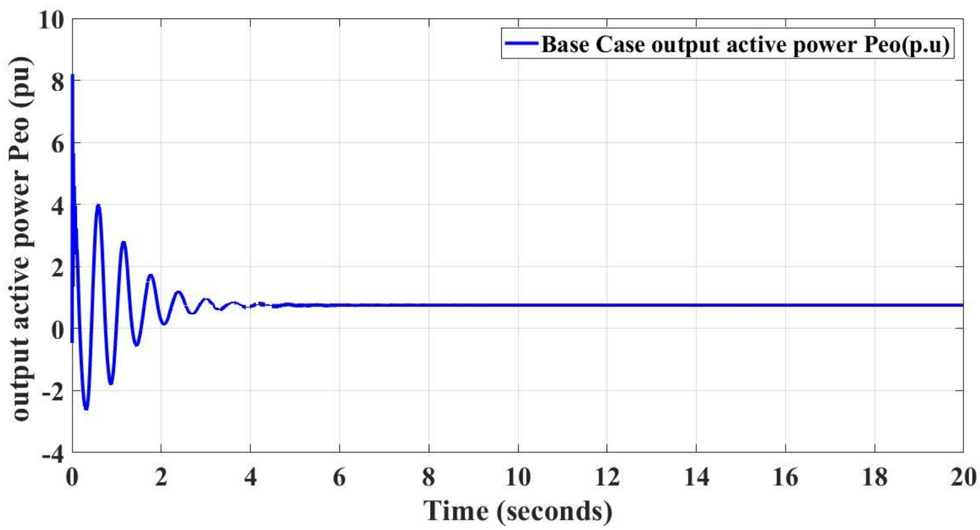

Figure5. 6: Base case output active power Peo(pu) response without disturbance

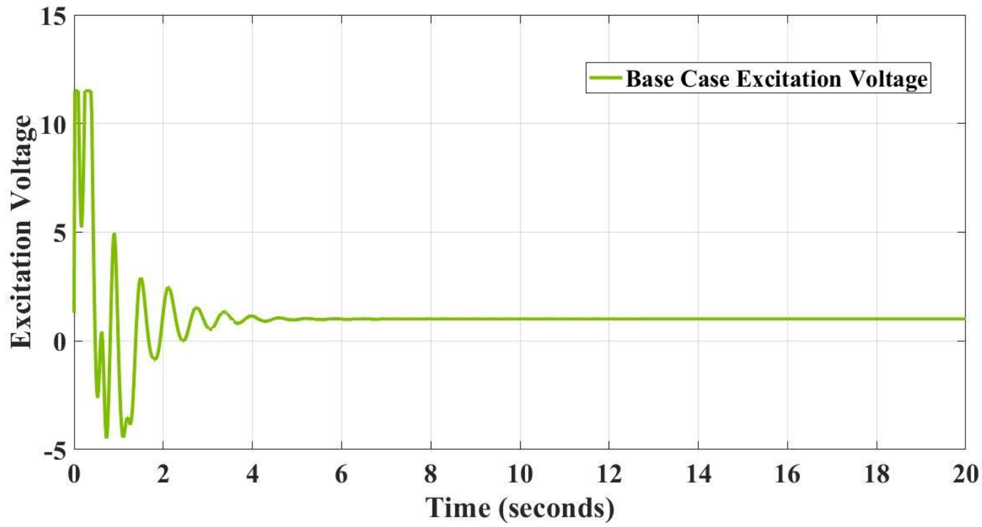

Figure5. 7: Base case Excitation Voltage response without disturbance

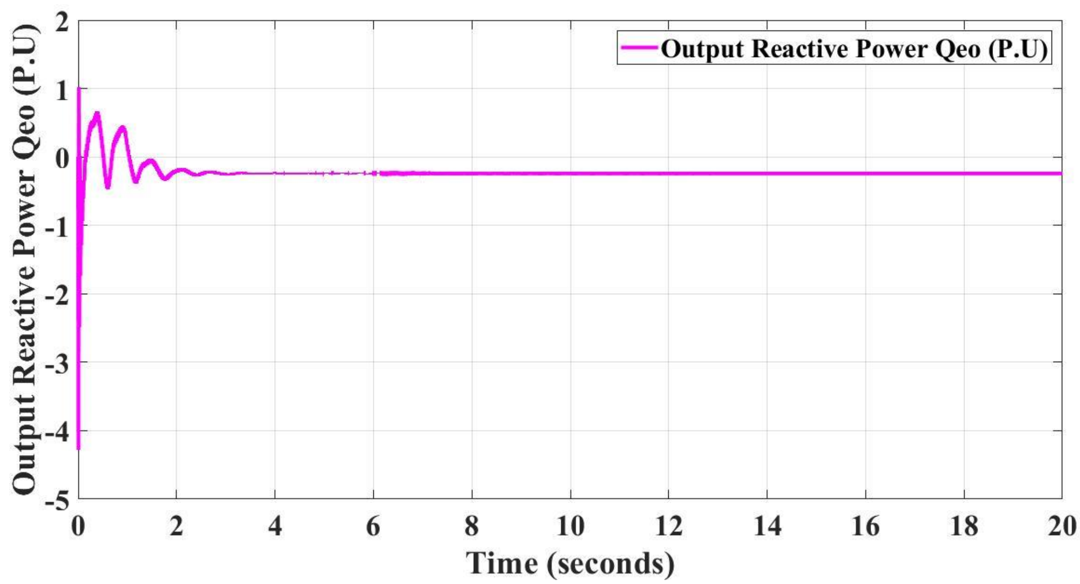

Figure5. 8: Base case output Reactive power Q(pu) response without disturbance

Two important indices are used to assess the system's performance in the time-domain simulation: settling time and percentage overshoot.

I. **Percentage overshoot:-** The ratio of the highest amount of the step excited output to the final output is called the overshoot of the system.

II. **Settling time:-** The amount of time it takes for the system response to stabilise and remain within a 2% tolerance of its ultimate value.

III. Figures 5.2 to 5.7 present simulation results indicating that, under base case conditions with an average load and no disturbances, the system variables rotor speed deviation, rotor angle deviation, rotor speed, generator output reactive power, excitation voltage, and generator output active power all exhibit a low settling time of less than 4 seconds. Additionally, the percentage overshoot for these parameters is 99%, 150%, 10.8%, 90%, 230%, and 301%, respectively. These results demonstrate that the system remains stable and maintains synchronism under normal operating conditions without faults.

5.4 Response of the System to a Disturbance with and Without UPFC

Three scenarios are used to assess the system's response: no UPFC, a PI-based UPFC, and an ANFIS-based UPFC. The PI controller parameters, determined using an autotuning method, are Kp = 9.8 and Ki = 0.3. This section examines the system's ability to maintain synchronism at the generation level during a disturbance on the transmission line, using performance metrics such as settling time and peak overshoot. If the issue is not promptly mitigated, it may result in severe equipment damage, potentially leading to power outages and blackouts.

5.4.1 Response of the System to a Fault at the Koka to Kality East Industry Transmission Line's The halfway point

This section uses a Simulink model to assess how adding a UPFC can improve transient stability during a disturbance at the midpoint of the Koka to Kality East Industry transmission line. The system's responses, such as active power, rotor angle deviation, rotor speed, rotor speed deviation, and excitation voltage, are specifically analysed in the context of both a three-phase and a single-phase ground fault at that location, as illustrated below.

I. System response for a balanced three-phase with ground fault

When a balanced three-phase fault is introduced at the midpoint of the Koka to Kality East Industry transmission line at 7 seconds and cleared at 7.25 seconds, the Koka generators' responses are shown in the figure below in terms of rotor angle deviation, rotor speed, output active power, rotor speed deviation, and excitation voltage.

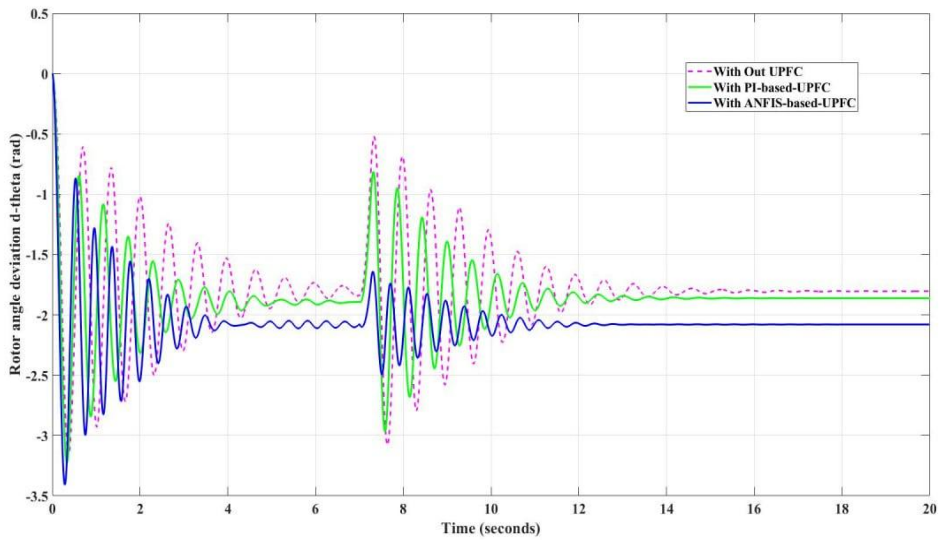

Figure5. 9: The Koka to Kality East Industry transmission line's midpoint, with and without UPFC, experienced a rotor angle deviation response for the 3-Ph-G fault.

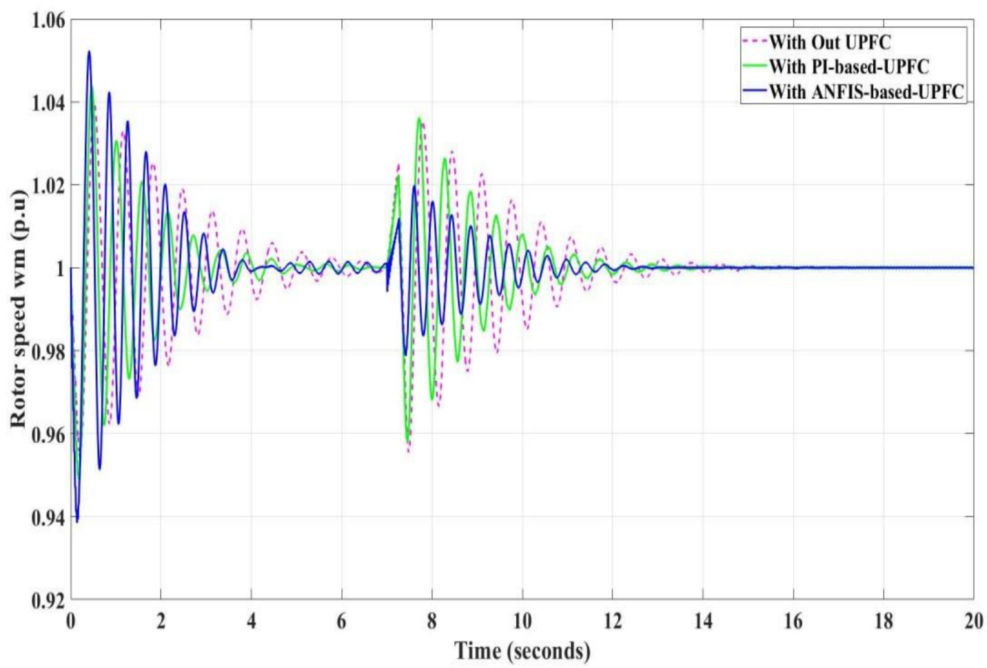

Figure5. 10: The midway of the Koka to Kality East Industry transmission line, both with and without UPFC, experienced a rotor speed response for a 3-Ph-G fault.

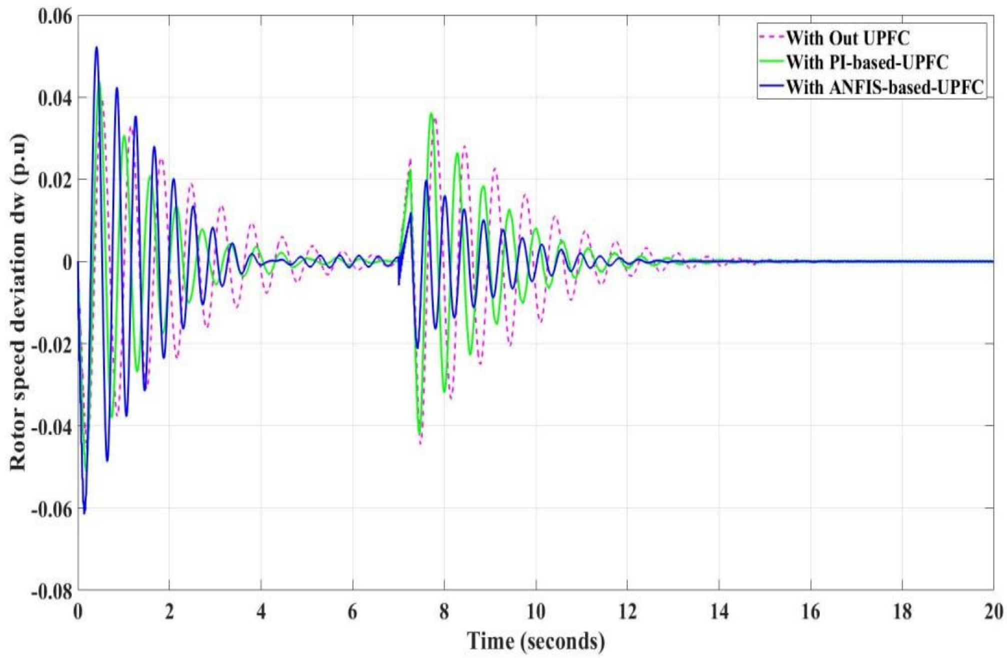

Figure5. 11: Rotor speed deviation response for a 3-Ph-G fault occurred at the midpoint of the Koka to Kality East Industry transmission line with and without UPFC.

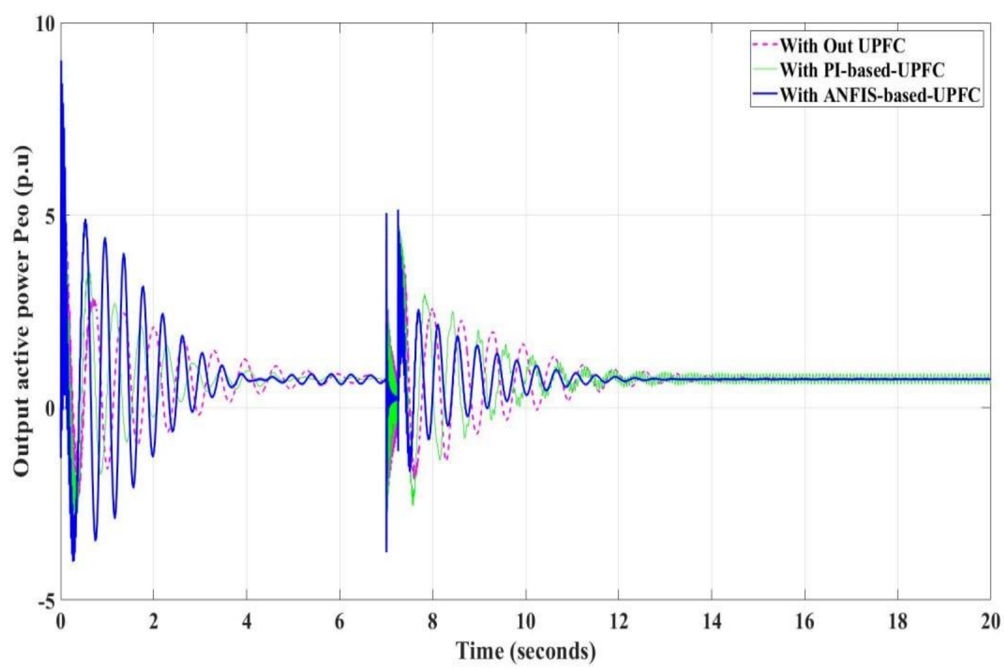

Figure5. 12: Output active power response for a 3-Ph-G fault occurred at the midpoint of the Koka to Kality East Industry transmission line with and without UPFC.

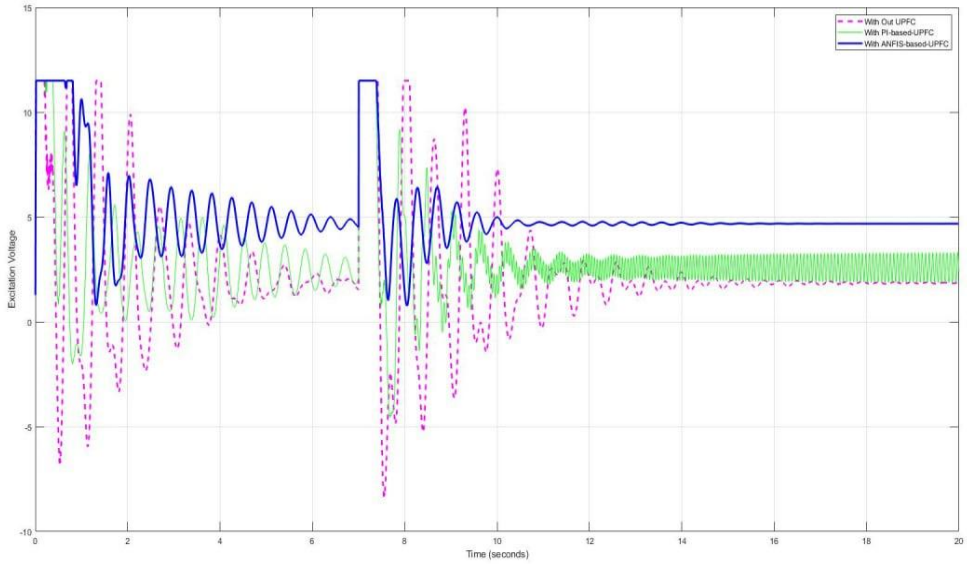

Figure5. 13: Excitation voltage response for a 3-Phase-G fault occurring at the midpoint of the Koka to Kality East Industry transmission line with and without UPFC.

Table5. 2: Comparison of the system response for different variables with and without UPFC when a 3-Phase-G fault occurred at the midpoint of the Koka to Kality East Industry transmission line

Variable type	Controller	Maximum peak value (Mp)	Percentage overshoot (%)	Settling time (sec)
Rotor angle deviation	Absent UPFC	1.70	99.99	8.49
	PI-based UPFC	1.00	52.65	5.99
	ANFIS-build UPFC	0.29	12.49	2.49
Rotor speed	Absent UPFC	0.04	4.90	9.79
	PI-based UPFC	0.04	4.00	6.29
	ANFIS-build UPFC	0.099	1.00	6.99
Rotor speed deviation	Absent UPFC	0.049	4.99	9.79
	PI-based UPFC	0.040	4.00	6.29
	ANFIS-build UPFC	0.099	1.00	6.099
Output active power	Absent UPFC	2.29	229	7.99
	PI-based UPFC	2.099	210	5.50
	ANFIS-build UPFC	0.099	10	4.50
Excitation Voltage	Absent UPFC	2.30	230	7.00
	PI-based UPFC	2.10	210	5.40
	ANFIS-build UPFC	0.100	10	4.40

According to Table 5.2, the PI-based UPFC improves the rotor angle deviation settling time by 30%, whereas the ANFIS-based UPFC improves it by 70.48%. The ANFIS- and PI-based UPFCs decrease the settling time by 38% and 36%, respectively, in relation to rotor speed. The ANFIS- and PI-based UPFCs show comparable improvements in rotor speed deviation, with reductions of 38% and 36%, respectively. The ANFIS-based UPFC improves the settling time for output active power by 44%, while the PI-based UPFC improves it by 30%.

II. System response for a single-phase with ground fault

The figure below illustrates the response of the Koka generators in terms of rotor angle deviation, rotor speed, output active power, and rotor speed deviation when a single-phase-to-ground fault occurred at the midpoint of the Koka to Kality East Industry transmission line at 7 seconds and was cleared at 7.25 seconds.

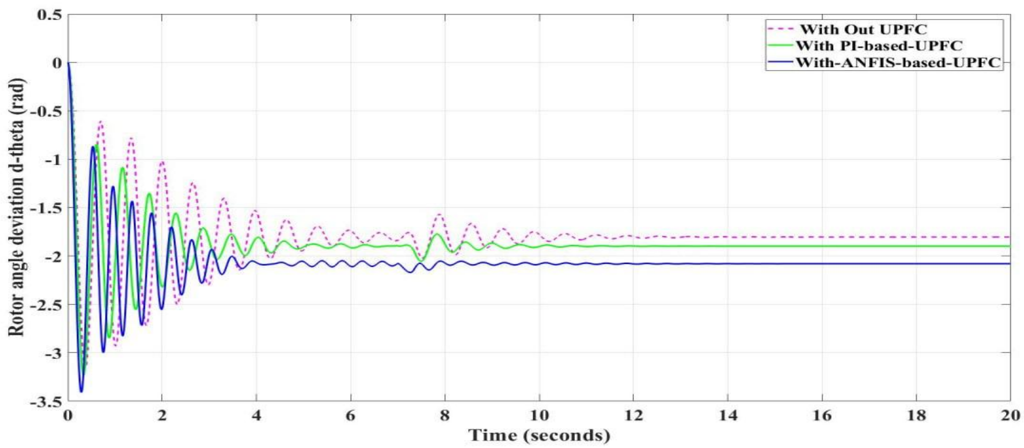

Figure5. 14: Rotor angle deviation response for a 1-Φ-G fault occurred at the midpoint of the Koka to Kality East Industry transmission line with and without UPFC.

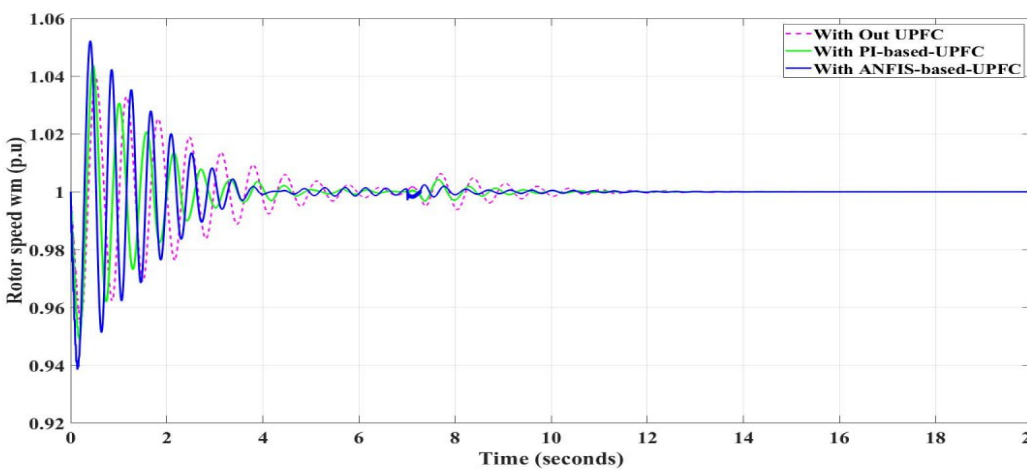

Figure5. 15: Rotor speed response for a 1-Φ-G fault occurred at the midpoint of the Koka to Kality East Industry transmission line with and without UPFC.

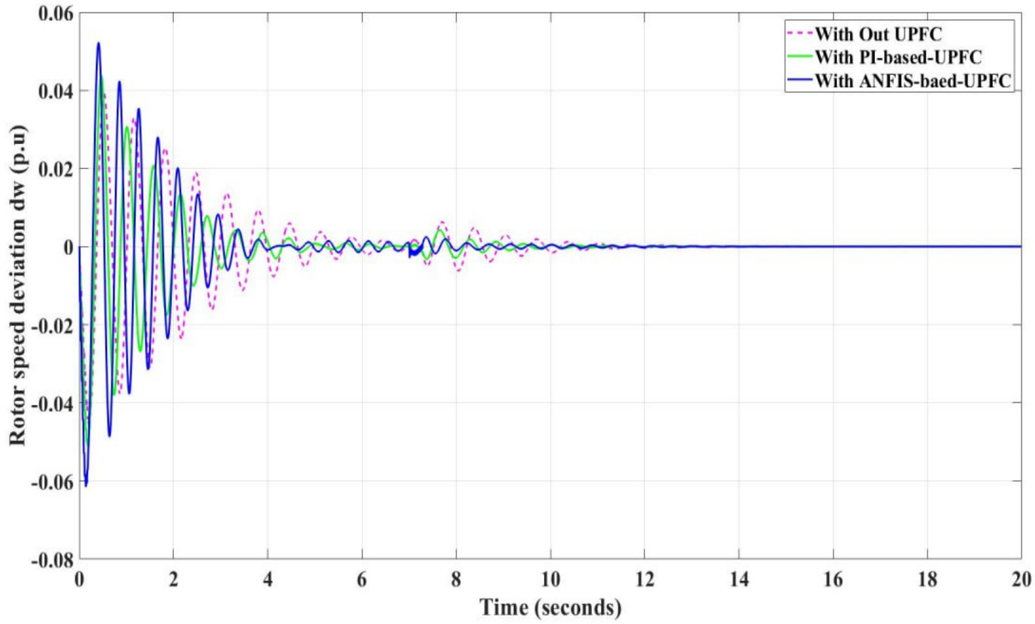

Figure5. 16: Rotor speed deviation response for a 1-Φ-G fault occurred at the midpoint of the Koka to Kality East Industry transmission line with and without UPFC.

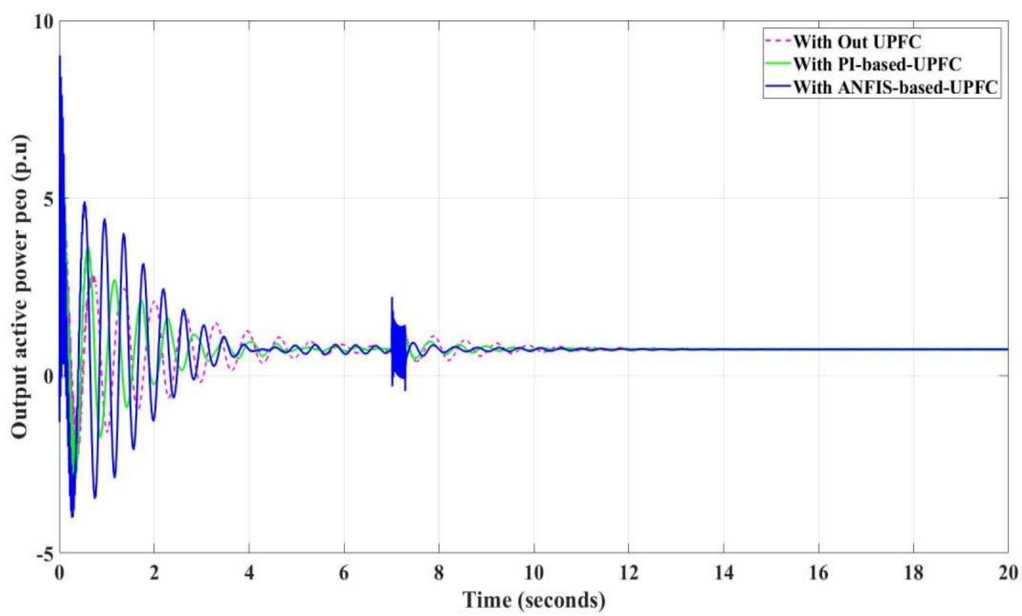

Figure5. 17: Output active power response for a 1-Φ-G fault occurred at the midpoint of the Koka to Kality East Industry transmission line with and without UPFC.

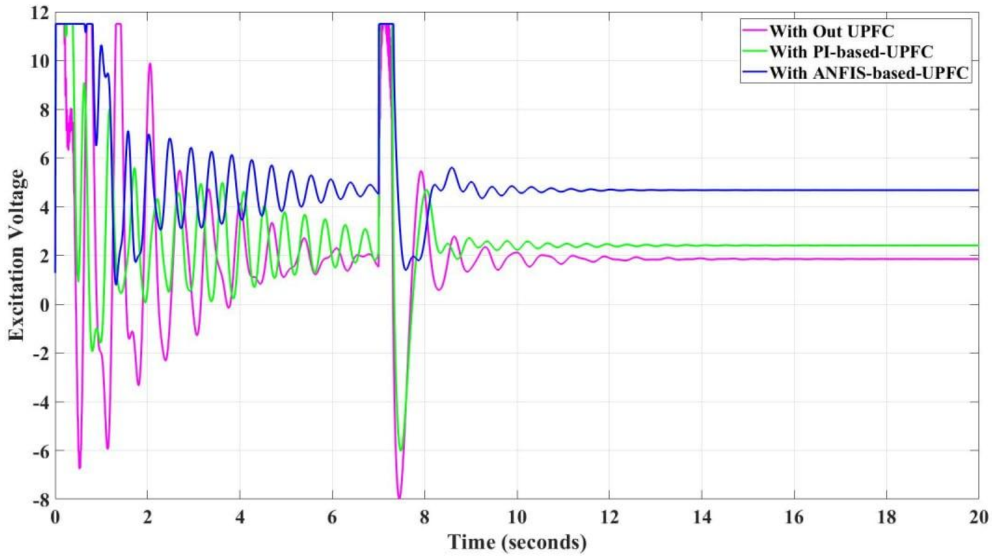

Figure5. 18: Excitation voltage response for a 1-Φ-G fault occurred at the midpoint of the Koka to Kality East Industry transmission line with and without UPFC.

Table5. 3: Comparison of the system response for different variables with and without UPFC when a 1-Φ-G fault occurred at the midpoint of the Koka to Kality East Industry transmission line.

Variable type	Controller	Maximum peak value (Mp)	Percentage overshoot (%)	Settling time (sec)
Rotor angle deviation	Not using UPFC	0.19	9.99	6.49
	PI-based UPFC	0.13	6.29	4.40
	ANFIS-based UPFC	0.99	4.69	2.00
Rotor speed	Not using UPFC	0.099	9.99	3.70
	PI-based UPFC	0.099	9.9	2.50
	ANFIS-based UPFC	0.0049	4.9	0.86
Rotor speed deviation	Not using UPFC	0.099	9.99	3.70
	PI-based UPFC	0.099	9.99	2.50
	ANFIS-based UPFC	0.0049	4.9	0.86
Output active power	Not using UPFC	0.69	69	2.80
	PI-based UPFC	0.75	75	2.50
	ANFIS-based UPFC	0.12	12	2.00
Excitation Voltage	Not using UPFC	0.70	70	2.79
	PI-based UPFC	0.76	76	2.55
	ANFIS-based UPFC	0.13	13	2.10

According to Table 5.3, the PI-based UPFC improves the rotor angle deviation settling time by 33%, whereas the ANFIS-based UPFC improves it by 70%. For rotor speed, the ANFIS-based and PI-based UPFCs reduce the settling time by 77% and 33%, respectively. The same percentage improvements are observed for rotor speed deviation. In terms of output active power, the ANFIS-based UPFC enhances the settling time by 29%, whereas the PI-based UPFC achieves an 11% improvement.

5.4.2 Response of the System to a Fault at the Adama Wind II to Kality Transmission Line's Midpoint

A Simulink model analyzes how a unified power flow controller (UPFC) affects transient stability during a fault on the Adama II-Kality transmission line's midpoint. The following figure shows the Adama Wind II generators' active power, rotor angle deviation, rotor speed, and rotor speed deviation responses to both three-phase and single-phase-to-ground faults at this location.

i. System response for a balanced three-phase with ground fault

The figure below illustrates how the Adama Wind II generators responded in terms of rotor angle deviation, rotor speed, output active power, and rotor speed deviation when a balanced three-phase ground fault occurred at the midpoint of the Adama Wind II to Kality transmission line at 7 seconds and was cleared at 7.25 seconds.

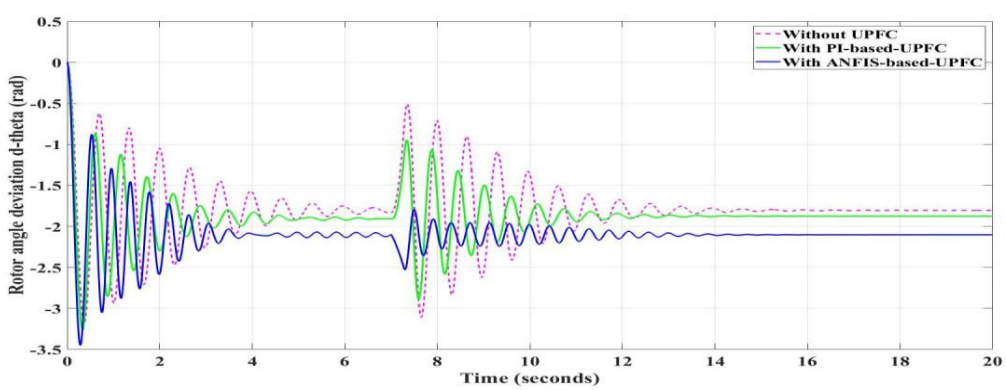

Figure5. 19: The Adama wind II to Kality transmission line's midpoint, with and without UPFC, experienced a rotor angle deviation response for the 3-Ph-G fault.

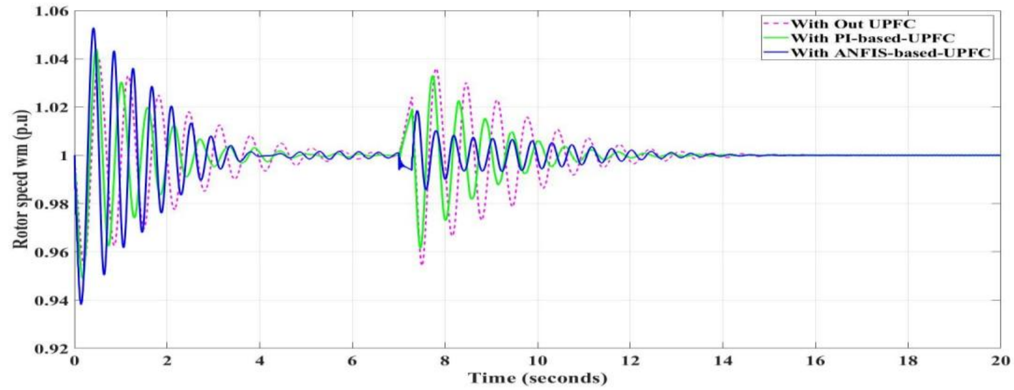

Figure5. 20: The midpoint of the Adama wind II to Kality transmission line, both with and without UPFC, experienced rotor speed response for the 3-Ph-G fault.

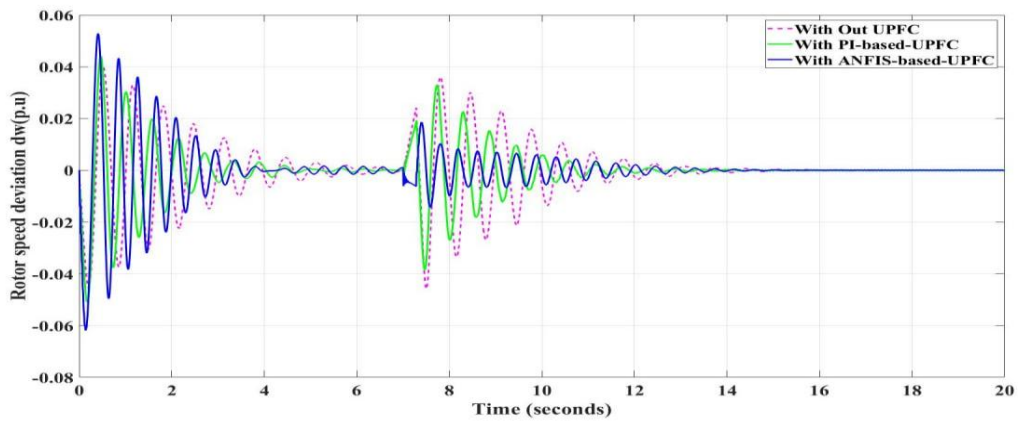

Figure5. 21: The Adama wind II to Kality transmission line's midpoint, with and without UPFC, experienced a rotor speed deviation response for the 3-Ph-G fault.

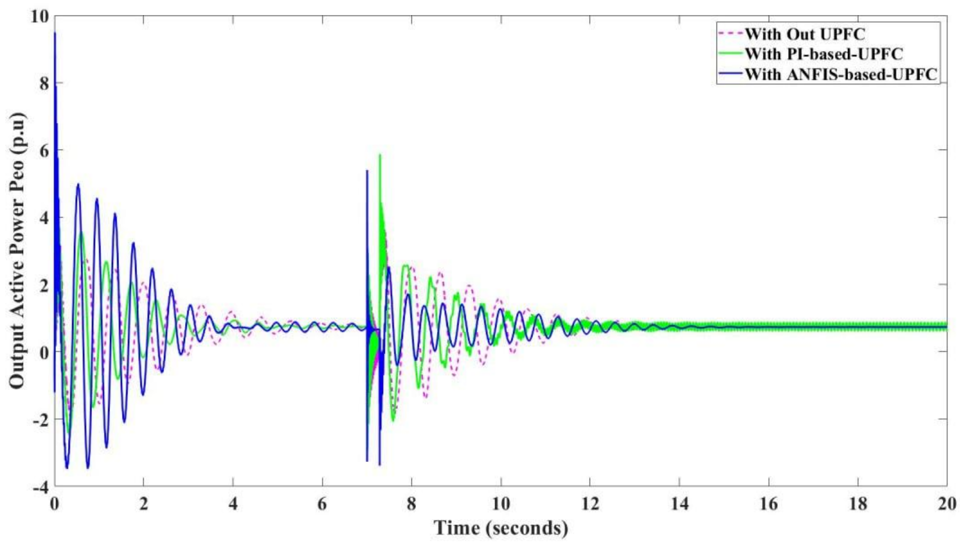

Figure5. 22: The Adama wind II to Kality transmission line's midpoint, both with and without UPFC, experienced an output active power response for the 3-Ph-G fault

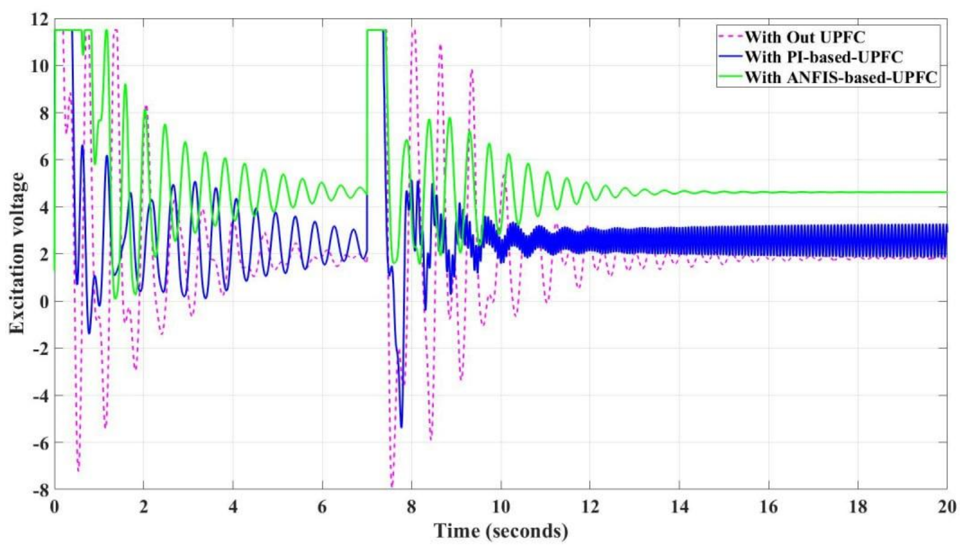

Figure5. 23: The Adama wind II to Kality transmission line's midpoint, both with and without UPFC, experienced an excitation voltage response for the 3-Ph-G fault.

Table5. 4: Comparison of the system response for different variables with and without UPFC when a 3-Ph-G fault occurred at the midpoint of the Adama Wind II to Kality line.

Variable type	Controller	Maximum peak value (Mp)	Percentage overshoot (%)	Settling time (sec)
Rotor angle deviation	Absent of UPFC	1.29	73	7.9
	PI-based UPFC	1.00	52.63	5
	ANFIS-based UPFC	0.29	14.28	4.19
Rotor speed	Absent UPFC	0.039	3.9	7.19
	PI-based UPFC	0.034	3.4	6.0
	ANFIS-based UPFC	0.099	0.99	4.79
Rotor speed deviation	Absent of UPFC	0.039	3.9	7.3
	PI-based UPFC	0.034	3.4	6.0
	ANFIS-based UPFC	0.099	0.99	4.79
Output active power	Absent of UPFC	1.4	140	6.6
	PI-based UPFC	4.00	400	4.5
	ANFIS-based UPFC	4.10	401	3.5
Excitation Voltage	Absent of UPFC	1.5	150	6.5
	PI-based UPFC	3.9	390	4.5
	ANFIS-based UPFC	4	400	3.6

Table 5.4 shows that the ANFIS-based UPFC reduces the settling time of rotor angle deviation by 47%, while the PI-based UPFC achieves a 37% improvement. For rotor speed, the ANFIS- and PI-based UPFCs enhance the settling time by 34% and 19%, respectively. Similar improvements are observed in rotor speed deviation, with reductions of 34% and 19% for the ANFIS- and PI-based controllers, respectively. Additionally, the settling time of output active power is improved by 45% with the ANFIS-based UPFC and by 31% with the PI-based UPFC.

ii. System response for a single-phase with ground fault

The Adama Wind II generators' responses to a single-phase ground fault that occurred at the midpoint of the Adama Wind II to Kality HV transmission line at 7 seconds and was cleared at 7.25 seconds are depicted in the figure below, specifically the rotor angle deviation, rotor speed, output active power, and rotor speed deviation.

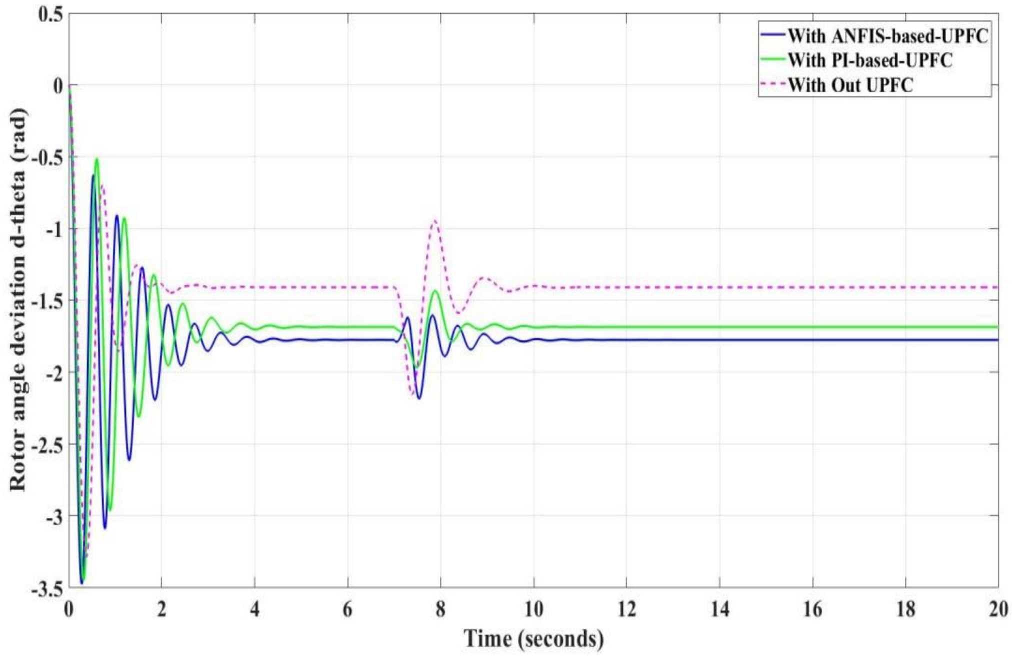

Figure5. 24: Rotor angle deviation response for a 1-Φ-G fault occurred at the midpoint of the Adama wind II to Kality transmission line with and without UPFC

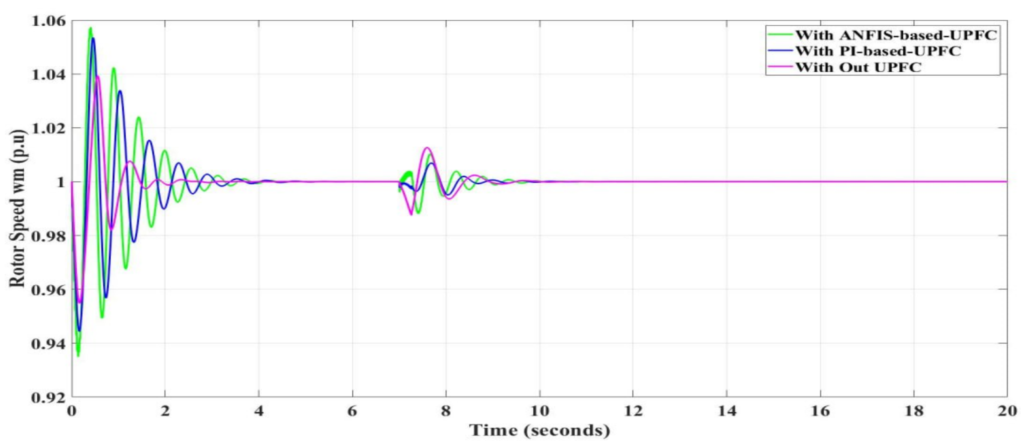

Figure5. 25: Rotor speed response for a 1-Φ-G fault occurred at the midpoint of the Adama wind II to Kality transmission line with and without UPFC.

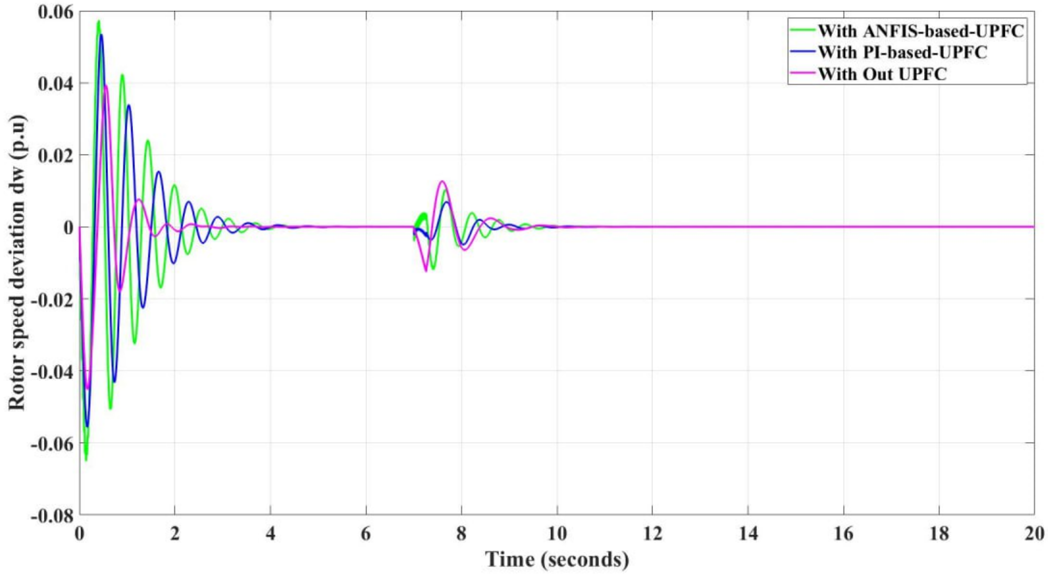

Figure5. 26: Rotor speed deviation response for a 1-Φ-G fault occurred at the midpoint of the Adama wind II to Kality transmission line with and without UPFC.

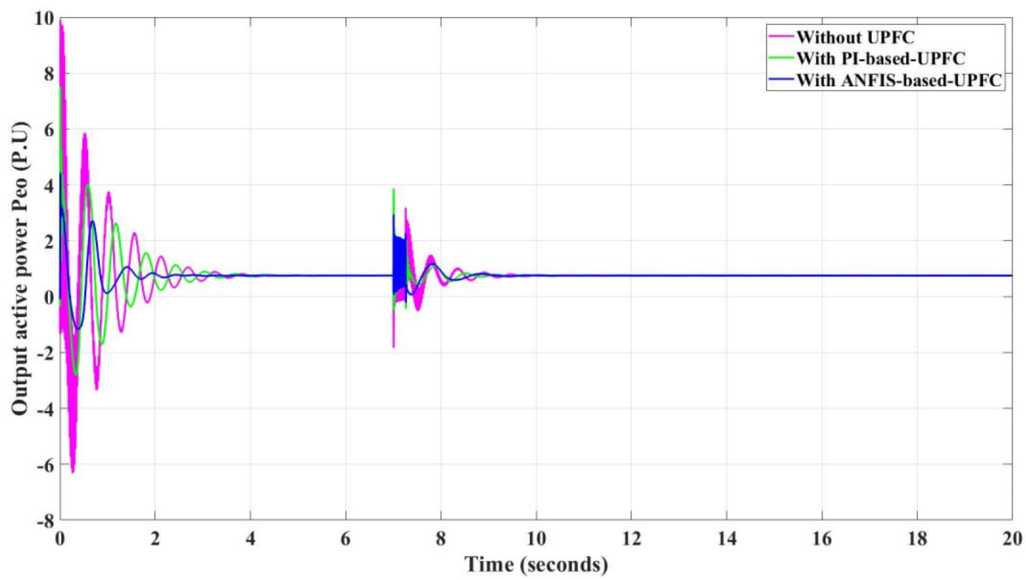

Figure5. 27: Output active power response for a 1-Φ-G fault occurred at the midpoint of the Adama wind II to Kality HV transmission line with and without UPFC.

Table5. 5: Comparison of the system response for different variables with and without UPFC when the 1-Φ-G fault occurred at the midpoint of the Adama Wind II to Kality line.

Variable type	Controller	Maximum peak value (Mp)	Percentage overshoot (%)	Settling time (sec)
Rotor angle deviation	Without UPFC	0.29	17.60	4.7
	PI-based UPFC	0.19	10.49	4.0
	ANFIS-based UPFC	0.09	4.40	2.0
Rotor speed	Without UPFC	0.010	1.00	2.99
	PI-based UPFC	0.010	1.00	2.09
	ANFIS-based UPFC	0.015	1.5	1.8
Rotor speed deviation	Without UPFC	0.010	1	3.0
	PI-based UPFC	0.010	1	2.1
	ANFIS-based UPFC	0.015	1.5	1.8
Output active power	Without UPFC	1	100	2.7
	PI-based UPFC	2	200	2.2
	ANFIS-based UPFC	5.2	520	1.9
Excitation Voltage	Without UPFC	0.99	99	2.8
	PI-based UPFC	1.99	199	2.3
	ANFIS-based UPFC	5.3	530	2.0

According to Table 5.5, the PI-based UPFC improves the rotor angle deviation settling time by 16%, whereas the ANFIS-based UPFC improves it by 57%. The settling time is decreased by 41% with the ANFIS-based UPFC and by 31% with the PI-based UPFC when considering rotor speed. For rotor speed deviation, the same enhancements hold true. Furthermore, the settling time of the output active power is improved by 33% and 25%, respectively, by the UPFCs based on ANFIS and PI.

5.4.3 Sending end and receiving end active power for Koka to Kality Line

A series voltage injection can increase the maximum real power that can be sent over a particular transmission line. In order for big power plants to supply more electricity over longer distances, voltage levels are raised. However, for long overhead transmission lines, voltage cannot be raised indefinitely due to the limitations of current high-voltage technology. In such cases, increasing power transfer is only possible by reducing line reactance, which can be achieved by integrating an ANFIS-based UPFC. This approach can be tested on the Koka–Kality high-voltage transmission line, as illustrated in the figure below. The capacity of Koka is 43 MW.

I. Sending and receiving active power at peak load from Koka to Kality line

The active power transferred from the sending end at Koka to Kality at maximum load is 43 MW. The active power at the receiving end is 32 MW in the absence of a UPFC, 38 MW in the presence of a PI-based UPFC, and 40 MW in the presence of an ANFIS-based UPFC.

Table5. 6: Loss minimized after incorporating UPFC into the transmission line.

Controller	Receiving end power (MW)	Power loss (MW)	Loss mimized (%)
without	32	11	-----
With PI-based UPFC	38	5	54.5455
With ANFIS-based UPFC	40	3	72.7272

5.4.4 Voltage magnitude at all buses after incorporating UPFC into the system

The bus voltage magnitudes at peak load, both before and after the integration of the UPFC into the system, are displayed in Table 5.10 below, presented in per unit (p.u.). As anticipated, the implementation of the ANFIS-based UPFC contributed to maintaining the voltage levels of all buses within acceptable limits during both disturbances and normal operation.

Table5. 7: Voltage magnitude at all buses after incorporating UPFC into the system.

Bus No	Bus location	Voltage magnitude (p.u.) without UPFC	Voltage magnitude (p.u) with ANFIS-based UPFC
1	Koka	1.0100	1.0100
2	Melka Wakena	1.000	1.00
3	Adama Wind Farm	1.020	1.020
4	Hurso	0.9432	0.9984
5	Gelan	0.9465	0.9824
6	Awash 7 kilo	0.9532	1.0087
7	Adama Wind II	1.0023	1.0023
8	Nazareth II	0.9432	0.9845
9	Awash II	0.9532	1.0047
10	Debrezeith II	0.9432	0.9980
11	Mojo	0.9270	0.9882

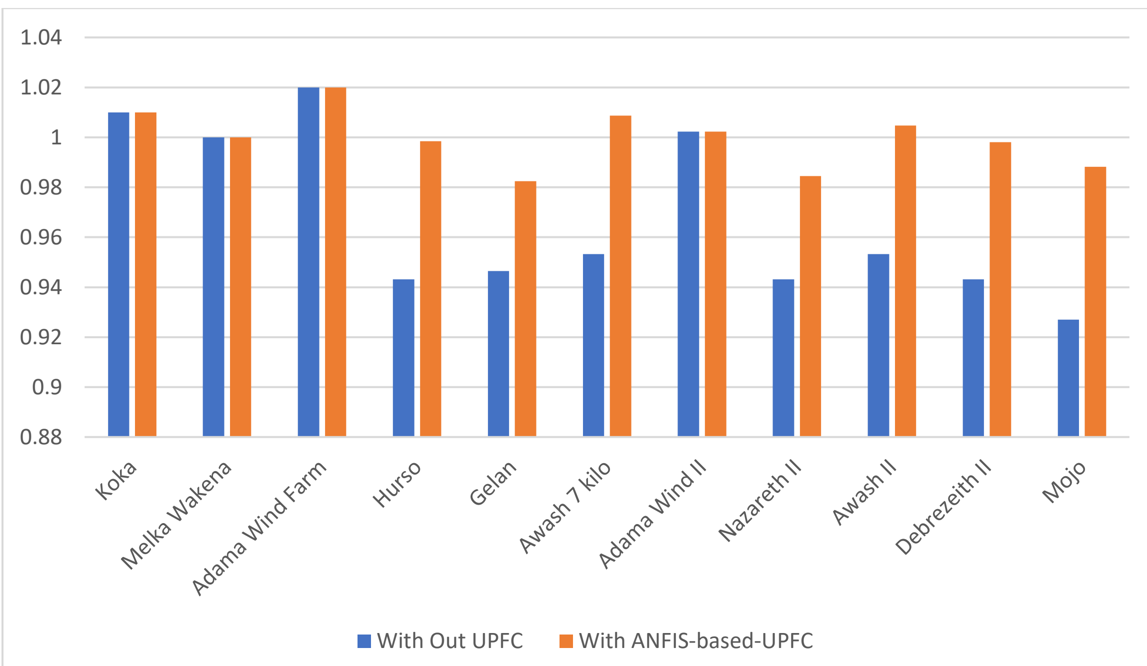

Figure5. 28: Voltage profile of each bus without UPFC and with ANFIS-based UPFC.

CHAPTER SIX

CONCLUSION AND RECOMMENDATION

6.1 Conclusion

This thesis is concerned with the transient stability problems in the interconnected power system that links Adama II, Koka, and the Kality Substation. An adaptive neuro-fuzzy inference system is used by the Unified Power Flow Controller (UPFC) to regulate power flow in high-voltage transmission networks. To test the controller's performance, the system is subjected to both single-line-to-ground and three-phase faults. The power flow performance of the transmission line is also assessed under minimum, average, and peak loading scenarios. By operating the current network infrastructure closer to its thermal limits, this method maximises its use and lessens the need to build new transmission lines.

The efficiency of the ANFIS-based UPFC is demonstrated by a three-phase ground fault at the middle of the Koka-Kality East Industry transmission line. It lowers settling times for rotor angle deviation, rotor speed, rotor speed deviation, and output active power by 70.48%, 38%, 38%, and 44%, respectively, in comparison to a system without a UPFC. A PI-based UPFC reduces active power loss on this line by 54.54% at peak load, while an ANFIS-based UPFC reduces it by 72.72%. Similarly, a PI-based UPFC reduces peak load active power loss by 50% on the Adama II, Koka, and Melka Wakena to Kality transmission line, while an ANFIS-based UPFC reduces it by 70%. The ANFIS-based Unified Power Flow Controller (UPFC) demonstrates superior performance over the conventional PI-based UPFC in enhancing transient stability. Specifically, it achieves a more rapid system response by reducing both the settling time and the percentage overshoot during fault conditions. While both controllers significantly improve the system’s stability and enhance the transmission capacity of the line, the neuro-fuzzy-based approach exhibits greater robustness, particularly under challenging operating scenarios.

6.2 Recommendations and Suggestions for Future Work

The UPFC based on ANFIS developed in this thesis aims to improve transient stability in high-voltage transmission lines. Currently, the power network linking Adama II, Koka, and Kality Substation is experiencing stress due to increasing load demands, which push the system close to its stability thresholds. Simulation results indicate that the ANFIS-based UPFC effectively resolves this problem by bolstering system security, optimizing the efficiency of power system components, minimizing transmission line losses, and reinforcing transient stability.

Overall, the UPFC device is more costly compared to traditional power flow controllers because of the advanced technology it employs. Nevertheless, this expense is justified by its exceptional ability to regulate all transmission line parameters, a point addressed in this thesis. Based on the results, it is recommended that Ethiopian Electric Power (EEP) implement the UPFC at the identified optimal location with the appropriate rating. Future research may explore expanding the application of the ANFIS-based UPFC to improve transient stability across Ethiopia's broader high-voltage transmission grid, beyond the current focus on the Adama II, Koka, and Kality substations.

REFERENCE

Abdelkrim, B., Abdelkader, C., Zoubida, A., & Mohamed, A. (2012). Neural adaptive control by state space system UPFC (SSNN) for compensation of active And reactive power. *International Journal of Scientific & Engineering Research, 3*(3).

Abugri, J. B., & Karam, M. (2015). Particle Swarm Optimization for the Minimization of Power Losses in Distribution Networks. *2015 12th International Conference on Information Technology - New Generations.*

Abugri, J. B., & Karam, M. (2015). Particle Swarm Optimization for the Minimization of Power Losses in Distribution Networks. *2015 12th International Conference on Information Technology - New Generations.*

Akele, S. (Spring Semester2012). *Customer Service Quality in Ethiopian Electric.* Uppsala University, Department of Business Studies.

Ashley-Edison. (2020). *Power quality in Ethiopia.* Bedford, England, United Kingdom: Sinalda.

Baharozu, E., Soykan, G., Altay, O., & Kalenderli, O. (2015). *An Improved Particle Swarm Optimization Method to Optimal Reactive Power Flow Problems.* Istanbul, Turkey: Bahcesehir University.

Balakrishnan , F. G., Sreedharan, S. K., & Michael, J. (2013). Transient Stability Improvement in Power System Using Unified Power Flow Controller (UPFC). *2013 Fourth International Conference on Computing, Communications and Networking Technologies (ICCCNT).*

Balakrishnan, F. G., & Sreedharan, S. K. (2013). Transient stability improvement in power system using unified power flow controller (UPFC). *2013 Fourth International Conference on Computing, Communications and Networking Technologies (ICCCNT), pp. 1-6.*

Benaissa, O. M., Hadjeri, S., & Zidi, S. A. (2016). Impact of PSS and SVC on the power system transient stability. *8th International Conference on Modelling, Identification and Control (ICMIC), pp. 303-307.*

Bodha, Gundala Srinivasa Rao and Venugopal Reddy. (2013). Improvement of Transient stability in Power Systems with NeuroFuzzy UPFC. *American Journal of Engineering Research (AJER), 02*.

Cabezas Soldevilla, F. R., & Cabezas Huerta, F. A. (2019). Minimization of Losses in Power Systems by Reactive Power Dispatch using Particle Swarm Optimization. *2019 54th International Universities Power Engineering Conference (UPEC).*

Chen, B., Fei, W., Tian, C., & Yuan, J. (Nov.-Dec. 2018). Research on an Improved Hybrid Unified Power Flow Controller. *in IEEE Transactions on Industry Applications, 54*(6), 5649-5660.

Chourasia, R., Saxena, V., Yadala, N., & Rhee, F. C. (2017). Visualization of Two-dimensional Interval Type-2 Fuzzy Membership Functions using General Type-2 Fuzzy Membership Functions. *2017 Joint 17th World Congress of International Fuzzy Systems Association and 9th International Conference on Soft Computing and Intelligent Systems (IFSA-SCIS).*

Das, D. (2006). *Electrical Power Systems.* West Bengal: New Age International (P) Ltd,publisher.

Das, P., Desmukh, S. M., & Sahu, L. (june 2016). Voltage Stability Improvement by using Fuzzy Logic Controller in Multi -Machine Power System. *International Journal of Scientific Engineering and Applied Science (IJSEAS), 2*(6).

Dires, L. (july 2021). *power transmission capacity and power system stability imrovement of exixsting HVAC lines with simultaneous AC-DC transmission.* Bahir Dar: Bahird University.

Eremia, M., & Shahidehpour, M. (2013). *Power System Stability and Protection.* in Handbook of Electrical Power System Dynamics: Modeling, Stability, and Control , IEEE.

F. Taki, S. Abazari and G. R. Arab Markadeh. (2010). Transient Stability Improvement Using ANFIS Controlled UPFC Based on Energy Function. *Proceedings of ICEE*.

Fujita, H., Watanabe, Y., & Akagi, H. (1999). Control and Analysis of a Unified Power Flow Controller. *in IEEE Transactions on Power Electronics, 14*(6), 1021-1027.

Hasanovic, A. (2000). *Modeling and Control of the Unified Power Flow Controller (UPFC).* Morgantown, West Virginia: College of Engineering and Mineral Resources at West Virginia.

Hasanovic, A. (2000). *Modeling and Control of the Unified Power Flow Controller (UPFC).* Morgantown, West Virginia: The College of Engineering and Mineral Resources.

Imdadullah, Amrr, S. M., Jamil Asghar, M. S., & Meraj, M. (2020). A Comprehensive Review of Power Flow Controllers in Interconnected Power System Networks. *in IEEE Access, 8*, 18036-18063.

Kandasamy, S., & Rajapalan, A. (2015). Dynamic control modeling and simulation of a UPFC–SMES compensator in power systems. *Ainf Shams Engineering Journal*.

Kassie, A. (2019). *Transient stability improvement using unified power flow controller with fuzzy logic.* Bahir Dar: Bahir Dar University.

Khan, S., & Bhowmick, S. (2015). A Fuzzy TCSC Controller for transient stability improvement. *2015 Annual IEEE India Conference (INDICON), New Delhi, India, 2015, pp. 1-5.*

Khurana, B. V., & Titare, L. S. (2020). Improvement of Power flow and voltage stability using UPFC with Artificial Neural Network in Matlab. *2020 IEEE International Symposium on Sustainable Energy, Signal Processing and Cyber Security (iSSSC), pp. 1-4.*

Kothari, D. P. (2011). *Modern Power System Analysis.* New Delhi: Tata McGraw Hill, New Delhi.

Kumar, M. S., Renuga, P., & Saravanan, K. (2009). Adaptive Neuro-Fuzzy Based Transient Stability Improvement Using UPFC. *International Journal of Recent Trends in Engineering*.

Kumar, R. J., & Rammohan, T. (2020). Enhancement of Transient Stability in Power System with Multi-Machine Using Facts Device. *IEEE International Conference on Advances and Developments in Electrical and Electronics Engineering (ICADEE), pp. 1-7*. Coimbatore.

Kumar, R., & Kumar, M. (2015). Improvement Power System Stability Using Unified Power Flow Controller Based On Hybrid Fuzzy Logic-PID Tuning In SMIB System. *2015 International Conference on Green Computing and Internet of Things (ICGCIoT), pp. 815-819.* Kota.

Kundur, P. (1994). *Power System Stability and Control.* New York: McGraw-Hill.

Kundur, P., Paserba, J., & Vite, S. (2003). Overview on Definition and Classification of Power System Stability. *CIGRE/IEEE PES International Symposium Quality and Security of Electric Power Delivery Systems.*

Latha, S., & Rani, C. K. (2013). Transient Stability Improvement with Unified Power Flow Controller Using Fuzzy Logic and ANFIS Approach. *Advanced Materials Research, 768*(12), 378-387.

Li, Q. (2006). *Analysis, design, and laboratory evaluation of a distributed unified power flow controller concept.* College of Engineering at the University of Kentucky.

Li, Q. (2006). *Analysis,design,and laboratory evaluation of a distributed unified power flow controller concept.* University of Kentucky.

Liu, F., Wang, H., Shi, Q., Wang, H., Zhang, M., & Zhao, H. (2017). Comparison of an ANFIS and Fuzzy PID Control Model for Performance in a Two-axis Inertial Stabilized Platform. *IEEE Access, 14*(8).

Mihalic, R., Zunko, P., & Povh, D. (Jan 1996). Improvement of transient stability using unified power flow controller. *in IEEE Transactions on Power Delivery, 11*(1), 485-492.

Mohanty, K. B., & Pati, S. (2016). Fuzzy logic controller based STATCOM for voltage profile improvement in a micro-grid. *2016 Annual IEEE Systems Conference (SysCon), pp. 1-6.*

Muzaffer, I., & ud din Mufti, M. (2017). Modeling of a Multi-Machine System Aided with Power System Stabilizers and Shunt Compensator for Transient Stability Enhancement. *International Conference on Energy, Communication, Data Analytics and Soft Computing (ICECDS)*, 1716-1721.

Obaid, Z. A., Mejeed, R. A., & Al-Mashhadani, A. (2020). Investigating the Impact of using Modern Power System Stabilizers on Frequency Stability in Large Dynamic Multi-Machine Power System. *2020 55th International Universities Power Engineering Conference (UPEC).* Baqouba, Diyala, Iraq.

Peng, F. Z. (Nov. 2017). Flexible AC Transmission Systems (FACTS) and Resilient AC Distribution Systems (RACDS) in Smart Grid. *in Proceedings of the IEEE, 105*(11), 2099-2115.

Rahman, H., Rahman, M. F., & rashid, H. O. (July 2012). Stability Improvement of Power System By Using SVC With PID Controller. *International Journal of Emerging Technology and Advanced Engineering, 2*(7).

Roy, M., & Kori, A. K. (2021). FUZZY LOGIC based Improvement of UPFC Performance in Power System. *2021 6th International Conference on Inventive Computation Technologies (ICICT),, pp. 245-250.*

Samal, S. K., & Panda, P. C. (2014). Damping of Power System Oscillations by Using Unified Power Flow Controller with POD and PID Controllers. *2014 International Conference on Circuit, Power and Computing Technologies [ICCPCT].*

Schauder et al., C. D. (April 1998). Operation of the unified power flow controller (UPFC) under practical constraints. *in IEEE Transactions on Power Delivery, 13*(2), 630-639.

Shao, Y., & Tang, Y. (2010). Voltage stability analysis of multi-infeed HVDC systems using small-signal stability assessment. *IEEE PES T&D, pp. 1-6.*

Sharma, N. K., & Jagtap, P. P. (2010). Modelling and application of Unified Power Flow Controller (UPFC). *IEEE Third International Conference on Emerging Trends in Engineering and Technology*. Goa (2010.11.19-2010.11.21).

Shen, Y., Li, Y., Kang, H., Zhang, Y., Sun, X., Chen, Q., . . . Wang, H. (2018). Research on Swarm Size of Multi-swarm Particle Swarm Optimization Algorithm. *2018 IEEE 4th International Conference on Computer and Communications (ICCC).*

Siddula, S., Achyut, T. V., Vigneshwar, K., & UdayTeja, M. V. (2020). Improvement of power quality using fuzzy-based Unified Power Flow Controller . *2020 International Conference on Smart Technologies in Computing, Electrical and Electronics (ICSTCEE),pp. 55-60.*

Singh, P., arida, S. K., Chauhan, B., & Choudhary, N. (2020). Online Voltage Stability Assessment Using Artificial Neural Network considering Voltage stability indices. *2020 21st National Power Systems Conference (NPSC), pp. 1-5.*

Singh, R., & Kirar, M. (2016). Transient stability analysis and improvement in microgrid. *2016 International Conference on Electrical Power and Energy Systems (ICEPES), Bhopal, India, 2016, pp. 239-245.*

Sreenivasachar, K. (2001). *Unified power flow controller :modelling,stability analysis,control strategy and contorl system design.* Ontario,Canada: University of Waterloo.

Sudha, K. R., & Reddy, K. H. (2009). A fuzzy controller for enhancement of power system stability with FACTs device. *Journal of Theoretical and Applied Information Technology*.

Tsehay, A. (2019). *Investigation and minimization of power loss and voltage profile enhancement using a unified power flow controller.* Bahir Dar: Bahir Dar University.

Vetoshkin, L., Votava, J., Kyncl, J., & Müller, Z. (2019). Improvement of transient stability using STATCOM combined with optimization. Prague, Czech Republic.

Wang, B., Fang, B., Wang, Y., Liu, H., & Liu, Y. (SEPTEMBER 2014). Power System Transient Stability Assessment Based on Big Data and the Core Vector Machine. *JOURNAL OF LATEX CLASS FILES, 13*(9).

Wang, S., Jing, L., Zhao, Y., Wickramasinghe, H. R., Wu, X., & Konstantinou, G. (2020). Operation of Unified Power Flow Controller as Virtual Synchronous Generator. *in IEEE Access, 8*, 162569-162580.

Wei, Q., Guo, W., Han, X., Li, T., & Yang, M. (2014). Analysis on the effect of rotor angle control for transient stability enhancement. *IEEE PES Innovative Smart Grid Technologies, Europe, pp. 1-6.* istanbul.

Yadv, V. K., Bindu, C. H., & M. N. (2015). Enhancement of Transient Stability in A Multi-Machine Power System Using Adaptive Neuro-Fuzzy Controller for Facts Devices. *international journal and magazine of Engineering,Technology,Management and Research, 2*.

Yang, S., Fan, X., Zhang, B., Hao, Z., & Masahide, H. (2019). A Unified Scheme for Power System Transient Stability Simulation and Transient Stability Assessment. *2019 IEEE 8th International Conference on Advanced Power System Automation and Protection (APAP).*

Yuan, B., Xing, L., Zhang, S., Hu, Y., Zhange, Z., & Li, G. (2020). Several Key Issues of the Unified Power Flow Controller in its Actual Application. *2020 7th International Forum on Electrical Engineering and Automation (IFEEA).*

APPENDICES

Appendix A: Simulink model of the system

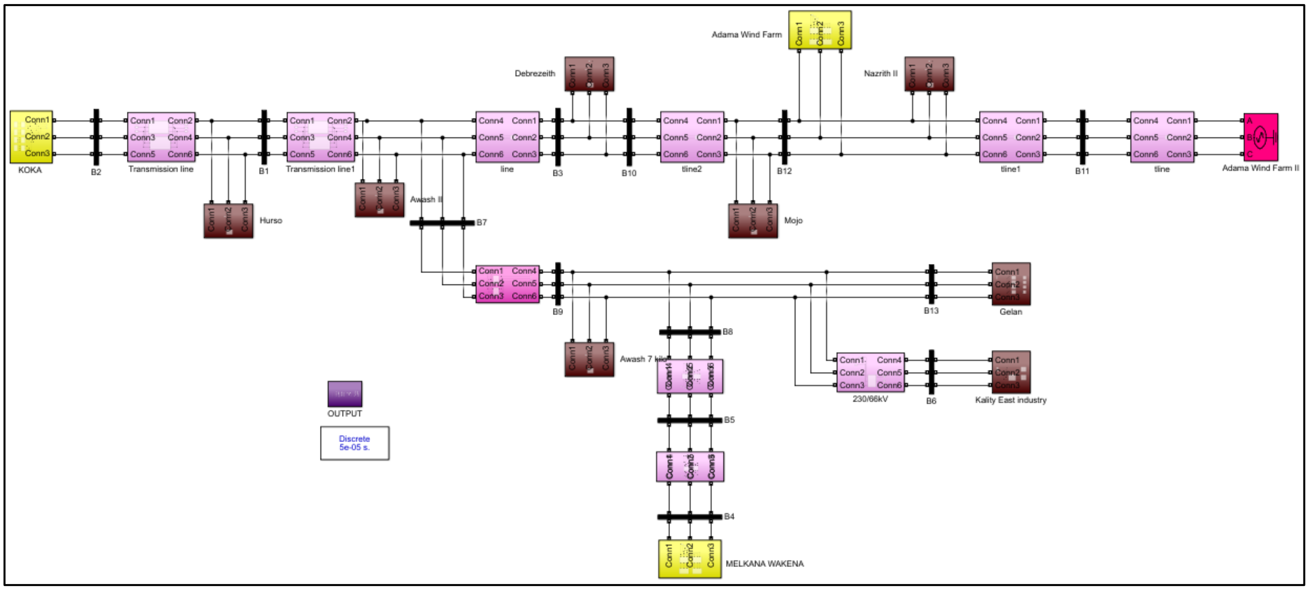

Appendix B: Transmission Line Data

Bus From	Bus To	Voltage in (kV)	Rating (MVA)	Length (km)	R (Ω/km)	X (Ω/km)	C (nF/km)
Koka	Kality	230	1340	82	0.00208	0.03096	12
Melka Waken	Koka	230	1340	327.72	0.00124	0.00244	9.5
Koka	Hurso	230	1341	250	0.00209	0.03096	12.2
Gelan	Koka	230	280	114	0.00725	0.04089	8.8
Koka	Awash 7	230	317	125	0.00918	0.03195	11.4
Adama II	Koka	230	318	12.5	0.00918	0.03205	11.4
Koka	Nazrit II	132	24	11.48	0.000127	0.00063	1.27
Koka	Awash II	132	24	50	0.00725	0.04089	8.8
Koka	Mojo	132	24	116	0.00725	0.04089	8.8

Appendix C: Generator Data

Generator station	MVA	H(s)	T'do	T''do =T''qo	Xd	Xq	X'd	X''d =X''q
Koka	90	2.5	7.1	0.12	1.00	0.6	0.29	0.365
Melka Wakena	90	3.14	9.2	0.10	1.03	0.7	0.31	0.250
Adama Wind II	40	3.14	9.1	0.11	1.02	0.71	0.21	0.260

Appendix D: Transformer Data

Voltage(kv)	Rating (MVA)	R (%)	X (%)	X/R (%)
230/ 132	90	0.211	13.36	57.33
230/ 66	90	0.52	12.368	28.76
230/ 33	6.3	0.401	8.4	27.78
132/ 10.5	24	0.355	7.8	30.35
132/ 6	6.3	0.322	6.387	28.85

Appendix E: Load Data

No	Bus name	Active power(MW)	Reactive power (Mvar)	Voltage level (KV)
1	Koka	43	1.7	230
2	Melka Wakena	150	57	230
3	Adama Wind Farm	150	18	230
4	Hurso	34	18	230
5	Gelan	22	2	230
6	Awash 7 kilo	15	30	230
7	Adama Wind II	18	8	230

8	Nazret	15	30	132
9	Awash II	18	8	132
10	Debrezeit II	25	1.7	230
11	Mojo	96	57	132
12	Kality East Industry	38	18	230

Appendix F: MATLAB code for UPFC placement using PSO integrated with Newton-Raphson

I. PSO.m

```
clc
clc;
clear all;
close all;
%% Problem Definition;
%error......power balance error
%Pgs.......slack power
%Toldev.......tolerance deviation of load flow
%angdev....angle deviation
%Vdev......voltage deviation
%Llim.....line capacity limit
%Pgsdev.....slack power deviation
CostFunction  =  @(x,Pgs,error,Plos,Toldev,  Vdev,  angdev,  Llim,Pgsdev)
Fitness  (x,error,Plos,Pgs,  Toldev,  Vdev,  angdev,  Llim,Pgsdev);%  Cost
Function
nVar = 2;                  % Number of Decision Variables
VarSize = [1 nVar];        % Size of Decision Variables Matrix

VarMin = [20 20];          % Lower Bound of Variables
VarMax = [80 50];          % Upper Bound of Variables


%% PSO Parameters

MaxIt =100;            % Maximum Number of Iterations

nPop = 100;            % Population Size (Swarm Size)

% PSO Parameters
wmax=0.9;              % Inertia Weight
wmin=0.4;
c1max = 2.5;           % Personal Learning Coefficient
c1min = 1.5;
c2max = 2.5;           % Global Learning Coefficient
c2min=1.5;
```

```
% Velocity Limits
VelMax = 0.1*(VarMax-VarMin);
VelMin = -VelMax;
%% Initialization

empty_particle.Position = [];
empty_particle.Cost = [];
empty_particle.Velocity = [];
empty_particle.Best.Position = [];
empty_particle.Best.Cost = [];
particle = repmat(empty_particle, nPop, 1);

GlobalBest.Cost = inf;
for i = 1:nPop

    % Initialize Position
    particle(i).Position = unifrnd(VarMin, VarMax, VarSize);
    % Initialize Velocity
    particle(i).Velocity = zeros(VarSize);
    [Pgs,Pl,Plos,Toldev,Vdev,angdev,
Llim,Pgsdev]=newton_raphson(particle(i).Position);
    error=PowerBalance(particle(i).Position,Plos,Pl,Pgs);
    particle(i).Cost  =  CostFunction(particle(i).Position,Plos,Pgs,error
,Toldev, Vdev, angdev, Llim,Pgsdev);

    % Update Personal Best
    particle(i).Best.Position = particle(i).Position;
    particle(i).Best.Cost = particle(i).Cost;

    % Update Global Best
    if particle(i).Best.Cost<GlobalBest.Cost

        GlobalBest = particle(i).Best;
    end
end

BestCost = zeros(MaxIt, 1);
%% PSO Main Loop

for it = 1:MaxIt
    for i = 1:nPop
        w(it)=wmax-(wmax-wmin)*it/MaxIt;
        c1(it)=c1max-(c1max-c1min)*it/MaxIt;
        c2(it)=c2min +(c2max-c2min)*it/MaxIt;
        % Update Velocity
        particle(i).Velocity = w(it)*particle(i).Velocity ...
            +c1(it)*rand(VarSize).*(particle(i).Best.Position-
particle(i).Position) ...
            +c2(it)*rand(VarSize) .*(GlobalBest.Position-
particle(i).Position);

        % Apply Velocity Limits
        particle(i).Velocity = max(particle(i).Velocity, VelMin);
        particle(i).Velocity = min(particle(i).Velocity, VelMax);
```

```
        % Update Position
        particle(i).Position = particle(i).Position + 
particle(i).Velocity;

        % Velocity Mirror Effect
        IsOutside = (particle(i).Position<VarMin | 
particle(i).Position>VarMax);
        particle(i).Velocity(IsOutside) = -
particle(i).Velocity(IsOutside);

        % Apply Position Limits
        particle(i).Position = max(particle(i).Position, VarMin);
        particle(i).Position = min(particle(i).Position, VarMax);



        [Pgs,Pl,Plos,Toldev, Vdev, angdev, 
Llim,Pgsdev]=newton_raphson(particle(i).Position);
        error=PowerBalance(particle(i).Position,Plos,Pl,Pgs);
        %           particle(i).Cost = 
CostFunction(particle(i).Position);
        particle(i).Cost = CostFunction(particle(i).Position,Pgs,error
,Plos,Toldev, Vdev, angdev, Llim,Pgsdev);
        % Update Personal Best
        if particle(i).Cost<particle(i).Best.Cost

            particle(i).Best.Position = particle(i).Position;
            particle(i).Best.Cost = particle(i).Cost;

            % Update Global Best
            if particle(i).Best.Cost<GlobalBest.Cost

                GlobalBest = particle(i).Best;

            end

        end

    end
    BestCost(it) = GlobalBest.Cost;
    disp(['Iteration ' num2str(it) ':Slack power='  num2str(Pgs(1)) ': 
Best Fitness = ' num2str(BestCost(it))]);
end
BestSol = GlobalBest;
%% Results

figure;
semilogy(BestCost, 'b','LineWidth', 3);
xlabel('Iteration');
ylabel('Best Fitness');
grid on;
```

II. Newton_Raphson.m

```
function[Pgs,Pl,Plos,Toldev, Vdev, angdev,
Llim,Pgsdev]=newton_raphson(X)
MVA_base=133.0;
[linedata,busdata,acceleration_factor,tolerence,nPV,nLB] =
Data11();%Calling the function containing the input data(Stevenson-337)

fb=linedata(:,1); % Storing the from-bus numbers
tb=linedata(:,2); % Storing the to-bus numbers
r=linedata(:,3); % Storing the resistance(s)
x=linedata(:,4); % Storing the reactance(s)
b=linedata(:,5); % Storing the half-line charging(shunt-admittance)
a=linedata(:,6); % Storing the off-nominal trans-ratio
bus_type=(busdata(:,2)); % Storing the bus-type(s)
v_bus_initial=(busdata(:,3)); % Storing the initial bus-voltage(s) in
(p.u.)
P_gen=((busdata(:,5))*(MVA_base)); % Storing the active power generated
at bus(s)
Q_gen=((busdata(:,6))*(MVA_base)); % Storing the reactive power
generated at bus(s)
S_gen=((P_gen)+(1i)*(Q_gen)); % Storing the complex power generated at
bus(s)
Pl=((busdata(:,7))*(MVA_base)); % Storing the active power at load(s)
at bus(s)
P_gen(2)=X(1,1);
P_gen(3)=X(1,2);
Q_load=((busdata(:,8))*(MVA_base)); % Storing the reactive power at
load(s) at bus(s)
S_load=((Pl)+(1i)*(Q_load)); % Storing the complex power at load(s) at
bus(s)
Q_min=((busdata(:,9))*(MVA_base)); % Storing the minimum Q-range of the
PV-bus(s)
Q_max=((busdata(:,10))*(MVA_base)); % Storing the maximum Q-range of
the PV-bus(s)
B_shunt=((busdata(:,11))); % Storing the data corresponding to the
static shunt capacitance
z_elementary=((r)+(1i)*(x));
Z=z_elementary;
b_elementary=((1i)*(b)); % Calculating the 'b'
nbus = max(max(fb),max(tb));     % no. of buses
nbranch = length(fb);            % no. of branches

z=zeros(nbus,nbus); % Initialising the elementary [z]
b=zeros(nbus,nbus); % Initialising the elementary [b]
Ybus=zeros(nbus,nbus); % Initialising the elementary [Y] (Bus-
admittance matrix)
tolerence_checker=1; % Initialising the 'tolerence_checker' as '1'
iteration=0; % Initialising the 'iteration' as '0'
V_new=v_bus_initial; % Initialising the 'V_new[]' as 'V_initial[]'
v_scheduled=v_bus_initial; % Initialising the 'v_scheduled[]' as
'V_initial[]' (to get the scheduled voltages at the PV-bus(s))
V_new_accelerated=zeros(1,nbus); % Initialising the
'V_new_accelerated[]'inj_pow_mismatch_vector=zeros(((2*(nbus-1))-
nPV),1); % Initialising the 'inj_pow_mismatch_vector[]'
```

```
correction_vector=zeros(((2*(nbus-1))-nPV),1); % Initialising the
'correction_vector[]'
correction_voltage_angle=zeros((nbus-1),1); % Initialising the
'correction_voltage_angle[]'
correction_voltage_magnitude=zeros((nbus-1-nPV),1); % Initialising the
'correction_voltage_magnitude[]'
mismatch_active_vector_element_count=1; % Initialising the
'mismatch_active_vector_element_count' as (1)
mismatch_reactive_vector_element_count=1; % Initialising the
'mismatch_reactive_vector_element_count' as (1)
mismatch_vector_element_count=0;% Initialising the
'mismatch_active_vector_element_count' as (0)
real_mismatch=zeros(nbus-1,1);
imag_mismatch=zeros(nbus-1-nPV,1);

for u=1:((2*(nbus-1))-nPV)
    correction_vector(u)=1.0; % Initialising the correction vector
element(s) as (1.0); so that loop can be started
end

% Forming the elementary z-matrix & b-matrix

for u=1:nbranch
    z(fb(u),tb(u))=z_elementary(u); % Storing the mutual element(s)
(Z(i,j))
    z(tb(u),fb(u))=z(fb(u),tb(u)); % Storing the similar element(s) in
(Z(j,i))
    b(fb(u),tb(u))=b_elementary(u); % Storing the mutual element(s)
(B(i,j))
    b(tb(u),fb(u))=b(fb(u),tb(u)); % Storing the similar element(s) in
(B(j,i))
end

% Modification(s) in the element(s) of 'z' & 'b' due to OFF-NOMINAL
TRANS RATIO

for u=1:nbranch
    if((a(u,1))~=1.0)
        shunt_fb_onr(1,u)=(((a(u,1))^(2))/(1-(a(u,1)))); % Calculating
the (a^2/(1-a))

b(fb(u),tb(u))=(1/((shunt_fb_onr(1,u))*(z(fb(u),tb(u)))))+(b(fb(u),tb(u
))); % Modifying the element 'b' matrix w.r.t. 'fb'
        shunt_tb_onr(1,u)=((a(u,1))/((a(u,1))-1)); % Calculating the
(a/(a-1))
        b(tb(u),fb(u))=(1/((shunt_tb_onr(1,u))*(z(fb(u),tb(u))))); %
Modifying the element 'b' matrix w.r.t. 'tb'
        z(fb(u),tb(u))=z(fb(u),tb(u))*(a(u,1)); % Modifying the 'z'
matrix
        z(tb(u),fb(u))=z(fb(u),tb(u)); % Storing the similar element(s)
in (Z(j,i))
    end
end
Q_injected_scheduled=((Q_gen-Q_load)/(MVA_base)); % calculating the
scheduled injected reactive power at each bus
```

```
for u=1:nbus
    for j=1:nbus
        if((u~=j)&&(abs(Ybus(u,j)))~=0.0)

P_injected_sum(u,1)=((P_injected_sum(u,1))+(((abs((V_new(u,1))*(V_new(j
,1))*(Ybus(u,j))))*(cos((angle(Ybus(u,j)))+(angle(V_new(j,1)))-
(angle(V_new(u,1)))))))); % calculating the mutual sumation part
        end
        if((u~=j)&&((abs(Ybus(u,j)))~=0.0)&&(bus_type(u)~=2))

Q_injected_sum(u,1)=((Q_injected_sum(u,1))+(((abs((V_new(u,1))*(V_new(j
,1))*(Ybus(u,j))))*(sin((angle(Ybus(u,j)))+(angle(V_new(j,1)))-
(angle(V_new(u,1)))))))); % calculating the mutual sumation part
        end
        if(j==nbus)

P_injected_bus(u,1)=((((abs(V_new(u,1)))^(2))*(Gbus(u,u)))+(P_injected_
sum(u,1))); % calculating the injecetd 'P' at bus-(u)
        end
        if((j==nbus)&&(bus_type(u)~=2))
            Q_injected_bus(u,1)=(-
((((abs(V_new(u,1)))^(2))*(Bbus(u,u)))+(Q_injected_sum(u,1)))); %
calculating the injecetd 'Q' at bus-(u)
        end
    end
end
for u=1:nbus
    if(bus_type(u)~=1)

inj_active_pow_mismatch_vector(mismatch_active_vector_element_count,1)=
((P_injected_scheduled(u,1))-(P_injected_bus(u,1))); % calculating the
mismatch vector for active power injecttion

mismatch_active_vector_element_count=mismatch_active_vector_element_cou
nt+1; % updating the value of 'mismatch_vector_element_count'
    end
    if((bus_type(u)~=1)&&(bus_type(u)~=2))

inj_reactive_pow_mismatch_vector(mismatch_reactive_vector_element_count
,1)=((Q_injected_scheduled(u,1))-(Q_injected_bus(u,1))); % calculating
the mismatch vector for reactive power injecttion

mismatch_reactive_vector_element_count=mismatch_reactive_vector_element
_count+1; % updating the value of 'mismatch_vector_element_count'
    end
end
for u=2:nbus

if(mismatch_vector_element_count<=((mismatch_active_vector_element_coun
t-1)+(mismatch_reactive_vector_element_count-1)))
        inj_pow_mismatch_vector((u-
1),1)=inj_active_pow_mismatch_vector(u-1,1); % storing the mismatch in
the active power
        mismatch_vector_element_count=mismatch_vector_element_count+1;
% updating the 'mismatch_vector_element_count'
```

```
    end
active_flow_line(1,flow_count)=real(complex_flow_line(1,flow_count)); %
P.U. active power flow from (u->j)
           reactive_flow_line(1,flow_count)=(-
(imag(complex_flow_line(1,flow_count)))); % P.U. reactive power flow
from (u->j)


bus_power_injection(1,u)=bus_power_injection(1,u)+conj(complex_flow_lin
e(1,flow_count)); % Calculating the bus-power-injection(s)
           bus_power_mismatch(1,u)=((S_gen(u,1)-S_load(u,1))/MVA_base)-
(bus_power_injection(1,u)); % Calculating the bus-power-mismach
           flow_count=flow_count+1; % Updating the flow_count by (1)
       end
   end
end
Tol1=max(real(bus_power_mismatch));
Tol2=max(imag(bus_power_mismatch));
Tol=max(Tol1,Tol2);

for u=1:nbus
    for j=1:nbus
        if((u<j)&&(abs(line_flows(u,j))~=0.0))
            line_loss(u,j)=line_flows(u,j)+line_flows(j,u); %
Calculating the individual line-loss
            real_line_loss=abs(real(line_loss(u,j))); % Absolute value
of the active-line-loss
            imag_line_loss=abs(imag(line_loss(u,j))); % Absolute value
of the reactive-line-loss
            line_loss(u,j)=(real_line_loss)+(imag_line_loss)*(1i);
            sum_line_loss=sum_line_loss+line_loss(u,j); % Calculating
the total line-loss
        end
    end
end
%caclulating  branch current
Vs=V_new(fb);
Vr=V_new(tb);
for i=1:11
Iline(i)=(Vs(i)-(Vr(i)))*a(i)/Z(i);
end
VS=abs(Vs)
VR=abs(V_new(tb));
ILINE=abs(Iline)';

V=abs(V_new);
del=angle(V_new);
Plos=real(sum_line_loss);
P=real(bus_power_injection);
Pgs=P(1)*100;
if Pgs>=160
    Pglim=160;
elseif Pgs<=10
    Pglim=10;
else
    Pglim=Pgs;
```

```
end
Pgsdev=Pgs-Pglim;
% convergency cheker
if Tol>=tolerence
    penalty=10000;
else
    penalty=0;
end
Toldev=penalty*(Tol-tolerence);
%angle ang voltage limit

for i=1:11
    if V(i)>=1.05
        vlim(i)=1.05;
    elseif V(i)<=0.95
        vlim(i)=0.95;
    else
        vlim(i)=V(i);
    end

end
vdev=V-vlim';
Vdev=max(vdev);
for i=1:11
    if del(i)>=0.785
        anglim(i)=0.785;
    elseif del(i)<=-0.785
        anglim(i)=-0.785;
    else
        anglim(i)=del(i);
    end
end
 Angdev=del-anglim';
 angdev=max(Angdev);%take maximum deviation
linecap=linedata(:,7);
linecapacity=[linecap;-linecap];
for i=1:22
    llim(i)=(abs(complex_flow_line(i))-abs(linecapacity(i)));
end
Llim=max(llim); %take maximem deviation
end
```

Appendix G: Primary Data Validation

A fault was recorded in Adama II wind farm

Fault Location	Quantity	Fault Description
Generator	50	Broken of their rotor terminal and/or burning of their slip rings
Pitch system	15	Burning of the pitch driver and capacitor charger.
Back-to-Back converter	60	IGBT, DC and AC bus fuse failure.
Crowbar	20	Crowbar IGBT failure and/or total burnout.